ENERGY BALANCE FLUXES IN A SUBTROPICAL CITY: MIAMI, FL.

By

TREVOR NEIL NEWTON

B.A. (Hons.) The University of British Columbia, 1994

A THESIS SUBMITTED IN PARTIAL FULFILLMENT OF
THE REQUIREMENTS FOR THE DEGREE OF

MASTER OF SCIENCE

in

THE FACULTY OF GRADUATE STUDIES

(Department of Geography)

We accept this thesis as conforming
to the required standard

THE UNIVERSITY OF BRITISH COLUMBIA

October 1999

Department of Geography

The University of British Columbia
Vancouver, Canada

Date October 12, 1999

ABSTRACT

This study presents summertime surface energy balance measurements from a suburb in west Miami, Florida, from May 13 (YD 133) to June 21 (YD 172), 1995. The incoming and outgoing shortwave, longwave, and the net all-wave radiation are measured directly, and both the sensible and latent turbulent heat fluxes are measured directly by eddy correlation. Results from this fieldwork are presented as an energy balance climatology, mainly using ensemble averages. The findings are compared with results from midlatitude suburban studies.

The complete, directly observed suburban radiation balance is one of very few available. In conjunction with these data, derived surface characteristics, such as temperature, albedo and emissivity (ε_o) are given. The clear sky midday albedo is observed to be 0.17, and ε_o is estimated to be 0.97. Parameterizations to calculate various energy fluxes are evaluated using the Miami data. These include formulae to calculate the net radiation and incoming shortwave and longwave radiative fluxes, under both clear and cloudy sky conditions. Of the radiative formulae tested, the calculation of incoming shortwave from the net radiation is particularly effective, especially under cloudless skies. In contrast, some of the incoming longwave radiation equations are essentially useless in cloudy conditions.

The sensible, latent, and storage heat fluxes are each presented as ensemble averages, and as fractions of the net radiation. The average daytime sensible heat flux normalized by the net radiation is 0.43, which is in the middle of the range of previous urban observations. The average daytime latent heat flux normalized by the net radiation is 0.27, which is reasonably similar to midlatitude suburban observations. The storage heat flux appears to play a significant

role, although this is linked to the fact that it is calculated as a residual from, among others, the (low) latent heat flux. The average daytime storage heat flux normalized by the net radiation is 0.30, which is similar to the highest of such observations from other cities.

Two energy partitioning parameters, the Bowen ratio (β) and the Priestley-Taylor α, as well as the McNaughton-Jarvis coupling factor (Ω), are used to gain insight into Miami's energy regime, and to more thoroughly compare it to those previously observed in other North American cities. The subtropical location is not found to significantly alter the urban energy balance partitioning, although some differences are noted. The Priestley-Taylor and Penman-Monteith parameterizations, which relate evaporation to available energy possess utility, whereas calculations using the aerodynamic approach that rely on empirical estimates of the surface roughness for heat as a fraction of that for momentum, are of questionable merit. The daytime average values of β, the Priestley-Taylor α, and Ω are observed to be 1.55, 0.51, and 0.4 respectively.

Given the hot, wet location relatively high latent heat fluxes (evaporation) were anticipated, but not found. The Penman-Monteith equation was used as a framework to investigate the most likely reasons for this. This analysis provides support for the suggestion that the small vapour pressure deficit in Miami is a major part of the explanation for the unexpectedly low latent heat fluxes.

TABLE OF CONTENTS

CHAPTER 2. METHODOLOGY

LIST OF TABLES

LIST OF FIGURES

ACKNOWLEDGEMENTS

The successful completion of this project would not have been possible without the generous assistance of a number of people and organizations.

I will always be indebted to my supervisor, Dr. Tim Oke, for his constant support, patience, and encouragement. He has always made himself available to plan fieldwork, answer questions, and refine presentations. Moreover, he is a gentle man and an inspiring scientist. Dr. Sue Grimmond of Indiana University has provided vital guidance in planning fieldwork and analyzing data, in addition to lending laboratory space, several instruments, and a 40 m portable pneumatic tower. She also brought her expertise and a backup datalogger, both much-needed, to Miami during data collection. I am thankful to Dr. Ian McKendry for graciously agreeing to read my thesis promptly, during a busy time of year.

I would like to thank Dr. Matthias Roth for his assistance in analyzing the 3-D anemometer data, but really it was I who assisted him in that endeavor. His knowledge and efforts were essential in the processing of these data.

Many thanks go to Mark Hubble and Tom King for providing a friendly place to stay in Bloomington. Additional thanks are due to Mark for his hard work, ingenuity, and encouraging presence during instrument testing in Bloomington and installation in Miami. I am also grateful to Andres Soux and Ron McTaggart-Cowan for their tireless assistance in transit and onsite, and to Andres, as well as Drs. Jamie Voogt and HaPe Schmidt, for providing useful discussion. Elena Scali assisted in the preparation of several spreadsheets and figures. Eric Leinberger digitized and prepared several figures.

Auxiliary data were kindly provided by the City of Miami, the Miami-Dade Water and Sewer Authority, and Dade County. The Dade County Youth Fair and Exposition furnished an excellent field site, in addition to generous amounts of office space and Southern hospitality. Funding for this research has been provided to Dr. T. R. Oke by Natural Sciences Engineering Research Council of Canada. Personal funding was provided through University of British Columbia Teaching and Research Assistantships in the Department of Geography.

I am especially grateful for the love and support I have received from my family and the Lord family. The Lords also provided a crucial site, and food, drink, and good company.

CHAPTER 1. INTRODUCTION

1.1 The Energy Balance Context

Land surface and atmospheric alteration by urbanization leads to the development of distinct urban climates with features such as the urban heat island, urban-induced wind circulation, precipitation enhancement downwind of urban areas, and air pollution. Ultimately such urban climate effects are due to differences between urban and pre-urban budgets of heat, mass, and momentum. Thus it is necessary to add knowledge of the surface energy balance of urban areas to the already well-developed understanding of the boundary layer meteorology and climatology of rural areas (Grimmond and Oke 1995). To this end, surface energy balances have been measured and studied in several cities over the past two decades.

1.1.1 Urban Surface Radiation Budget

The surface energy balance is forced by the exchange of radiation between the sun, atmosphere, and the surface. The surface radiation budget consists of five terms, which can be separated into three categories based on wavelength. The net all-wave radiative flux density (Q^*) is equal to the sum of the net shortwave flux density ($K^* = K\downarrow - K\uparrow$) and the net longwave flux density ($L^* = L\downarrow - L\uparrow$). The upwelling and downwelling shortwave fluxes ($K\uparrow$ and $K\downarrow$) refer to radiation in wavelengths ranging from 0.15 to 3.0 μm, and the two longwave fluxes, $L\uparrow$ and $L\downarrow$, consist of radiation between 3 and 100 μm (Oke 1987). The radiation budget therefore is:

$$Q^* = K\downarrow - K\uparrow + L\downarrow - L\uparrow \qquad (\mathrm{W\ m^{-2}}), \qquad (1.1)$$

where $K\downarrow$ is the incoming shortwave radiative flux density, which in essence is the intensity of sunlight striking the surface. This is affected by the angle of incidence of solar radiation, which, assuming a flat, level surface, is a function of latitude, time of day, and time of year at which observations are made. $K\downarrow$ is lessened by the presence of clouds, pollution or other atmospheric constituents, which can scatter, reflect or absorb sunlight before it reaches the surface. It is occasionally possible for clouds to increase $K\downarrow$ at a given location, by reflecting to that location radiation that would otherwise have travelled elsewhere.

$K\uparrow$ is the outgoing (reflected) shortwave radiative flux density. It depends on $K\downarrow$, because clearly the more incident sunlight that arrives at a surface, the more can be reflected from it, and upon the surface albedo (α), which is the spectral reflectivity integrated across the whole shortwave band ($K\uparrow = K\downarrow\alpha$). In the shortwave, light coloured brick, tile, concrete, and white-painted surfaces are among the most reflective urban materials, that can reflect up to 40%, while dark coloured materials such as asphalt may reflect as little as 5% of incident sunlight (Oke 1987; Sass 1992; Bretz *et. al.* 1998). Many surfaces, especially water and glass, and including cities in general, reflect a greater proportion of incoming shortwave radiation when the sun is low in the sky (or the local zenith angle is large) than during the middle hours of the day. The integrated urban albedo typically varies from about 20% near sunrise and sunset, to roughly 15% at midday (Oke 1988). Although $K\uparrow$ is not a constant fraction of $K\downarrow$, it is common to use the value during the middle of the day (when energy input is greatest) to characterize α for a surface.

$L\downarrow$ is the incoming longwave radiative flux density, which is infrared radiation emitted towards the surface by the atmosphere and clouds. Under clear skies, increases in atmospheric

temperature and humidity increase $L\downarrow$. The presence of clouds, particularly low-level (warm) clouds, produces even more significant increases.

$L\uparrow$ is the outgoing longwave radiative flux density. It is infrared radiation emitted upwards by a surface as a function of its temperature (T_o) and emissivity (ε_o), plus a small amount of $L\downarrow$ that is reflected, i.e. $L\uparrow = \varepsilon_o \sigma T_o^4 + (1 - \varepsilon_o) L\downarrow$. The warmer a surface, the larger is $L\uparrow$, but certain surfaces, especially metallic such as corrugated iron roofs, have unusually low surface emissivities that cause them to emit much less than would other surfaces with the same temperature. Temperatures calculated from $L\uparrow$ without exact knowledge of ε_o are apparent, not true, surface temperatures.

As stated, the sum of the four individual radiative terms is the net all-wave radiative flux density, Q^*. When Q^* is positive, the net transfer of radiative energy is towards the surface (usually downward). When Q^* is negative, the net radiative flux is upward, away from the surface.

1.1.2 Urban Surface Energy Balance

The urban surface energy balance can be expressed theoretically as

$$Q^* + Q_F = Q_H + Q_E + \Delta Q_S + \Delta Q_A \qquad (\mathrm{W\ m^{-2}}), \tag{1.2}$$

where Q^* is the net all-wave radiation or surface radiation budget, Q_F is the anthropogenic heat flux density due to combustion releases, Q_H is the turbulent sensible heat flux density, Q_E is the turbulent latent heat flux density, ΔQ_S is the net heat flux density stored in urban materials, and ΔQ_A is net horizontal heat advection.

In most energy balance studies conducted during the past two decades, Q^* has been measured directly by radiometry, yielding reasonable data. Q_F is reasonably small typically

varying from 15 to 50 W m^{-2} (Oke 1988). Presumably Q_F is manifested as plumes of warm air and water vapour exuded by vehicles and building vents, and infrared radiation from the warmer fabric. In an observation study Q_F should not be measured independently because it is already present in urban Q_H, Q_E, and Q^* measurements. It is not obvious how one could extract it from those measurements. Measurement of Q_H and Q_E is best conducted directly and simultaneously by eddy correlation. In the absence of a practical, accurate measurement technique, ΔQ_S has to be solved as a residual in (1.3) if the other terms have been measured. Usually energy balance observations are made at sites that are sufficiently extensive and quasi-uniform horizontally so that ΔQ_A can be considered negligible, as is assumed to be the case for the site in this study. Therefore in practical terms the measured urban surface energy balance is:

$$Q^* = Q_H + Q_E + \Delta Q_S \qquad \text{(W m}^{-2}\text{)}, \qquad (1.3)$$

where the first three terms are measured directly, and ΔQ_S is calculated as a residual.

1.2 Previous Urban Observations

1.2.1 Radiation

The present study is the first published wherein all five terms in (1.1) have been independently measured in a city. Several studies have evaluated the five radiative fluxes in cities, but have calculated one or more of them by parameterization and/or as a residual, using (1.1). The 1976 METROMEX study in St. Louis included direct observations of $K\uparrow$, $K\downarrow$, and $L\uparrow$ during daylight hours, calculated $L\downarrow$ from a formula, and solved Q^* as the sum (White *et al.* 1978). A pair of two-day studies in Bonn, Germany in 1982 and 1983 calculated Q^* with a model, tuned with spot observations of $L\uparrow$ and direct and diffuse $K\downarrow$ (Kerschgens and Hacker 1985; Kerschgens and Drauschke 1986). Several studies have

observed urban α, and results from over a dozen of these are tabulated by Oke (1988). He shows a fairly narrow range of values, and suggests 0.14 and 0.15 as typical values for urban and suburban areas, respectively. Oke's proposal that tropical urban α values might be somewhat higher will be shown to be correct.

Urban–rural radiation comparisons have tended to focus on the downward fluxes. There are many studies on the attenuation of $K\downarrow$ by polluted urban atmospheres (see references in Table 1 of Oke 1988), $K\downarrow$ together with $L\downarrow$ (Estournel *et al.* 1983), and $L\downarrow$ alone (Oke and Fuggle 1972). Less commonly there are studies of urban and rural $L\uparrow$, as in the Russian studies by Berlyand *et al.* (1974) and Kondratyev *et al.* (1976), and by Yap (1975) who showed the sensitivity of urban-rural $L\uparrow$ differences to small differences in ε_o. These studies and others like them have significantly improved the level of understanding of urban climate, by describing the role of $L\downarrow$ in urban heat island formation (increased urban versus rural $L\downarrow$ is an effect, not a cause, of the urban heat island) and by detailing, for example, the rather wide range of attenuation levels that pollution can impose on $K\downarrow$ (Oke 1988).

Urban modifications of the individual fluxes are offsetting:

(a) $K\downarrow$ is decreased by pollution, which reflects, absorbs, and scatters a portion of it before it reaches the surface, but

(b) $L\downarrow$ is increased by the presence of pollutants thus warmed, and by the warmth of the urban boundary layer (UBL, see Oke 1988).

(c) $K\uparrow$ is decreased, due to low α values of typical roofing materials and to the trapping tendency of urban geometry (Aida 1982; Aida and Gotoh 1982; Arnfield 1982), but

(d) $L\uparrow$ is increased by the warmer urban surface.

Thus the urban surface receives less $K\downarrow$ than the surrounding rural areas, but more of it is absorbed; urban $L\uparrow$ emission is greater, but so is $L\downarrow$ counter radiation. Urban–rural comparisons of the net result of these changes (Q^*) are therefore not easily encapsulated.

The present study provides a comprehensive illustration of the radiation balance of the sub-tropical city of Miami, FL by presenting direct observations of the five terms, made continuously over a period of five weeks. Previously unpublished radiation observations from a three-week period in the summer of 1978 in Vancouver, B.C. are also included. In Vancouver, $K\downarrow$, $K\uparrow$, and Q^* were measured directly, while $L\downarrow$ was calculated from observations of ($K\downarrow + L\downarrow$), and $L\uparrow$ was calculated as a residual (Steyn and Oke 1980).

1.2.2 Non-radiative Terms

Accurate measurement of the convective terms Q_H and Q_E has proved more difficult than that of the radiative fluxes, but in recent decades advances in micrometeorological theory and electronic technology have improved matters. Currently researchers are more able to make reliable measurements of these two turbulent fluxes. Appropriate equipment is more dependable and commercially available, and improvements continue to be made. Special significance is attached to the development and availability of eddy correlation equipment, which can now be used on an almost routine basis.

1.2.2.1 Early Efforts

Before eddy correlation was developed and accepted as a preferable tool for micrometeorological research, Bowen ratio (β) measurements were the primary source of turbulent energy flux data. The Bowen ratio-energy balance method of estimating turbulent

fluxes was used in several studies which are significant for their contribution to our understanding of energy partitioning in urban areas. They were conducted in suburbs of Montreal, Canada, and Uppsala, Sweden (Oke 1978), Vancouver, Canada (Kalanda *et al.* 1980; Oke and McCaughey 1983), and Bonn, Germany (Kerschgens and Hacker 1985; Kerschgens and Drauschke 1986). Pre-eddy correlation energy balance observations have also been made in downtown areas; in Uppsala (Taesler 1980) the aerodynamic approach with stability correction was used.

The aerodynamic approach, like the Bowen ratio-energy balance method, requires the accurate measurement of vertical gradients, but in cities, where turbulent mixing is enhanced by the warm, rough surface, these gradients can be small enough to place great demands on instrument precision. Another requirement of the aerodynamic approach is the specification of the nature of the surface, particularly its roughness and displacement lengths, which in cities is a difficult task (Oke 1988; Grimmond and Oke 1999b).

Bowen ratio measurements require that the turbulent diffusivity of heat (K_H) equal that of water vapour (K_V), and while this holds in areas with extensive homogeneous surfaces (and for moderate stability regimes, Oke 1987), it does not hold over heterogeneous surfaces such as cities (Roth and Oke 1995). This is because over urban surfaces, water and heat availabilities change disproportionately in space; an eddy may travel over a park and entrain heat and water vapour, but then it may encounter a paved surface, and cease to entrain water vapour while continuing to gain heat. Thus, as an eddy moves from a park to a street, the change in heat availability is unlikely to equal the change in water availability, so those two quantities' chances of being transported by turbulence change unequally.

In addition to being heterogeneous in terms of availability of water and heat, urban surfaces are rough. They are composed of tall buildings spaced with varying degrees of regularity, which promote vertical motion between the surface layer and the mixed layer, and up to the entrainment zone at the base of the overlying inversion. This means hundreds of metres of strong vertical motion—an effective way to drive evaporation, by bringing either relatively moist air upward or relatively dry air down to the surface. Such organized convection due to non-local transport is not built into most surface layer theory or expectations for flux-gradient methods which assume equality of K_H and K_V.

Conditions of patchy cloud cause further inequalities between K_H and K_V, as air parcels move over patches of sunny and shaded ground. Under these circumstances, water availability might be reasonably constant, but heat availability could change significantly through space, and the locations of cool and warm patches of ground vary with time as the clouds move. Thus Bowen ratio measurements are less than ideal in urban landscapes, which are of course spatially heterogeneous even under clear skies (Roth and Oke 1995).

The combination of physical obstruction causing mechanical up- and downdrafts, and the patchwork of thermally-contrasting surfaces causing convective thermals, provides an optimal environment for vertical coupling between the surface layer, the planetary boundary layer (PBL), and the free atmosphere.

Another difficulty peculiar to cities is that the measurement of ΔQ_S is more complex than simply installing an array of heat flux plates and thermocouples, as can be done in rural areas to measure the ground heat flux (Q_G). Parameterization is the preferred method of obtaining the estimates of ΔQ_S that are required in the Bowen ratio-energy balance approach. This usually

involves the use of measured Q^* and detailed description of the surface land cover so that composite empirical relations between Q^* and ΔQ_S can be applied. The initial land cover survey is relatively laborious, but the method can produce satisfactory results (Oke *et al.* 1981; Grimmond *et al.* 1991; Grimmond and Oke 1999a) and can facilitate closure of the urban energy balance by the calculation of Q_E as a residual, if it is not measured directly. This became feasible as fast response wind and temperature sensors became easier to acquire and as their reliability improved, allowing for direct measurement of Q_H. Enlightening studies employing this tactic have been conducted in suburban areas of Vancouver, Canada (Cleugh and Oke 1986; Grimmond 1992), and Mexico City, Mexico (Oke *et al.* 1992). Similarly illuminating observations were made in downtown Indianapolis, Indiana (Hanna and Chang 1990), where again Q_H was measured directly, and Q_E was not.

1.2.2.2 Eddy Correlation and Modern Methods

Eddy correlation involves direct measurement of fluctuations in vertical wind speed and a quantity, such as temperature or specific humidity, which is related to the flux of interest, e.g. heat or moisture. The time-averaged product of the instantaneous fluctuation of vertical wind speed (w') and that of air temperature (T') or specific humidity (q') can be used to calculate Q_H or Q_E. These fluctuations must be measured by fast response instruments, since significant contributions to the flux occur on time scales down to the order of tenths of seconds. Because the technology required to build such instruments did not exist, direct measurement of the turbulent fluxes was not possible until the 1950s, was not done until the 1960s, and was not done often until the 1980s, by which time researchers could reasonably hope to acquire and operate the equipment required to measure Q_H and Q_E by eddy correlation. The first use of eddy

correlation observation in cities was by Oke *et al.* (1972) in Montreal, PQ and by Yap in Vancouver, B.C. (Yap 1973; Yap and Oke 1974).

Direct, simultaneous measurement of Q_H and Q_E is the preferred alternative to the above profiling and parameterizing compromises, because it minimizes reliance upon empirical estimates of various elements of the urban surface. Measurement of both turbulent fluxes was not a viable option until reliable fast-response hygrometers became available; this occurred soon after the emergence of sonic anemometers. In suburban Adelaide, Australia, Q_H and Q_E were both measured directly (Coppin 1979), but seldom simultaneously. That early study was plagued by equipment malfunctions and shortcomings, including the problem of finding a data recorder capable of rapidly receiving and storing the huge amounts of raw data produced by fast response instruments. Very few urban climatologists faced these difficulties prior to 1979; this research in Adelaide is one of the earliest urban studies to use a fast-response hygrometer and to attempt direct measurement of both turbulent fluxes. Another pioneering effort was made using this approach in commercial and suburban areas of St. Louis, Missouri (Clarke *et al.* 1982; Ching *et al.* 1983), but only a few days' worth of data were obtained.

Several other noteworthy studies have since employed direct measurement of Q_H and Q_E in suburbs of: Sacramento, California (Grimmond *et al.* 1993), Vancouver (Roth and Oke 1994), Chicago, Illinois (Grimmond *et al.* 1994), Tucson, Arizona, and Los Angeles, California (Grimmond and Oke 1995), and in downtown Mexico City (Oke *et al.* 1999a). In the Ginza district of downtown Tokyo, both turbulent fluxes were measured directly by eddy correlation, and Q_H was also observed by scintillometer (Kanda *et al.* 1997, 1999).

The scintillometer uses radiation to observe Q_H. The path length of the scintillometer depends on the placement of the two separate transceiving heads, but it can be on the order of 1 to 2 km, producing measurements that are integrated over a considerable distance. This is desirable because data then apply to an area rather than essentially a single point (typical eddy correlation path length ~ 0.15 m), thus diminishing the likelihood that observations will be overly affected by individual roughness element-sized eddies. The advantage of inherent spatial averaging in Q_H observations by scintillometer is presently offset by two practical shortcomings: the instrument is expensive, and difficult to install in the field. The former concern will probably decrease with time and technological advances, but the second is a serious difficulty, particularly for suburban sites. The transceiving heads must be very accurately aligned in order to make measurements, so placing them for example on a pair of 20 m towers erected 200 m apart would likely not suffice, because of small differences in the direction and frequency of each tower's swaying. Kanda *et al.* (1997, 1999) avoided this problem by installing the instrument on adjacent buildings in their densely urbanized study areas.

1.2.2.3 Energy Balance Characteristics

The main findings of Roth and Oke (1994) involve comparison of ΔQ_S calculated as a residual and as determined by the OHM urban heat storage model (Grimmond *et al.* 1991). The model is found to be of value but to have distinct shortcomings. Therefore a caveat is included, warning against attaching too much value to comparisons between Q_E observations using eddy correlation and those calculated as a residual, using OHM-modelled ΔQ_S and direct measurements of Q^* and Q_H. A cautionary note is also given regarding comparisons between

direct measurements of Q_E and those obtained using the Bowen ratio-energy balance method, in light of the fact that the eddy diffusivities of heat and moisture are not equal in cities.

The fairly broad range of β observed at Vancouver during the 1980s is attributed to both the variety of techniques used and the range of climate conditions at that suburban site (Roth and Oke 1994).

Roth and Oke (1994) observed a Q_E 'tail', meaning that Q_E remains positive for about four hours after sunset, a phenomenon absent in many previous studies (e.g. Cleugh and Oke 1986; Grimmond 1992). Grimmond and Oke (1995) also observed a Q_E tail in Sacramento, Tucson, and Chicago, but unlike Roth and Oke (1994), did not observe a Q_H tail. Both studies made similar observations of the diurnal variation of the residual flux, ΔQ_S, which peaked earlier than the other fluxes, and was the first one to become negative, in the afternoon. The 1995 study found similar flux ratios to the mean values proposed earlier by Oke (1982, 1988), but this agreement was not overly convincing, so new values were suggested, with separate β for cities with and without frequent summertime precipitation.

The urban energy balance has been investigated using a consistent and sound methodology across a range of climatic zones, from desert (Tucson) and Mediterranean (Los Angeles, Sacramento) through moist continental (St. Louis, Chicago) to marine west coast (Vancouver). The aim of the present research is to extend this spectrum of knowledge to include the wet tropical case, by presenting observations from Miami, Florida.

1.3 The Importance of Tropical Urban Climate Study

Specific knowledge of tropical urban climate is important for three main reasons, in addition to scholarly interest: firstly, a great many people live in tropical cities, and these

populations are, and will continue to, increase dramatically over the next several decades; secondly, tropical cities are already inhospitable due to a host of factors; thirdly, the first will greatly exacerbate the second.

It is estimated that nearly half of the world's population lives in cities, and that three of the world's five cities of over 20 million people, and 17 of the 26 cities of over 10 million are located in tropical climates (Oke *et al.* 1990/91). Urban populations in Asia and Africa are projected to increase by 2.3 billion from 1990 to 2025, which is equivalent to the total urban population for the globe in 1990 (Cleugh 1995). It is also noteworthy that the projected urban population increase for Asia alone from 1990 to 2025 is about ten times the urban increase in the U.S. from pre-1900 to 1985 (Karl *et al.* 1988).

The basic infrastructure of most tropical cities, as well as less crucial civic features such as emissions legislation and enforcement, were woefully inadequate a decade ago, and now, as populations and pollution plumes mushroom, living conditions are more threatening than ever. Many tropical cities experience very weak ventilation, giving poor dispersion (Oke *et al.* 1990/91), and recent studies show that this is likely compounded by a favouring of ΔQ_S at the expense of Q_H (Oke *et al.* 1999a), casting doubt upon hopes that at least one benefit of higher temperatures would be better pollutant dispersal. Also, high levels of tropical insolation increase the potential for formation of photochemical smog. These are contributing factors to the observed trend of respiratory, cardiovascular, and cancerous diseases replacing infectious and parasitic diseases as the main cause of death in many tropical cities (Weihe 1986).

Another tropical health threat that is aggravated in cities is high air temperatures, which are effectively elevated in terms of human comfort by high humidity levels. It has been observed

in mid-latitude cities that heat stress during the summer can lead to increased morbidity and loss of productivity, and in extreme cases to death from heat stroke or fatal aggravation of cardiovascular weaknesses. Tropical residents may be more tolerant of high temperatures than those in cooler climates, but they are by no means immune to thermal discomfort and the above problems (Kalkstein and Smoyer 1993). In addition, the large release of ΔQ_S in the evening seriously compromises the opportunity to recover from the day's heat, as well as significantly boosting energy consumption in more affluent areas (Oke *et al.* 1990/91). Urban heat also appears to increase the incidence of homicide and suicide, as has been observed in several cities (PAHO 1967).

1.4 A Brief History of Tropical Urban Climate Study

Observations have been made previously in cities that are or can be considered 'tropical', and although recently these projects have included flux measurement, earlier studies were descriptive or theoretical, or relied on data from standard weather stations. In Kuala Lumpur, Malaysia, atmospheric temperature profile measurements and analysis of both suburban and rural climate records led investigators to conclude that unlike in mid-latitude cities, wind speed was only a minor factor in urban heat island development of an equatorial city, particularly at night (Sham Sani 1980). This is simply because observed wind speeds were quite low, with nocturnal winds ranging from 0 to 0.5 m s^{-1}. As well as wind speeds, mixing heights were lower in Kuala Lumpur than they tend to be in mid-latitude cities, implying a high potential for air pollution problems (Zeuner 1983).

Another difference between tropical and mid-latitude urban climates is the relative prominence of 'thermal discomfort' for those living in the tropics. The 'humiture' is an index that

relates air temperature (T_a) and relative humidity (RH) to how hot it feels to humans. The humiture is given by an equation developed by G. Winterling:

$$T_h = T_a + (e_a - 21) \qquad (°F), \qquad (1.4)$$

where e_a is the near-surface water vapour pressure in mb (Ahrens 1991). A similar system called the heat index was implemented by the US National Weather Service in 1984; it uses the term 'apparent temperature' rather than humiture (Ahrens 1991). People are said to experience thermal discomfort at apparent temperatures above 24.5 °C (Sham Sani 1977).

Tropical urban-rural temperature difference studies have also been done in India and Mexico. Three Indian cities have been thus examined: Poona (Padmanabhamurthy 1979), Bombay (Daniel *et al.* 1973, Pradhan *et al.* 1976), and Delhi (Padmanabhamurthy 1981). The latter used dew point temperature comparisons to show that the absolute humidity was lower in the city than in surrounding rural areas; this difference has also been observed in Ibadan, Nigeria (Adebayo 1991). Jáuregui (1973) has conducted temperature difference studies in Mexico City, as well as general urban climate studies, including such topics as urban enhancement of precipitation (1982).

These simple observations enabled investigators to confirm that many climatological features observed in the mid-latitudes are also present in the tropics, leading to the initial impression that if the same physical processes are present, some climate features may be qualitatively transferable to other tropical cities (Zeuner 1983). It is further noted by Zeuner that the few studies undertaken in tropical cities are insufficient to make generalizations for any climatological parameters, and while the situation has improved in the ensuing 16 years, there are for example no wet tropical urban flux observations with which to compare the present results.

The 1970s saw a significant increase in the number of papers being published on urban climate in the mid-latitudes (Oke 1990), and in the 80s this boom was echoed in tropical urban studies (Jáuregui 1992). During the 70s, tropical studies constituted only 2% of the total number of urban climate papers published (Jáuregui 1986), while in the 80s this figure increased to 21%, with an additional 12% of papers devoted to developed subtropical cities, primarily located in the U.S. and South Africa. This increase appears to have leveled off regarding work in the tropics, with a moderate increase in the subtropics; in the 90s, up to and including 1995, 20% of published urban papers were tropical, with subtropical studies constituting another 19% of the total (Jáuregui 1996).

Atwater (1977) used a numerical model to study urban effects in a wide range of climate zones and concluded that anthropogenic heating is a significant contributor to urban heat islands in tundra and mid-latitude climate regions, whereas pollutants, regardless of the overall climate, are minor contributors. Presently, anthropogenic heating is not widely considered to be a significant portion of the urban energy balance, but the conclusion that pollutants play a minor role in urban thermal structure still holds. Overall, Atwater found the largest urban thermal effects were in tundra regions, while the smallest were in the tropics and deserts, but this is contradicted by subsequent investigations.

In the early summer of 1990 in Tucson, Arizona, an energy balance study was conducted, with eddy correlation measurements of Q_H and Q_E (Grimmond and Oke 1990). The findings included larger urban-rural differences than had been observed in temperate regions. At 32°07'N, Tucson, like Miami at 25°44'N, does not meet the latitudinal definition of a tropical

city, but it is hot enough in summertime that it can be said to have a tropical climate; Miami qualifies year-round.

Mexico City, at about 19°N, is in the tropics, but because of its fairly high elevation (~ 2250 m) its climate is classified as highland tropical. In a 1985 study there, in a mixed residential/commercial/industrial area in the Tacubaya district, Q_H was measured by eddy correlation, ΔQ_S was parameterized, and Q_E was calculated as a residual from (1.3). Results from that investigation (Oke *et al.* 1992) are quite similar overall to those from residential areas in cities with temperate climates, but in Mexico City the role of heat storage was found to be significantly higher (and that of Q_H smaller) than in temperate cities. Further, in Tacubaya, as in Tucson, irrigation and other anthropogenic uses of water were seen to be major contributors to urban Q_E.

Another Mexico City study was conducted in late 1993, in the mixed institutional/commercial old city district, about 6 km to the east of the Tacubaya site. This time Q_H and Q_E were both measured by eddy correlation, and ΔQ_S was calculated as a residual (Oke *et al.* 1999a). Results were similar to those of the earlier study, with ΔQ_S playing a large role at the expense of Q_H, although nocturnal release of heat from storage enabled Q_H to remain positive virtually all the time. This, in conjunction with some reasonable assumptions about the energy balance of the rural areas surrounding Mexico City, led investigators to conclude that Q_H is likely smaller in the city than outside it, and that this relation might well hold for cities in general.

Preliminary urban energy budget studies have also been undertaken in tropical cities in India (Padmanabhamurthy 1990) and Africa (Adebayo 1990).

1.5 Objectives of the Present Study

The present research includes the first direct simultaneous observations of Q_H and Q_E in a wet tropical city. Central to this study is a presentation and explanation of data describing the components of the surface energy balance of Miami, including:

- analysis of component fluxes and derived variables relating to the radiation budget of the surface
- a climatology of the separate energy balance components and derived statistics such as the Bowen ratio, Priestley-Taylor α_{PT}, and the McNaughton-Jarvis coupling factor (Ω)
- assessment of the relative roles in the balance played by each flux, and comparison with results from other cities
- development of parameterizations of the fluxes
- explanation of any special features which emerge from the observations.

However, before the above points are covered, the following chapter will present the sites, instrumentation, and methodology used in the study.

CHAPTER 2. METHODOLOGY

2.1 Tropical Climate

A strict definition of a tropical city is one that lies between the Tropic of Cancer, at 23°27'N, and the Tropic of Capricorn, at 23°27'S, but this is as arbitrary as it is oversimplified. A more meaningful definition is climate-based; the chief characteristics of tropical climates are high temperatures, uniformity of annual temperature variations and air masses, and high spatial variability of humidity and precipitation (Zeuner 1983; Jáuregui 1986). Unlike many other tropical areas of the world, tropical America (consisting of the Caribbean region, Central America, and northern portions of South America) lacks a general monsoon system because the inter-tropical convergence zone (ITCZ) shows smaller variations with latitude than in tropical Africa and Asia (Okabe 1995). This is due mainly to the cool Humboldt current in the eastern Pacific and the reduced land mass area north of the equator (Zeuner 1983).

2.1.1 Climate of South Florida

Southern Florida is bounded on three sides by the sea and therefore has a maritime climate. Trade winds from the east bring warm, humid, near-surface air to the region, but above 1 – 1.5 km in winter or 2 km in summer, inversions weaken vertical uplift, particularly in winter. The maximum rainfall occurs during summer and is related to disturbances in so-called easterly waves, or in hurricanes traveling over the area (Zeuner 1983). In the absence of synoptic precipitation, the primary control for summertime rain shower development is low-level, mesoscale convergence (Pielke 1984). Typically, buoyant energy accumulates during the morning, presumably due to sea-breeze convergence (Pielke 1984), then downdraft-induced

convergence sustains cumulus convection until the available buoyant energy is used up (Cooper *et al.* 1982). A related explanation is that the merger and intersection of thunderstorm-produced outflow boundaries are the main sources of low-level convergence for subsequent deep cumulus convection (Purdom and Marcus 1982).

2.2 Study Area

The observations for the present study were made in a suburban area of Miami (25°44'N, 80°22'W). The southeastern edge of the Florida peninsula is essentially a north–south oriented strip of land about 15 to 25 km wide and 150 km long, with Miami situated approximately 50 km north of the southern end. This strip is bounded by the swamps of the Everglades to the south and west, and by the Atlantic Ocean to the east. The land is quite

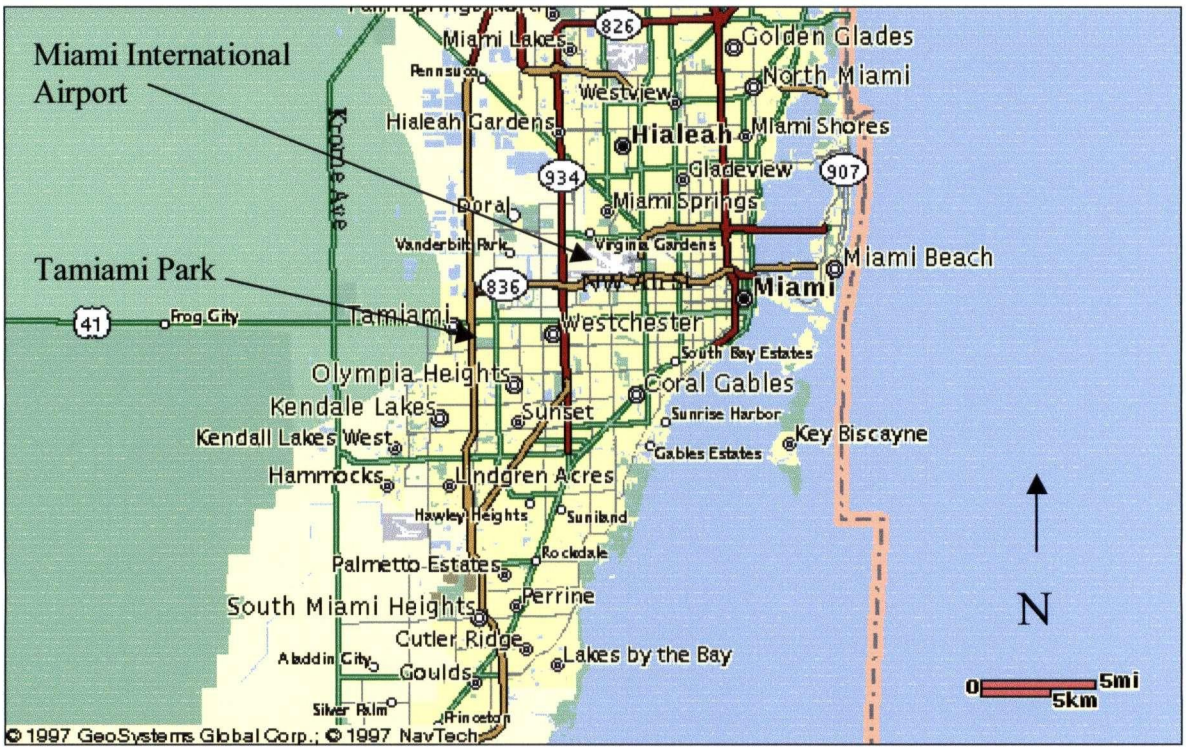

Fig. 2.1 Miami, Fl. and environs. The downtown core is labelled **Miami**, with a black bullseye. At Miami International Airport, screen level observations of standard climate variables are made hourly by onsite officials. Tamiami Park is the green rectangle indicated, and the study sites are at and near the southeast corner of it.

flat, with a high water table, and many lakes and canals. The greater Miami area (Fig. 2.1) has no natural topographic features over 2 m in elevation.

The natural vegetation is marsh grasses in marine areas (adjacent to swamps and canals), and in less wet regions, palm and ficus trees, and leafy fruit trees and bushes. South Florida has a hot-dry climate in winter and a hot-wet climate in summer.

Two sites were established in western Miami. One, called Fairground, was the location of the main turbulence tower and instrumentation. The second, called Residential, was located slightly upwind of fairground to sample the upwelling radiative fluxes in the turbulent source area.

2.2.1 Residential Site

The Residential site is located in the backyard of Jim and JoAnne Lord, who live in a single-story house at 2800 SW 104 Court, Miami, about 700 m southeast of the southeast corner of Tamiami Park (Figs 2.2, 2.3). The backyard is grassed, and although it is not regularly irrigated, it remains green. Several large, leafy trees are present, with heights of 2 to 8 m. The three houses in the immediate area (the Lords' and two neighbours') have white stucco walls, and reddish-brown roofs. Two of the houses have tar and paper shingle type roofs, while the other has a ceramic tile roof. Three light-coloured aluminium garden sheds are present as well.

2.2.2 Fairground Site

The Fairground site is an out-of-season county fairground, the Dade County Youth Fair, located at 10901 Coral Way, Miami, on the eastern half of Tamiami Park (Figs 2.2, 2.3). The Fairground consists of many trees and interspersed grassed and paved surfaces, and a few buildings (Fig. 2.4). In the immediate vicinity of the tower (i.e. the northwest quadrant,

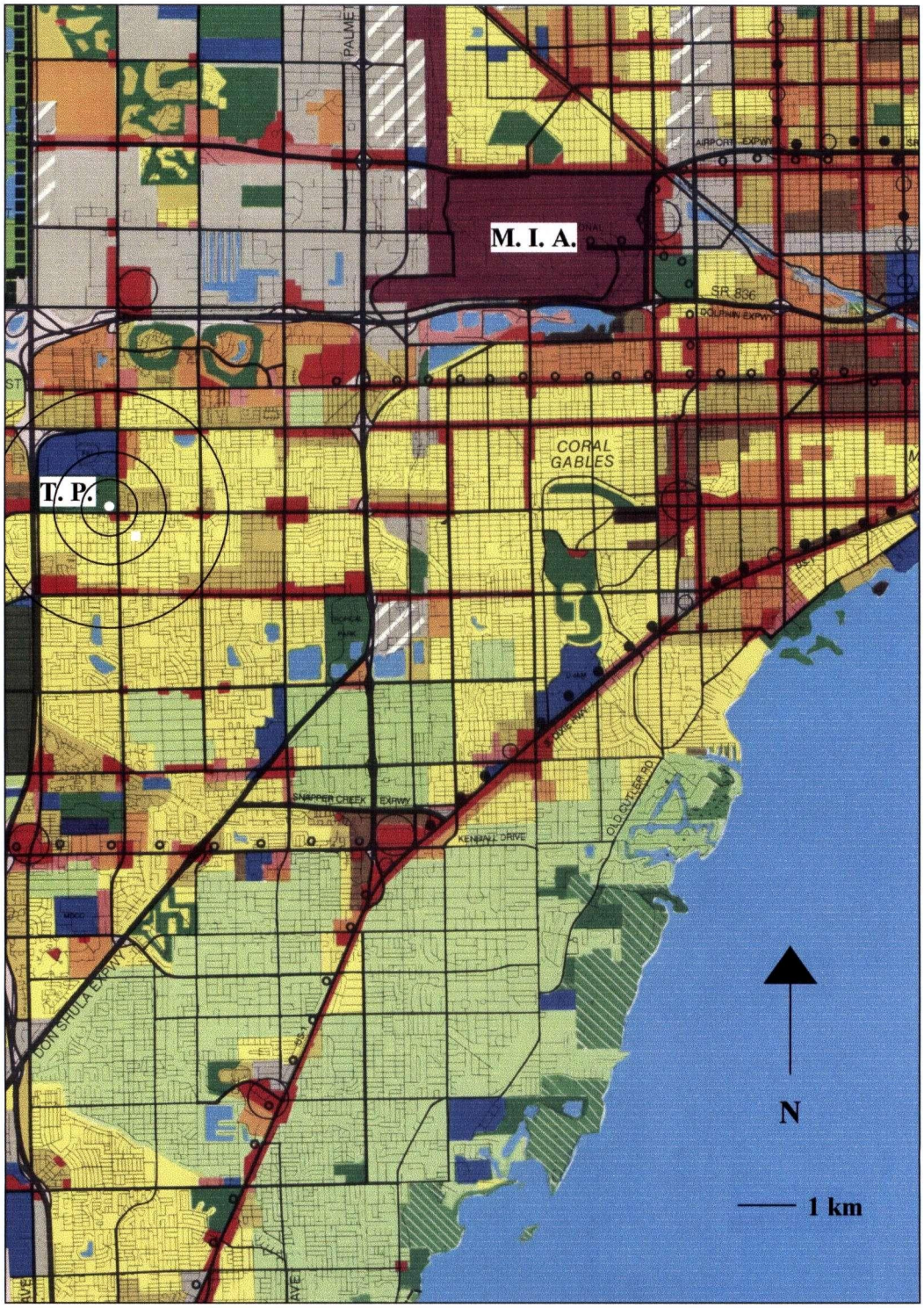

Fig. 2.2 Land use map of west-central Miami. See next page for legend. Miami International Airport (M.I.A.) and Tamiami Park (T.P.) are labelled. The white circle at the southeast corner of the park is the Fairground site, and the Residential site is the white square slightly to the southeast of the park. Circles around the Fairground site have radii of 0.5, 1, and 2 km. The Atlantic Ocean occupies the southeast corner of the map. Because prevailing winds are from the southeast, both the airport and the park have a suburban fetch of about 10 km.

ADOPTED 2000 AND 2010 LAND USE PLAN FOR METRO-DADE COUNTY, FLORIDA

RESIDENTIAL COMMUNITIES

ESTATE DENSITY	UP TO 2.5	DWELLING UNITS PER GROSS ACRE
LOW DENSITY	UP TO 6	DWELLING UNITS PER GROSS ACRE
LOW-MEDIUM DENSITY	UP TO 13	DWELLING UNITS PER GROSS ACRE
MEDIUM DENSITY	UP TO 25	DWELLING UNITS PER GROSS ACRE
MEDIUM-HIGH DENSITY	UP TO 60	DWELLING UNITS PER GROSS ACRE
HIGH DENSITY	UP TO 125	DWELLING UNITS PER GROSS ACRE

INDUSTRIAL AND OFFICE
RESTRICTED INDUSTRIAL AND OFFICE
BUSINESS AND OFFICE
OFFICE/RESIDENTIAL
INSTITUTIONAL AND PUBLIC FACILITY
PARKS AND RECREATION
AGRICULTURE
OPEN LAND
ENVIRONMENTAL PROTECTION
ENVIRONMENTALLY PROTECTED PARKS

TRANSPORTATION
TERMINALS
EXPRESSWAYS
MAJOR ROADWAYS (3 OR MORE LANES)
MINOR ROADWAYS (2 LANES)
METRORAIL PHASE 1
FUTURE RAPID TRANSIT

ACTIVITY CENTERS
REGIONAL
METROPOLITAN

URBAN DEVELOPMENT SUBJECT TO WETLAND BASIN STUDY
2000 URBAN DEVELOPMENT BOUNDARY
2010 URBAN EXPANSION AREA BOUNDARY
WATER
CANAL
LEVEE/CANAL

270° through 0°, of the 0.5 km circle in Fig. 2.3), it differs from the suburbs to the south and east, by having fewer buildings and more trees. The tower is only 50 to 100 m (depending on

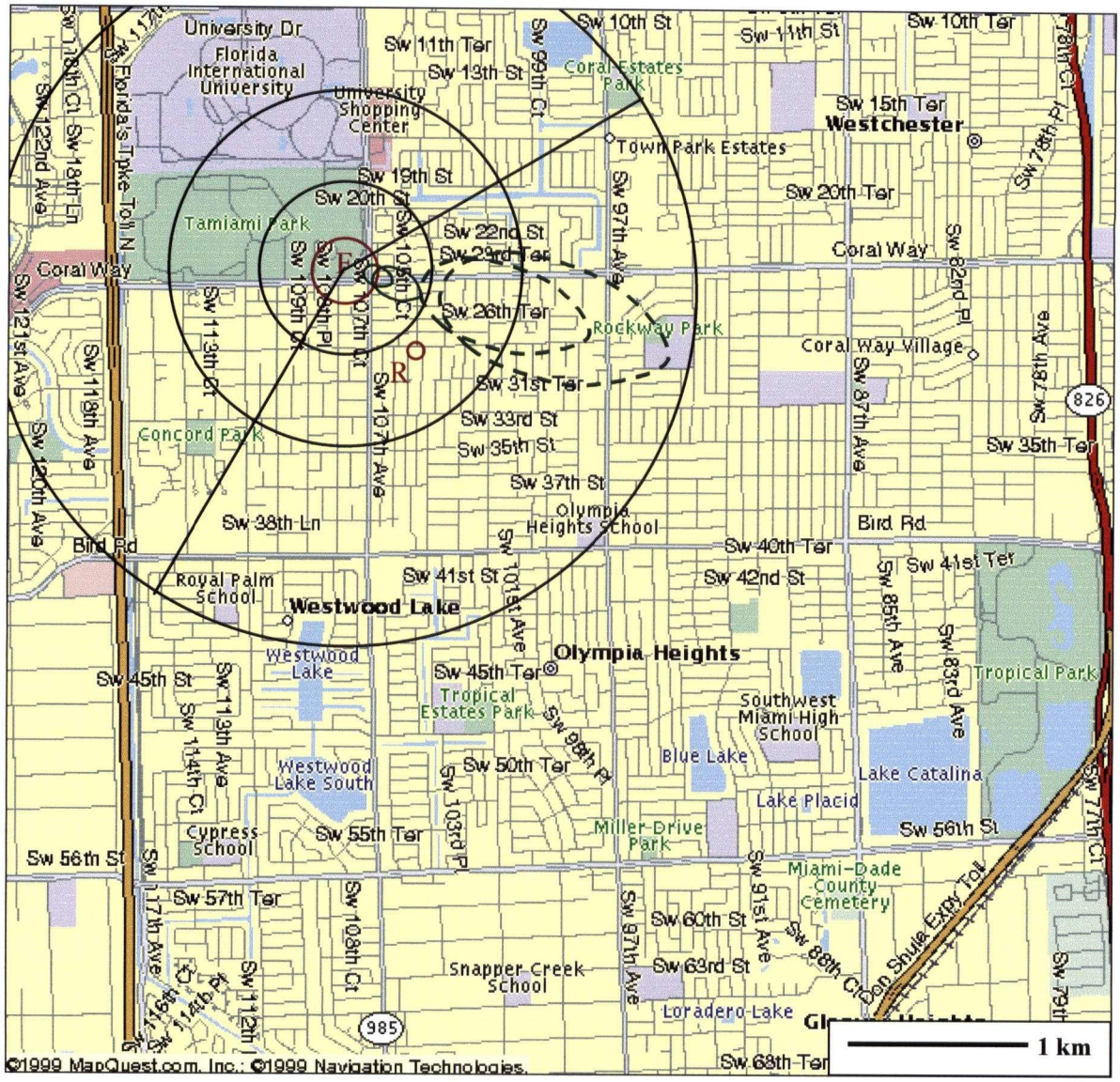

Fig. 2.3 The fairground (F) and residential (R) sites. The top of the page is north. The red circle at the Fairground site represents the area responsible for 95% of the upwelling radiative fluxes observed at the top of the 40 m tower there. The red circle at the Residential site is the same, but because that tower is 10 m high, the source area is smaller. Circles around the Fairground site have radii of 0.5, 1, and 2 km. The two straight black lines mark the range of preferred wind directions, i.e. 60° to 210°. The egg-shaped isopleths represent typical areas responsible for 50% of the turbulent heat fluxes observed at the top of the fairground tower, in both stable (dashed green line) and unstable (solid green line) conditions. The directions of the ellipses represent the most frequently observed wind directions under stable (106°) and unstable (112°) conditions. See Section 2.6 for further explanation.

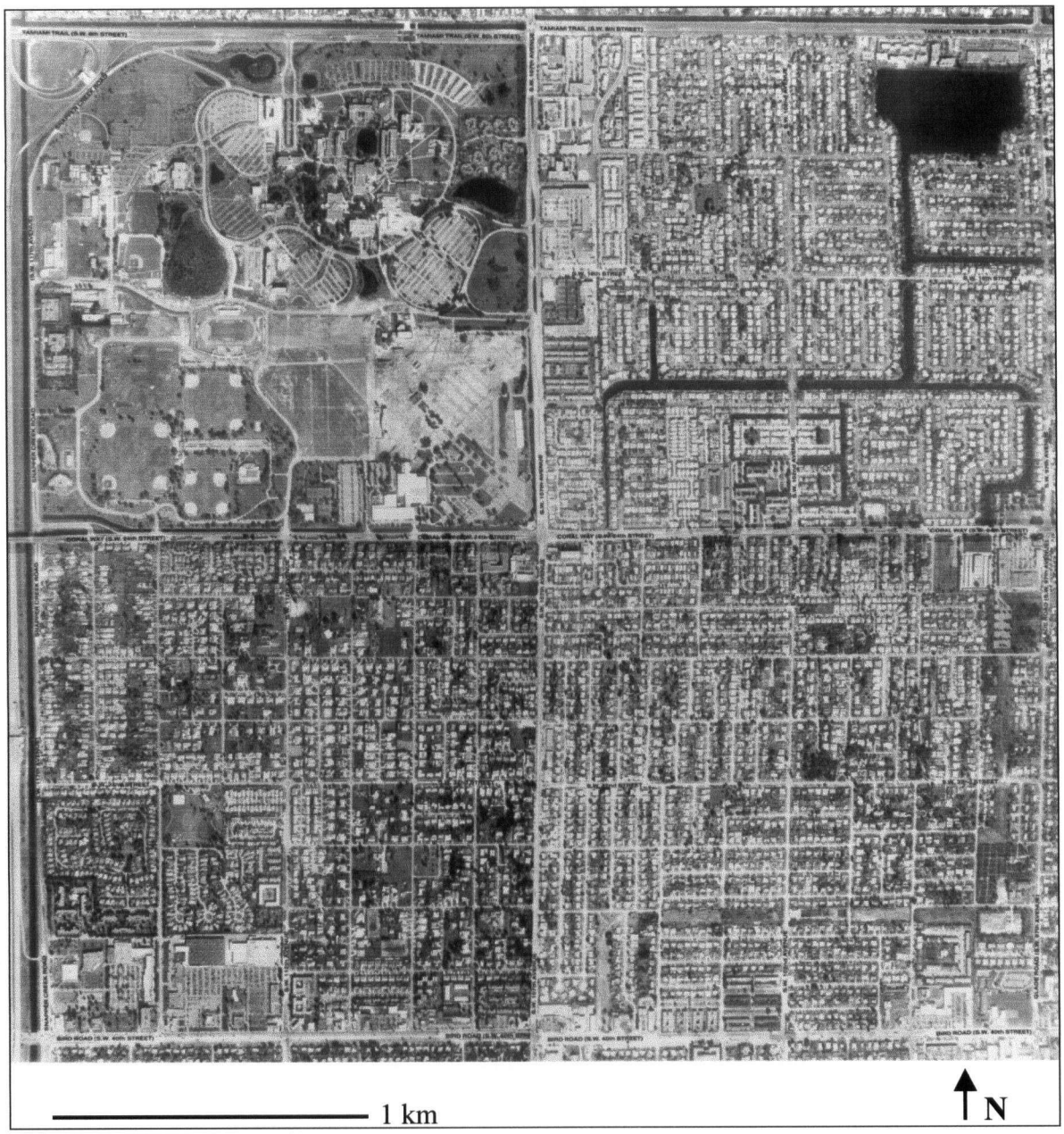

Fig. 2.4 A December 1995 aerial photograph of the study area. At the center is the intersection of SW 107th Ave. and Coral Way (SW 24th St.); directly adjacent to this intersection, to the northwest of it, is the Fairground site. The Residential site is 700 m south-southeast of the Fairground site.

wind direction) downstream from an extensive residential zone to be characterized. Since the sensors are at a height of 40 m, the source areas for the turbulent fluxes are in the residential, not the fairground, area (see Section 2.6.2).

15° segment ending at (0° = North, 180° = South)	**Buildings**	**Impervious**	**Unmanaged**	**Trees**	**Grass**	**Water**
15	0.35	0.27	0.02	0.06	0.26	0.05
30	0.36	0.29	0.01	0.06	0.25	0.05
45	0.34	0.32	0.01	0.05	0.24	0.04
60	0.37	0.28	0.00	0.06	0.26	0.03
75	**0.39**	**0.26**	**0.00**	**0.06**	**0.26**	**0.03**
90	**0.37**	**0.25**	**0.00**	**0.06**	**0.27**	**0.05**
105	**0.36**	**0.23**	**0.01**	**0.07**	**0.30**	**0.04**
120	**0.34**	**0.22**	**0.02**	**0.07**	**0.31**	**0.02**
135	**0.34**	**0.22**	**0.03**	**0.08**	**0.32**	**0.02**
150	**0.33**	**0.20**	**0.04**	**0.08**	**0.34**	**0.02**
165	**0.33**	**0.17**	**0.04**	**0.08**	**0.35**	**0.02**
180	**0.32**	**0.17**	**0.04**	**0.09**	**0.36**	**0.02**
195	**0.29**	**0.23**	**0.03**	**0.09**	**0.35**	**0.01**
210	**0.24**	**0.33**	**0.03**	**0.08**	**0.30**	**0.02**
225	0.22	0.35	0.04	0.07	0.28	0.04
240	0.18	0.31	0.08	0.06	0.30	0.07
255	0.16	0.30	0.10	0.05	0.31	0.09
270	0.15	0.33	0.09	0.05	0.29	0.09
285	0.16	0.38	0.07	0.06	0.27	0.07
300	0.17	0.41	0.05	0.06	0.25	0.06
315	0.20	0.42	0.04	0.06	0.24	0.05
330	0.26	0.39	0.02	0.06	0.23	0.04
345	0.29	0.33	0.02	0.06	0.24	0.07
360	0.32	0.28	0.02	0.06	0.26	0.07

Table 2.1. Observed plan area fractions of various surface types within a circle of radius 1 km around the tower at the Fairground site. Values in **boldface** correspond to the preferred wind direction; see Section 2.6.2 for explanation.

2.3 Observation Strategy

The studies in Vancouver, St. Louis, Sacramento, Chicago, Tucson, Los Angeles, and Mexico City mentioned in chapter 1 used eddy correlation to measure sensible and latent turbulent heat flux densities directly. The present research employs this approach in

Miami. This and several other aspects regarding instrument choice, and positioning, parallel those in previous campaigns, so as to facilitate their comparison with the other datasets.

In Miami, data were collected in a suburban residential area for a number of reasons other than the aim of maintaining consistency with earlier studies. Suburban surfaces produce less dramatic urban climate effects than downtown areas, but they represent a larger land fraction, and one in which a majority of city-dwellers spend most of their lives. Another reason for selecting a site in the suburbs is that, unlike commercial and downtown areas, they commonly cover sufficiently large land areas to provide adequate fetch for observations conducted on towers tens of metres high.

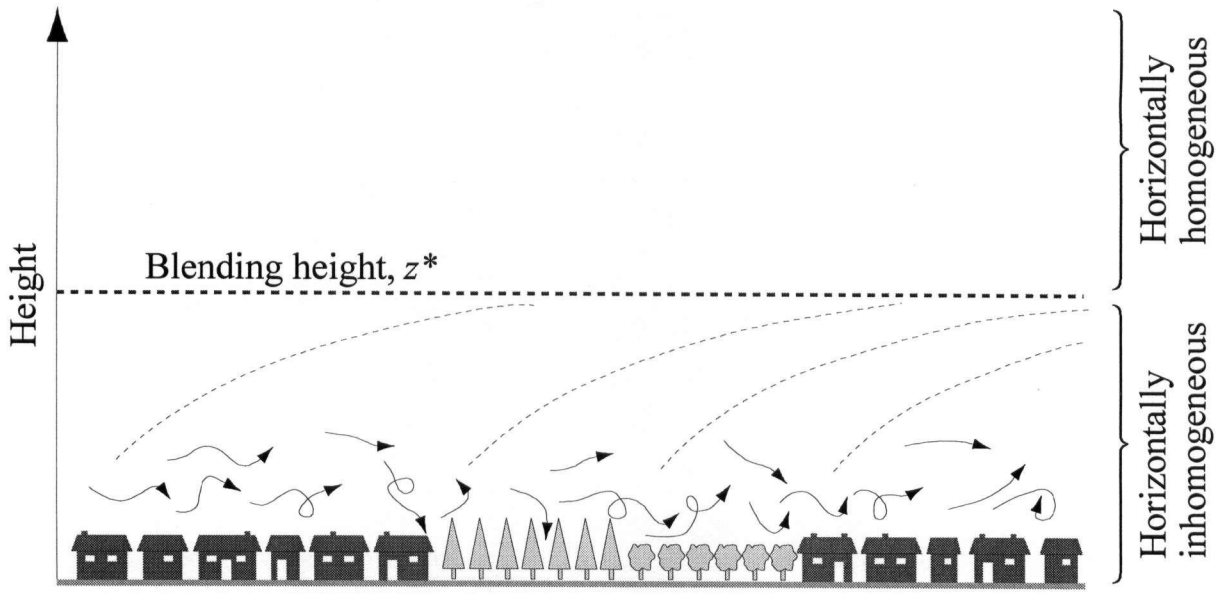

Fig. 2.5 Above the blending height (z^*), Q_H and Q_E are horizontally homogeneous. Below z^*, in the roughness sublayer, Q_H and Q_E are affected by individual roughness elements, and spatial heterogeneity is the norm. *Source:* After Oke *et al.* (1989) and Steyn *et al.* (1997).

Such tower heights are necessary to get above the urban roughness sublayer, into the constant flux layer, so that data are not merely a site-specific, complex function of turbulent

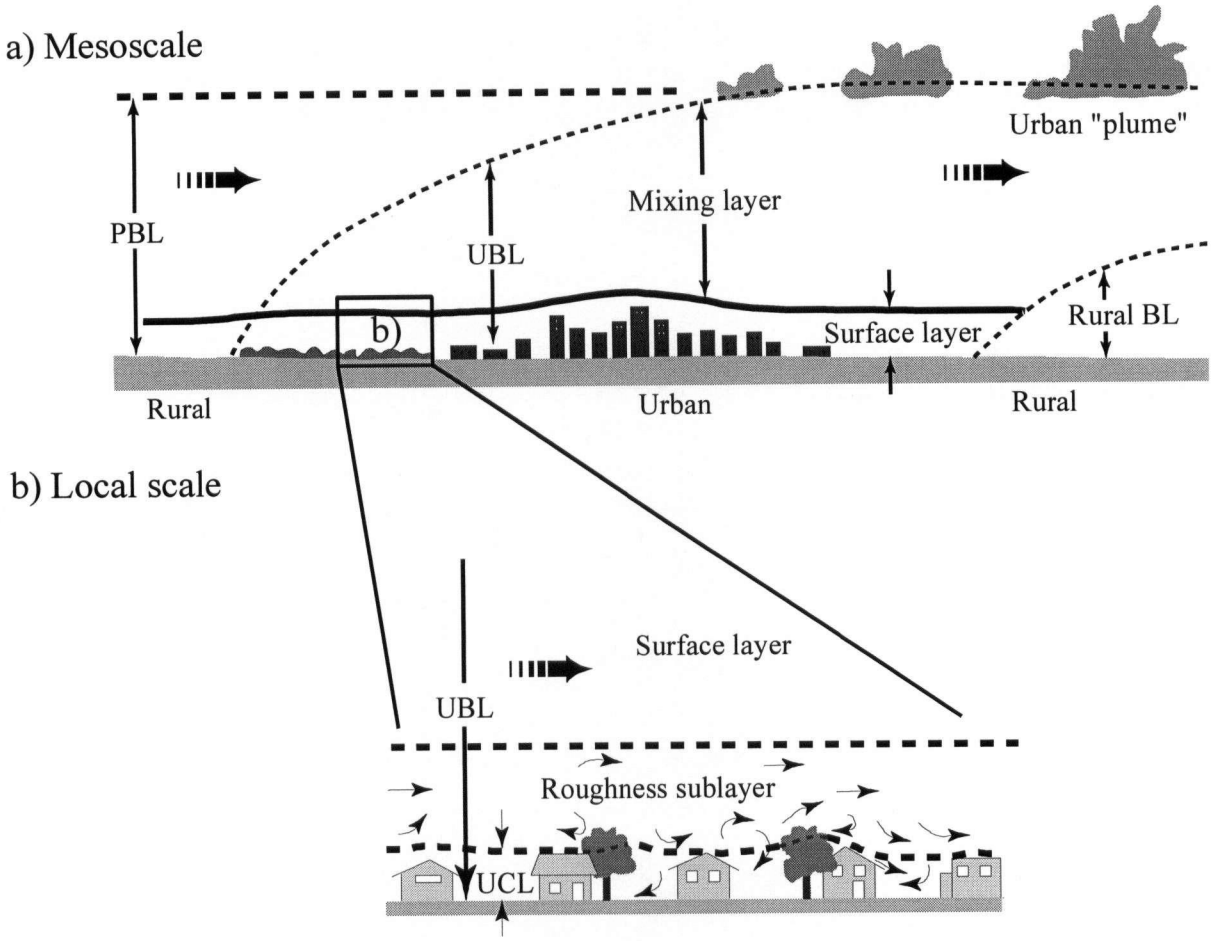

Fig. 2.6 Idealized vertical structure of the urban atmosphere over (a) an urban region at the scale of the whole city, and (b) a land-use zone.
Source: Modified after Oke (1997).

flow around individual roughness elements (Figs 2.5, 2.6). Turbulent flux density measurements taken within the urban roughness sublayer would not be ideal in an energy balance study because in that layer air movement, and thus turbulent heat transfer, is dynamically influenced by individual buildings and trees, so an apparent transfer of heat between the surface and the atmosphere could actually be the circulation of heat within a near-surface eddy. To eliminate this ambiguity data are collected higher, in the constant flux

layer, through which heat, mass, and momentum are transferred between the roughness sublayer and the mixed layer.

The depth of the roughness sublayer (or blending height, z^*) is approximately $2D$ to $3D$, where D is the horizontal spacing of the roughness elements, but several relations have been suggested (Grimmond 1988, Grimmond and Oke 1999b). Houses and trees are the dominant roughness elements in suburban west Miami, and approximately 95% of the houses in the study area are single-story, single-family homes with rooftops about 5 m high. Trees in the area are occasionally as high as 12 m, but such large trees are far less numerous than houses. D for the study area was observed, by means of surveys conducted on foot, to be on the order of 17 m (Table 2.2). Using four different formulae for z^*, this produces a roughness sublayer which is typically between 20 and 40 m in depth (Table 2.2). This suggests that the turbulence sensors were in the constant flux layer.

15° segment ending at	D (N – S)	D (E – W)	z^* Pasquill '74	z^* Mulhearn and Finnigan '78	z^* Garratt '78	z^* Raupach '80
75°	11.7	8.6	14.1	23.3	25.4	21.0
90°	11.4	7.4	13.7	24.5	24.7	23.2
105°	14.2	9.1	13.5	29.2	24.3	19.8
120°	19.4	11.0	14.2	36.4	25.6	18.2
135°	12.0	22.3	14.8	41.1	26.6	17.9
150°	12.4	23.4	15.0	42.3	27.1	15.9
165°	12.7	24.1	15.1	43.5	27.2	14.0
180°	13.0	24.2	15.4	43.1	27.7	14.1
195°	13.7	24.1	15.9	40.6	28.7	21.0
210°	20.8	35.2	19.4	53.3	34.9	40.7
average	**14.1**	**18.9**	**15.1**	**37.7**	**27.2**	**20.6**
median	**12.8**	**22.8**	**14.9**	**40.8**	**26.8**	**19.0**

Table 2.2. Roughness element spacing (D) from field surveys and calculated blending heights (z^*) for sectors of a circle of radius 1 km, centred on the tower at the Fairground site. Units for the first column are degrees of the compass, and are metres for the others.

Turbulent eddies originating from a large area (i.e. tens of thousands of m^2; see Table 2.6 for more information) upwind of the tower are able to impinge on instruments at a height of 40 m. Therefore, since prevailing winds in Miami are from the southeast, it was necessary to ensure that large areas to the east, southeast, and south of the tower were suburban and continuous. The Fairground site in west Miami was 13 km northwest of the Atlantic Ocean, with 10 km of fetch over suburbs extending windward, uninterrupted except by canals and a few parks and small lakes (Fig. 2.2). These 'interruptions' are not necessarily undesirable elements in the study area; like parking lots, houses, and lawns, they have distinct boundaries and physical properties, but they, like the other suburban features, are a normal part of the area under scrutiny, thus their effects on local climate must be taken into account. By measuring turbulent flux densities in the constant flux layer, and by selecting a site with extensive suburban fetch, data are self-integrated over a variety of suburban surfaces.

2.4 Instrumentation

The components of the surface radiation balance (1.1) were measured individually. The outgoing radiative flux densities, $K\uparrow$ and $L\uparrow$, were measured at a height of 10 m at the Residential site. The net all–wave radiation, Q^* was also measured at 10 m at the Residential site, and at 40.64 m at the Fairground site. The incoming radiative fluxes, $K\downarrow$ and $L\downarrow$, were measured at the Fairground site, at a height of 2.5 m. The turbulent fluxes, Q_H and Q_E, were measured at 40.84 m at the Fairground site, and various ground–based instruments were present at both sites.

2.4.1 Residential Site Instruments

A net radiometer and two down-facing radiometers (a pyranometer and a pyrgeometer)

were mounted at the top of the 10 m tower at the Residential site. At the base of the tower, in addition to a rainproof datalogger box, were a lysimeter and four surface wetness sensors (Table 2.3).

Instrument	Variable Measured	Measurement Height (m)
REBS Q6 net radiometer	Q^*	10
Eppley pyranometer	$K\uparrow$	10
Eppley pyrgeometer	$L\uparrow$	10
lysimeter	dewfall/evaporation (g)	0
surface wetness sensors (4)	surface wetness (from 0 = dry to 1 = wet)	0

Table 2.3 Tower and ground based instruments at the Residential site.

$K\uparrow$ and $L\uparrow$ were measured at the Residential site because they are affected by the surface over which they are measured. Measuring them at the Fairground site, while more convenient logistically, would be less useful because the surface at that location is not as representative of suburban Miami.

2.4.2 Fairground Site Instruments

Turbulence sensors, as well as several other instruments, were mounted on a 40 m pneumatic tower at the Fairground site (Table 2.4, Fig. 2.7).

Instrument	Variable(s) Measured	Measurement Height (m)
Gill 3-D sonic anemometer	u', v', w', T' [1]	40.84
CSI[2] 1-D sonic anemometer and fine-wire thermocouple system (CA27)	w', T'	40.84
CSI krypton hygrometer (KH20)[3]	q'	40.84
REBS Q6 net radiometer	Q^*	40.64[4]
Li-Cor mini-pyranometer	$K\downarrow$	40.64[4]
Vaisala HMP C	T, RH	40.74
R. M. Young Wind Sentry	u, wind direction (*dir*)	41

Table 2.4. Tower mounted instruments at the Fairground site.

[1] The Gill anemometer measures temperature by the speed of sound, not by thermocouple.

[2] Campbell Scientific Incorporated

[3] The signal from the krypton hygrometer was split by splicing an extra lead onto each of the two signal output wires, so that both the 3-D and 1-D sonic anemometers could be logged with synchronized q' data.

[4] The net radiometer and miniature pyranometer were positioned slightly lower than the other instruments, and were mounted on a 1 m horizontal arm (Fig. 2.7) to increase the distance between them and the main instrument array. This decreased the magnitude of inter-instrument radiative exchanges and turbulent wake effects.

At the base of the tower was a camper that housed datalogging equipment and an atmospheric air pressure sensor. On top of the camper were radiometers to measure the incoming long- and shortwave radiative flux densities. At ground level, next to the camper and tower, were a raingauge, lysimeter, and two surface wetness sensors (Table 2.5).

Instrument	Variable(s) Measured	Measurement Height (m)
air pressure sensor	atmospheric pressure	2
Eppley pyranometer	$K\downarrow$	2.5
Eppley pyrgeometer	$L\downarrow$	2.5
tipping bucket raingauge	precipitation (mm)	0
lysimeter	evaporation/dewfall (g)	0
surface wetness sensors (2)	surface wetness (from 0 = dry to 1 = wet)	0

Table 2.5 Ground based instruments at the Fairground site.

$K\downarrow$ and $L\downarrow$ can be measured at the Fairground site for convenience because these fluxes have low spatial variability and are not affected by the surface over which they are measured.

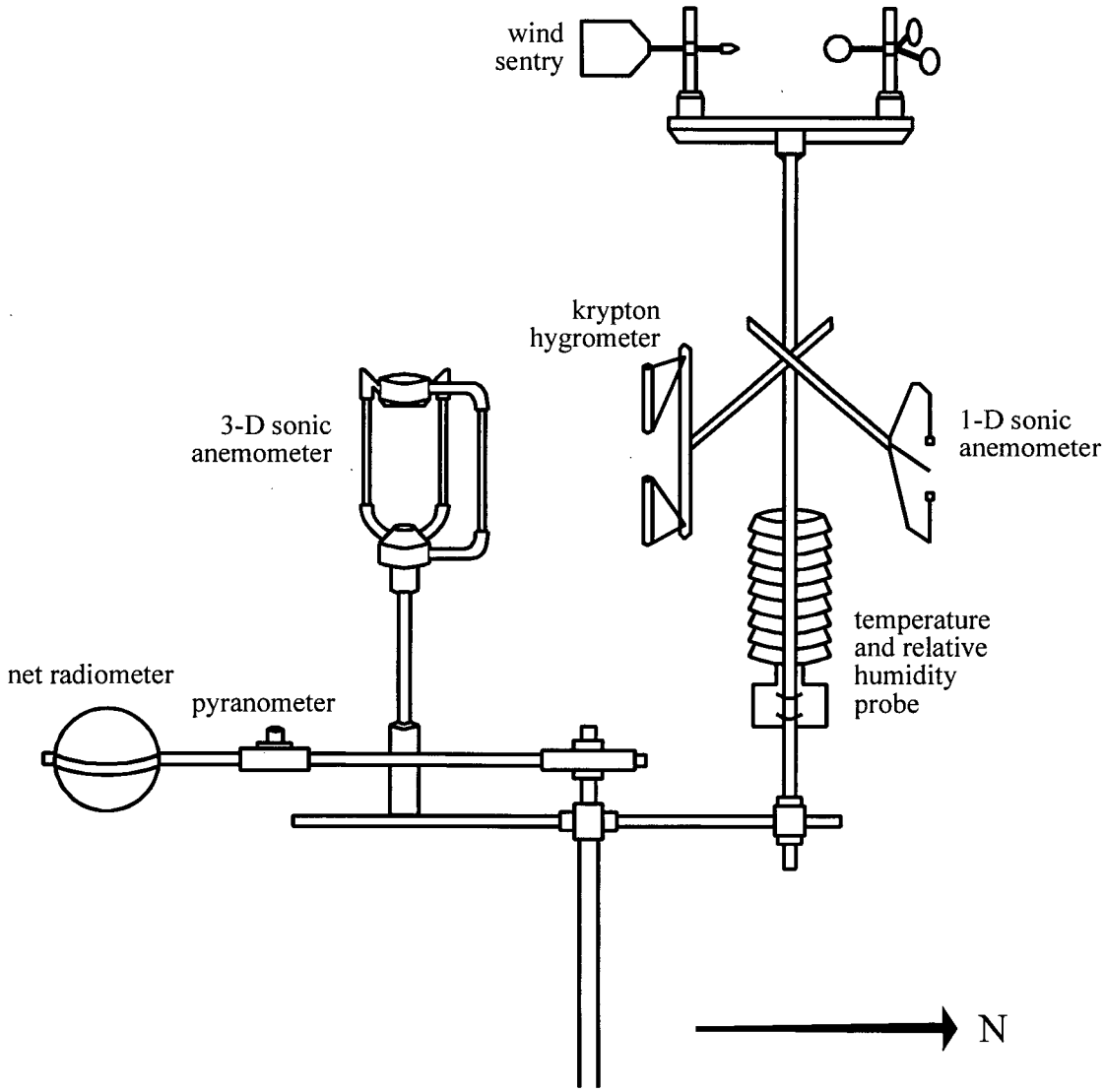

Fig. 2.7 The tower-mounted instrument array at the Fairground site. The turbulence sensors were aimed towards the southeast, the prevailing wind direction. The hygrometer was placed between the two sonic anemometers, 0.1 m from each. The radiometers were pointed south from the tower and main instrument array, so that the array could not shade them.

2.5 Data Management

2.5.1 Data Logging

At the Residential site, data were logged by two CSI 21X dataloggers and downloaded daily to a laptop computer.

At the Fairground site, data were logged by three CSI dataloggers and a laptop PC. The only instrument not logged by a CSI datalogger was the 3-D sonic anemometer, which was logged by a laptop. w', T', and q' were sampled by a CSI datalogger at 5 Hz, and the CSI 21X software used in previous studies was used in Miami to calculate and log Q_H and Q_E as 15-min averages. The 3-D sonic anemometer data were sampled at 20.83 Hz, logged raw in 30 min runs to the hard drive of the laptop, and archived daily to 120 Mb computer backup tapes. Data were downloaded daily from the CSI loggers to a laptop for storage and visual checks, then archived to 1.44 Mb floppy disks.

The signal output wires of the hygrometer and the 1-D sonic anemometer were each split so that their data could be logged by a CSI datalogger (at 5 Hz) as well as by the analog input channels of the 3-D sonic anemometer (at 10 Hz). This was done because the CSI 21X software could provide Q_H and Q_E flux values every 15 min, and the 3-D sonic anemometer's software could log 3-D, 1-D, and hygrometer data simultaneously. The latter facilitates comparisons between w' and T' from the two anemometers.

Output from the hygrometer has a range of 0 to 5 volts, which corresponds to the analog input range of the 3-D sonic anemometer, so the hygrometer was wired directly to that anemometer. Output from the 1-D sonic anemometer is –5 to 5 V, so its signal was decreased, using resistors, to a range of –2.5 to 2.5 V, then boosted, using two resistor-equipped 12 V cells (one each for w' and T'), to 0 to 5 V.

Because the hygrometer and the 1-D sonic anemometer were logged by both the CSI datalogger and the 3-D sonic anemometer, two calculations each of Q_H and Q_E, from the same

instruments, are possible. A third calculation of Q_H and Q_E is possible, using data from the 3-D sonic anemometer itself, with q' from the hygrometer.

2.5.2 Data Processing

Q_H and Q_E flux measurements from the 1-D sonic anemometer and krypton hygrometer, logged by the CSI datalogger, are used in subsequent chapters in order to facilitate comparison with observations from other suburban studies. Corrections were made to those two flux measurements, for oxygen absorption by the sensor (Tanner and Greene 1989) and air density (Webb *et al.* 1980). No corrections were made for frequency response or spatial separation of the eddy correlation sensors. Neglect of these corrections probably underestimates Q_E by 1% at suburban sites (Grimmond and Oke 1995).

All data recorded by the 3-D sonic anemometer were transferred from a series of 120 Mb tapes to two CD-ROMs to accelerate their processing. Standard procedures were performed on the data; a linear trend was removed from them, and the x, y, z wind coordinates were rotated into natural coordinates (u, v, w) through alignment of u with the mean wind (i.e. mean $v = 0$). No filtering was done. Special software was used to compute Q_H and Q_E (individually for the 3-D anemometer/hygrometer and 1-D anemometer/hygrometer combinations), and turbulence statistics such as the stability, normalized standard deviations, correlation coefficients, and (co)spectra. Further outputs included averaged (over 1 sec) time series of all variables and fluxes. For each 30 min run, the software was initialized with the following variables from the slow response data logged on the 21X: atmospheric pressure, air temperature, relative humidity, wind speed, wind direction, net radiation, and the voltages (recorded manually each day) of the 12 V signal-boosting cells.

All energy flux and slow response data were imported into a Quattro Pro spreadsheet on a PC, and converted from 15 and 30 min averages to hourly averages. All times are corrected to local mean solar time, or local apparent time (LAT).

2.6 Flux Source Areas

It is important to know the surface area 'seen' by the radiation and turbulence sensors, and especially to know if they are congruent so that the energy balance is 'closed' to the best degree possible.

2.6.1 Upwelling Radiative Fluxes

The circular source areas for the upwelling radiative fluxes ($K\uparrow$ and $L\uparrow$) depicted in Fig. 2.3 are calculated using

$$r = z_s\,(1/F - 1)^{-0.5}, \tag{2.1}$$

where r is the radius of the source area circle, z_s is the sensor height, and F is the portion of the flux for which that area is responsible, i.e. 0.95 (Schmid *et al.* 1991). The radiant source area for the 40 m high Fairground tower has a 178 m radius, giving an area of 9.96×10^4 m^2. For the 10 m Residential tower, the radius is 43.6 m, giving an area of 6.0×10^3 m^2.

2.6.2 Turbulent Fluxes

Turbulent flux observations for hours during which the mean wind direction is from the north, northwest, or west (i.e. between 270° and 360°) are discarded because the surface cover in those areas is not representative of suburban regions. Furthermore, eddies arriving at the sensors from those directions are disturbed by the instrument mounting apparatus. Wake effects also are a concern when the wind is from the northeast (45°) or southwest (225°), because the three turbulence sensors are placed along a line running in that direction. The array is an optimal

configuration for the prevailing winds, which are from the southeast (135°). Thus the accepted range of wind directions is from 60° to 210°.

A model to calculate turbulent source areas ('footprints') has been devised by Schmid (1994). The most recent version of the model is FSAM3.EXE, version 3.1, June 10, 1998. It calculates the position and dimensions of turbulent flux source area isopleths (i.e. ellipsoids), given the effective measurement height z' (= sensor height z_s – zero-plane displacement z_d) roughness length z_o, Obukhov length L, the standard deviation of lateral wind speed fluctuations σ_v, and the friction velocity u_*. For a given set of input values, the software provides the dimensions, and horizontal distances to the measurement location, of 10 isopleths of the source area, in increments of 10%. Fig. 2.3 shows four 50% source area isopleths for the current study. These dimensions can also be provided by a parameterization called mini-FSAM (Schmid 1994), but for the same input data, mini-FSAM and FSAM3 do not provide the same output values. The more recent model is considered preferable (M. Roth, J. Voogt, *pers. comm.* 1999) and is the one used here.

Under stable atmospheric conditions ($0 < L$), 15 research grade calculations of source area isopleths were made, and 69 were made under unstable conditions ($0 > L$), from hourly averages of the input data. Several requisites must be met to successfully obtain meaningful calculations for a given hour of the study period. Q_H and Q_E measurements must both be available, which is the case for 327 hours, and the wind direction must be between 60° and 210°, which is the case for 232 of those hours. 3-D sonic anemometer data must also be available, so that FSAM3 inputs L, σ_v, and u_* can be calculated. This is possible for 151 of the 232 hours of usable turbulent flux measurements. Finally, the program must run

to completion—it has a tendency to crash (i.e. freeze, failing to provide output), but it does so consistently; re-entering input values that caused it to crash once will cause it to do so again. 46 hours of data were available under stable conditions, and 31 of these caused FSAM3 to crash. The unstable data fared better, with 105 hours of data producing 36 crashes.

Thus dimensions for 15 stable and 69 unstable turbulent flux 50% source area isopleths were computed. One of the two stable isopleths depicted in Fig. 2.3 is the median of the stable isopleths, in terms of area. The area of the other is the closest of the 15 to the mean area. The same applies to the two unstable isopleths (Table 2.6).

stability	**YD**	**LAT**	Q_H, Q_E (W m^{-2})	**dir**	**area**	**median**	**mean**
stable	149	0500	-14.3, 12.3	109°	3.45×10^5	3.45×10^5	6.99×10^5
stable	152	2200	-1.5, -5.6	103°	6.73×10^5	3.45×10^5	6.99×10^5
unstable	147	1500	251.1, 166.0	124°	1.47×10^4	1.47×10^4	4.21×10^4
unstable	149	1800	48.0, 18.6	70°	4.25×10^4	1.47×10^4	4.21×10^4

Table 2.6 Areas and turbulent flux values for 50% source area isopleths computed by FSAM3. The **area**, **median**, and **mean** columns are all in units of m^2.

It must be stressed that these 50% source areas are only order-of-magnitude estimates. FSAM3 is based on the solution of the advection-diffusion equation, and assumes that turbulence is generated primarily mechanically, with buoyancy effects playing a minor role. For several of the model runs that did provide output, the program gave a warning message that z'/L "is rather high for surface layer scaling", indicating that buoyancy may be more important in these cases than the model assumes. Thus the source areas illustrated in Fig. 2.3 are rough estimates only, and should not be given more significance than that

implies, because in those 'high z'/L situations', the model results should be taken with a grain of salt (H-P. Schmid, *pers. comm.* 1999).

2.7 Operational Routine

2.7.1 Site Maintenance

The daily downloading of data at both locations was accompanied by an inspection of the site, which included checking the raingauge for obstructions, checking radiometer domes for contamination externally or condensation internally, inspecting surface wetness sensors for damage, and ensuring visually that the soil and grass monoliths in the lysimeters were still reasonably healthy.

The most labour intensive site management task was to monitor and maintain the turbulence sensors because two of them, the hygrometer and the 1-D sonic, can be damaged by rainfall. Miami is a difficult place to operate these systems because the strong surface heating typically encountered in the tropics drives vigorous convection, which often results in afternoon thundershowers. The 40 m tower on which these instruments were mounted is pneumatic, so it could be collapsed and the delicate instruments covered with plastic bags during rainy periods. Collapsing and re-erecting the tower takes about 90 min in total. During the 41 day observation period this procedure had to be performed 19 times, only one of which (broken thermocouple) was not due to rain or the threat of it.

2.7.2 Manual Data Collection

Part of the daily routine was collecting a pair of soil samples from each site, to measure soil moisture. Samples were weighed, baked for 24 hours to drive off moisture, and weighed again to measure the mass of water driven from the soil.

Site surveys were conducted on every block within 500 m of the Fairground site, and on representative blocks to a distance of 1 km from the site. This involved photographing typical houses and completing questionnaire-format survey forms, providing such details as the number of trees and shrubs on each property and the height in stories of each building. This information was entered into a geographic information system (GIS), where it was used to calculate surface characteristics such as the mixing height, z^* (Table 2.2).

On June 14, 1995, through midnight to the early hours of the 15th, leaf stomatal resistances were sampled at the Residential and Fairground sites, using a portable automatic porometer model Mk3 from Delta-T Devices.

2.8 Weather Conditions during the Observation Period

The observation period was from May 13 (YD 133) to June 21 (YD 172), 1995. During this period the average air temperature was 27.2 °C; that is 0.9 °C warmer than normal. 19 of the 41 observed days had rain amounts greater than 0.25 mm; that is 3 days more than normal. General weather conditions were dominated by diurnal convection cycles; mornings tended to be clear, with thunderstorms developing in the afternoons. Winds were predominantly from the southeast (Fig. 2.8).

The decrease in temperature and vapour pressure deficit in the early afternoon (Fig. 2.8) is due to the patchy thundershowers that typically occurred at that time. Generally the weather was sunny, but numerous small cumulus clouds were usually present.

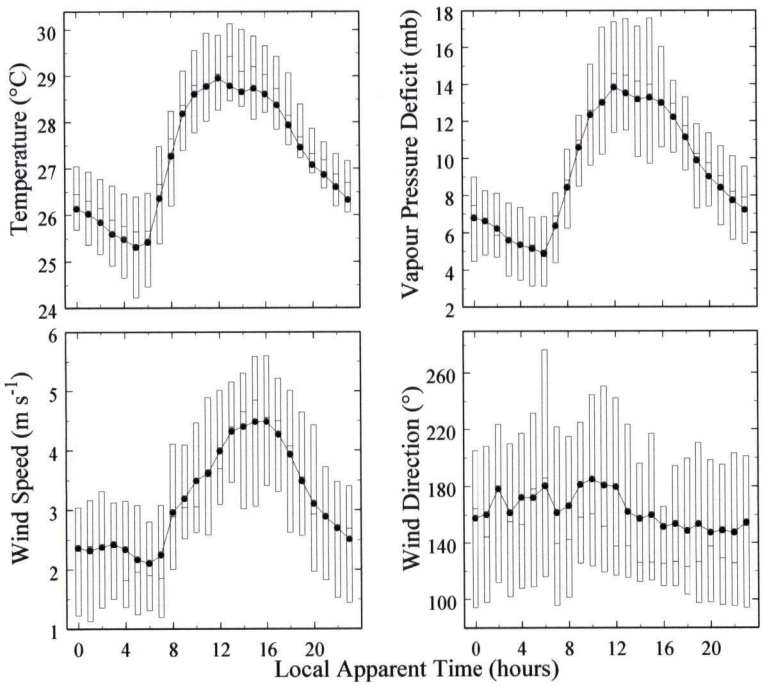

Fig. 2.8 Ensemble hourly averages of air temperature, vapour pressure deficit, wind speed, and wind direction at the top of the 40 m tower at the Fairground site over the entire observation period. Data are from the temperature and humidity probe, and the wind sentry. In boxplots the top of each box corresponds to the 75th percentile of that hour's data; the horizontal line within is the median, and the bottom is the 25th percentile.

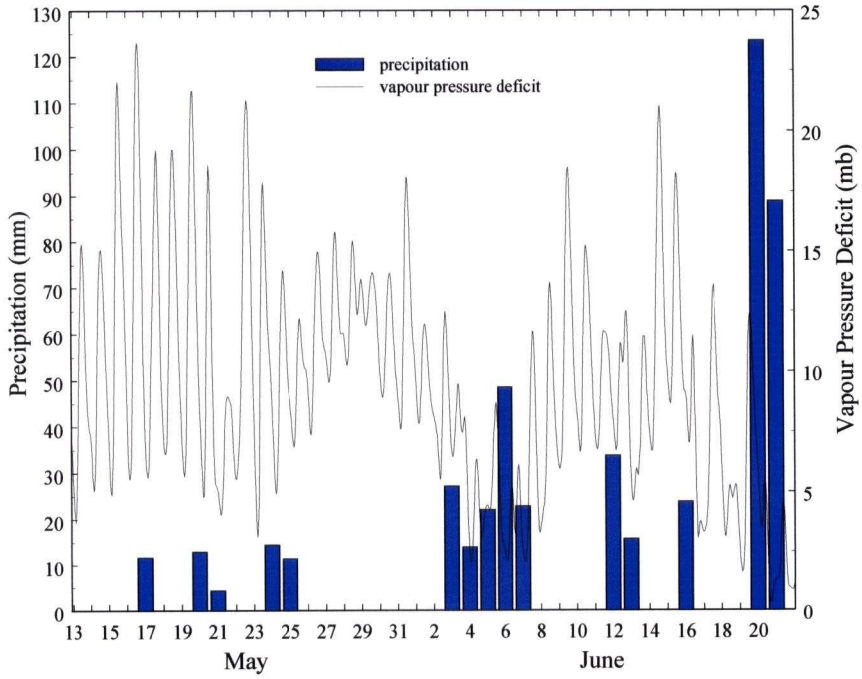

Fig. 2.9 Time series of daily precipitation totals and hourly averaged vapour pressure deficit at the Fairground site. Data are from the tipping bucket raingauge (on the ground) and the temperature and humidity probe (at a height of 40 m). Precipitation totals less than 1 mm are not included.

Virtually all of the precipitation observed during the study period (Fig. 2.9) can be attributed to synoptic weather systems. On May 17th, a weak, short-lived trough was present, and on the 20th and 21st a cold front passed over the length of Florida, from north to south. On May 24-5, a weak low pressure centre was in the vicinity of south Florida, but it is possible that that precipitation was due to mesoscale activity. From June 3rd to 7th, a low was in the area. It developed into Hurricane Allison in the early hours of the 5th, was downgraded to a tropical storm near the end of that day, and to a tropical depression early on the 6th, and by midday on the 6th, it was a low, with several troughs extending from it and providing precipitation to Miami on the 7th. On June 12th, a trough passed over south Florida, followed by a cold front on the 13th. June 14th (YD 165) was almost completely cloudless in Miami, as the cold airmass crossed the region. A weak trough was present on June 16th, and on June 20-1 a number of strong troughs and lows provided considerable rainfall, flooding parts of the city with up to 1 m of water.

The near-surface air temperature showed a fairly narrow range of variation during the study, and the diurnal curves grew erratic when there was substantial precipitation (Fig. 2.10). The effect of the June 13-4 cold front can easily be seen in the depressed overnight low, about 2°C cooler than at any time in the previous 30 days. This was accompanied by a 2-day wind speed maximum which occurred at night, whereas usually the maxima are in the early afternoon (Fig. 2.10).

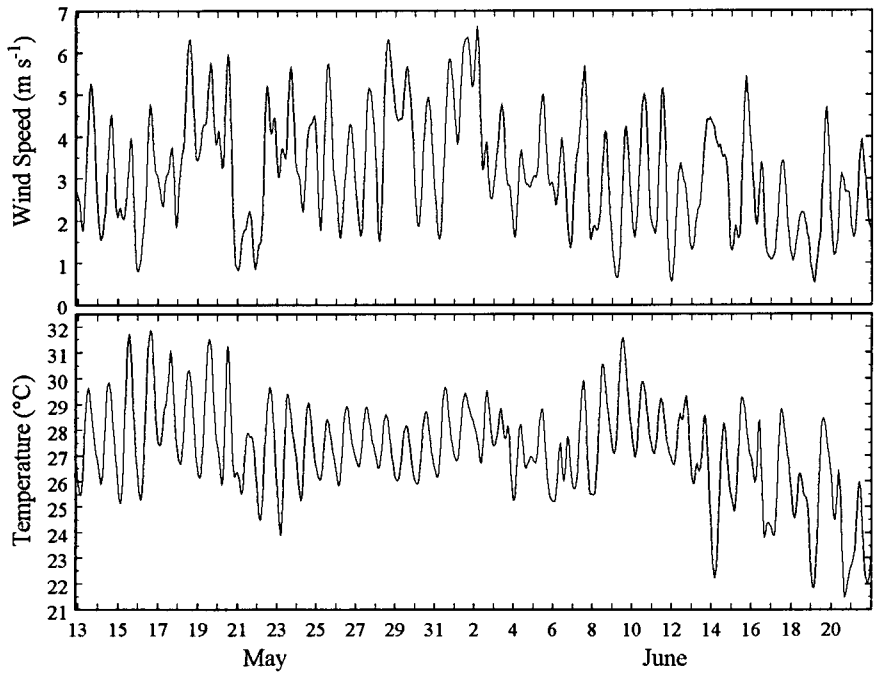

Fig. 2.10 Time series of hourly averaged temperature and wind speed at a height of 40 m at the Fairground site. Data are from the temperature and humidity probe and the wind sentry.

2.9 Comparative Statistics

In order to quantitatively assess errors between various observed and predicted radiation fluxes, two sets of statistical calculations are used. The first uses a widely available Windows 95 computer spreadsheet program, Quattro Pro version 8. It contains a linear regression function that computes the slope and Y-intercept of a line, as well as the standard error of Y estimation (S.E.) and r^2.

The second set, referred to here as Willmott statistics, consists of four quantities calculated using Willmott's (1982) formulae. These statistics are considered ideal when comparing the performance of a model against observed data. The first of these is the mean absolute error (MAE), which is the mean of the absolute values of the differences between a set of observed and predicted values. The second is the mean bias error (MBE), which is the

mean of the differences; the third is the root mean squared error (RMSE), which is the root of the average of the squared differences, and the fourth, d, is a dimensionless number between zero and unity that indicates the degree of predictive accuracy from the independent variable. Good agreement between the observed and predicted variables is indicated by Willmott error terms close to the measurement error, and by d values at or above about 0.80 (Saunders and Bailey 1997).

CHAPTER 3. RADIATION BUDGET

3.1 Observed Radiation Fluxes ($K\downarrow, K\uparrow, L\downarrow, L\uparrow$)

3.1.1 Cloudless Skies

The climatology of the four individual radiation fluxes under clear sky conditions at the Miami site (Fig. 3.1a) is, for the most part, as expected, given that observations were made from May 16 to June 21 at almost 26° N latitude. The two shortwave components describe smooth, unimodal curves, with a peak at solar noon. Actually Fig. 3.1a is somewhat surprising in that it looks like an ideal radiation budget, with even, symmetrical curves, despite the fact that these observations are from a suburban site, where the heterogeneous nature of both the atmosphere and the urban surface might be expected to give more erratic radiative flux behaviour.

Of the 855 hours of radiation observations made during this study, only 9% (77 hours) were with clear sky conditions. Observation hours with any cloud present are classified as 'cloudy'.

The overall appearance of the surface radiation balance in Miami is very similar to others, both rural and urban (e.g. see Oke 1987, Monteith and Unsworth 1990), but there is one difference: the incoming fluxes have relatively high absolute values. Because previous urban studies have been conducted at mid-latitude sites, climate forcing by $K\downarrow$ and $L\downarrow$ has been smaller than in Miami, which is a high energy, near-tropical environment. Clear sky fluxes observed in Vancouver, B.C. in 1978 include peak $K\downarrow$ values of about 850 W m^{-2}, while the same flux

measured in Miami is 950 W m^{-2}. Since $K\uparrow$ is essentially a constant fraction of $K\downarrow$, naturally it is also larger in Miami than in extratropical locations.

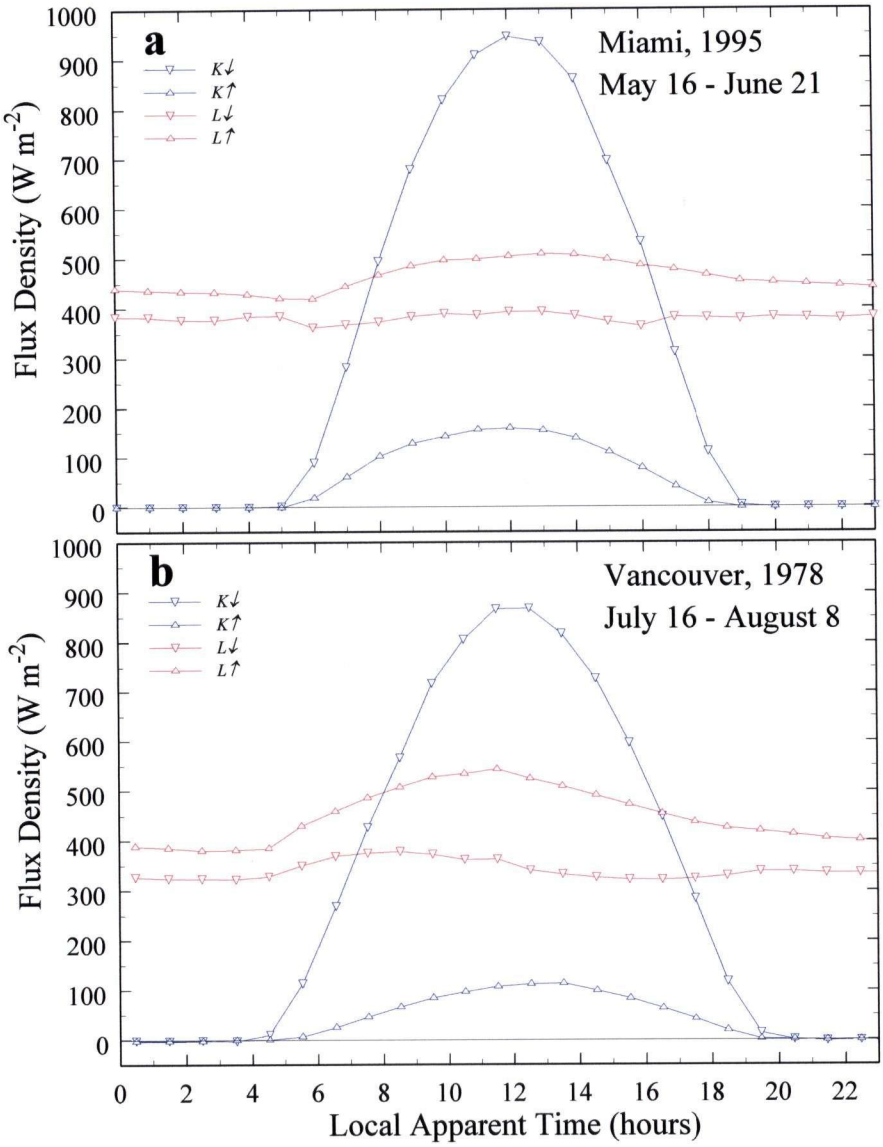

Fig. 3.1 Individual measured radiative flux densities. Ensemble hourly averages over Residential sites during periods with clear skies in a) Miami, this study, and b) Vancouver (T. R. Oke, *pers. comm.* 1999). [The sign convention adopted in all radiation figures is that all individual component fluxes are positive, but net (difference) fluxes have a sign indicating whether they are positive or negative for the surface.]

Clear sky summertime $L\uparrow$ observations in Vancouver (Fig. 3.1b) and Miami are fairly similar, with the former varying from 385 W m^{-2} prior to sunrise, to 540 W m^{-2} at noon, and the

latter increasing from 420 to 510 W m^{-2} at those times. This suggests that the diurnal variation of surface temperature is less in Miami than in Vancouver, probably because of the larger amounts of water at the surface of this subtropical city, both in lakes and canals, and in the soil and vegetation. Water has a high heat capacity, so a wet surface requires larger amounts of energy to alter temperatures. It is also likely to have high evaporation, which cools the surface (but see Ch. 4). Together these controls keep daytime temperatures lower than they would be in a dry region with similar $K\downarrow$ forcing. A corollary is that nighttime temperatures are relatively elevated, due to the slower dissipation of heat from the moist air and soil.

For several of the daylight hours (0600 to 1800 LAT) in the ensemble plot, only one hour of clear sky data was available. Hence it was usually cloudy during the entire 36-day observation period. For example, only one of the 36 hourly observations that were made at 1400 LAT was under clear sky conditions. Thus the fluxes in Fig. 3.1a at 1400 LAT are each single hourly values, not cumulative hourly averages.

Most of the clear sky daylight hours occurred on a single day, June 14, 1995, when a cold front crossed southern Florida. Therefore, because an anomalously cool, dry airmass was present, the $L\downarrow$ values in Fig 3.1a are somewhat lower than usual, and the irregular fluctuations are due in part to the fact that some points are single-hour values. Another effect of the use of single-hour values can be seen in the $K\downarrow$ curve, which shows marginally higher values in the afternoon than in the corresponding morning hours.

Despite the scarcity of clear sky data, these observations do demonstrate that the near-tropics is a high-energy climate region, with radiative fluxes providing large amounts of energy

to be dissipated, both into the ground and buildings, and into the atmosphere. This partitioning is discussed in chapter 4.

There are several other features of Fig. 3.1 worth noting. Firstly, small amounts of sunlight are measured both before sunrise and after sunset; $K\downarrow$ fluxes of less than 5 W m^{-2} are observed at 0500 and 1900 LAT, when the sun is below the horizon according to a simple model used to calculate the local solar elevation angle from the latitude, longitude, time of day, and day of year (Stull 1995). Shortly before sunrise and after sunset, $K\downarrow$ is slightly greater than zero because of scattering and reflection of solar radiation by pollutants and clouds. This twilight period is not unique to Miami.

A second subtle feature of the flux behaviour is that while it exhibits the anticipated diurnal heating and cooling curve, the $L\uparrow$ plot is essentially flat at noon. The Miami data (Fig. 3.1a) show $L\uparrow$ in phase with $K\downarrow$ and flattened at midday. Although the Vancouver $L\uparrow$ plot (Fig. 3.1b) does not exhibit this midday flattening, McCaughey (1985) investigated forested and clearcut rural sites, and observed midday $L\uparrow$ plots that were flattened for the forested site, but curved and unimodal for the clearcut site. (Both plots reached their peak about an hour after that of $K\downarrow$.) This reveals an apparent tendency of surfaces with prominent shading elements, such as trees in a forest, or buildings in a city, to reach their maximum $L\uparrow$ value several hours before solar noon, and maintain it for several hours. This may be due to mitigation of the average radiative surface temperature by cool facets of the surface elements. Some surfaces do not receive direct $K\downarrow$ until the afternoon; others only receive it during the morning, and many vertical surfaces only receive it at a glancing angle in the middle of the day.

Such mitigation also helps to explain the fact that the time lag from the midday peak of $K\downarrow$ to the early afternoon maximum of $L\uparrow$, that is observed to be at least an hour at rural sites (e.g. McCaughey 1985), is in cities an hour at most (e.g. White *et. al.* 1978), and often is non-existent. Strictly speaking, in Miami the delay is about an hour from the $K\downarrow$ peak to that of $L\uparrow$ (Fig. 3.1). However, effectively the two curves are in phase, as they are in the Vancouver data. The flattening of the $L\uparrow$ curve at urban sites seems to make its time lag in relation to $K\downarrow$ less apparent and less significant.

3.1.2 All-sky Conditions

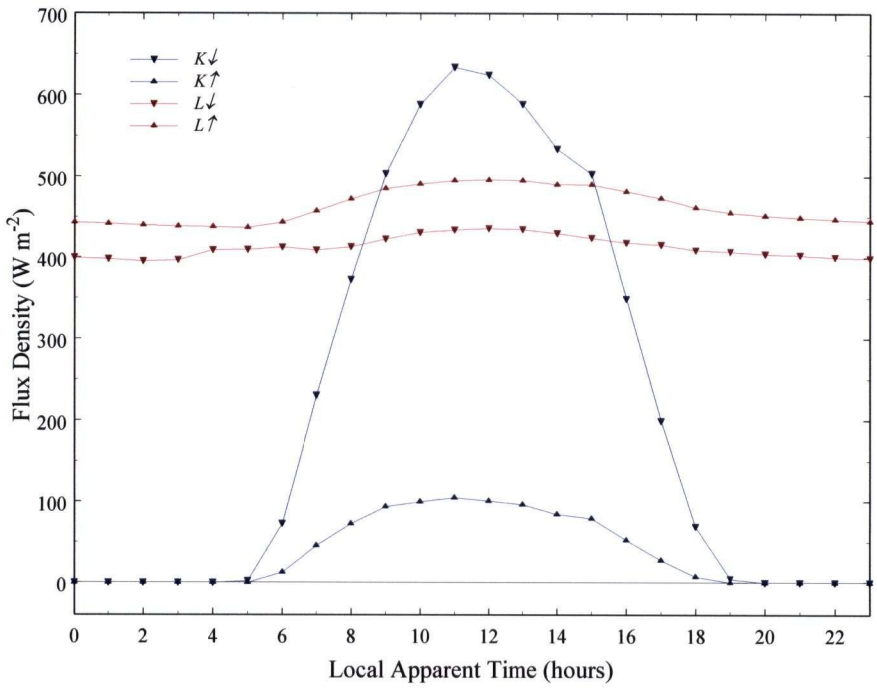

Fig. 3.2 Individual measured radiative flux densities in Miami. Ensemble hourly average observations taken under all-sky conditions.

Daytime heating of the surface, and the destabilization of the urban boundary layer, led to cumulus cloud formation on virtually every day of observations. Thus in the all-sky (cloudless and cloudy) data, the $K\downarrow$ and $K\uparrow$ fluxes show a marked decrease during the late

morning and afternoon hours (Fig. 3.2) compared with the clear sky case. There is also a correspondingly delayed decrease in $L\uparrow$ (Fig 3.2). The $L\downarrow$ curve is smoother than in Fig. 3.1 because each point is an ensemble average of over 30 hours of measurements.

Both the clear and all-sky data show an increase of $L\downarrow$ over an hour before any $K\downarrow$ is detected (i.e. prior to sunrise). This is due to wetting of the $L\downarrow$ sensor by an automated irrigation system at the Fairground site, each day at about 0500 LAT.

3.2 Observed Net Radiation Terms (K^*, L^*, and Q^*)

The individual components can be drawn together in the net terms of the surface radiation balance:

$$Q^* = K^* + L^* \qquad (\mathrm{W\ m^{-2}}), \tag{3.1}$$

where K^* and L^* are the net shortwave and longwave radiative flux densities, respectively. In terms of the instrumentation used in this study, K^* and L^* are defined:

$$K^* = K\downarrow_{fair} - K\uparrow_{residential} \qquad (\mathrm{W\ m^{-2}}) \tag{3.2}$$

$$L^* = L\downarrow_{fair} - L\uparrow_{residential} \qquad (\mathrm{W\ m^{-2}}) \tag{3.3}$$

The four individual flux measurements named above are the only ones available, so they are referred to hereafter without subscripts.

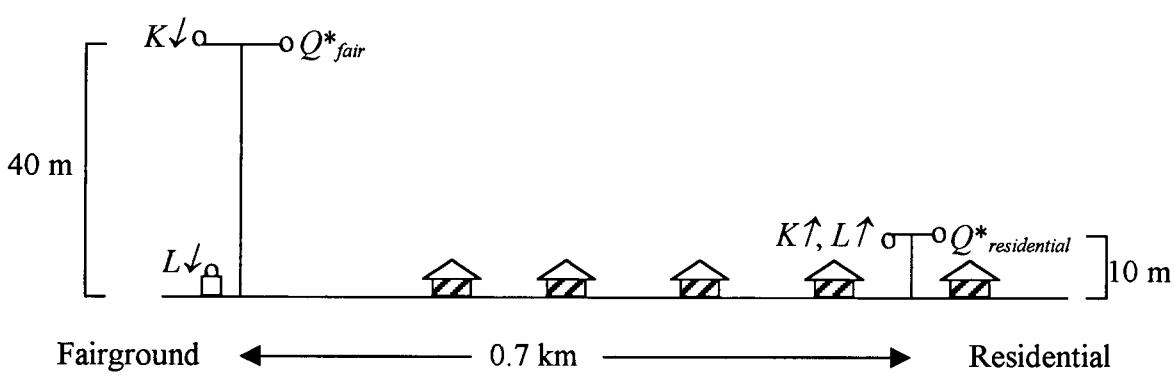

Fig. 3.3 Schematic of the array of radiation sensors in Miami. Q^*_{sum} is the sum of the individual components from the two sites.

On the other hand, three assessments of Q^* are possible, given the instrument array used:

(a) Q^*_{fair} - from the REBS Q6 net radiometer at the top of the 40 m tower at the main Miami site. It is located on a county fairground composed largely of flat grassed and paved surfaces.

(b) $Q^*_{residential}$ - from the REBS Q6 net radiometer at the top of the 10 m tower at the Residential site, which consists of a typical suburban mosaic of single-family homes, trees, grassed yards, and paved streets and sidewalks.

(c) Q^*_{sum} - the arithmetic sum of $K\downarrow$ from the Li-Cor mini-pyranometer on the 40 m tower, $K\uparrow$ from the Eppley pyranometer on the 10 m tower, $L\downarrow$ from the Eppley pyrgeometer on a 2.5 m stand at the Fairground site, and $L\uparrow$ from the Eppley pyrgeometer on the 10 m tower.

Thus Q^* could be said to be over-determined.

3.2.1 Cloudless Skies

The paucity of clear sky observations from this study is responsible for the asymmetry of the K^* curve and the undulations in the daytime portion of the L^* curve seen in Fig. 3.4a, whereas the plots in Fig. 3.4b are much smoother because they are based on 19 days of observations. Overall the net fluxes in Miami and Vancouver are fairly similar, but there are some differences to note. In Miami, K^* has a higher peak (787 vs. 759 W m^{-2}) due to higher $K\downarrow$ at its lower latitude. There are slightly longer days in summertime at Vancouver, as shown by the K^* at 1930 LAT exceeding that of Miami at 1900, and by Vancouver's Q^* turning negative later. Equivalent differences are present during the sunrise period. Vancouver's K^* peak is boosted somewhat, relative to Miami's, by its slightly lower midday surface albedo (α), of ~0.14; clear sky midday α in Miami was ~0.17 (Fig. 3.6). On the other hand, $K\downarrow$ in Vancouver

is decreased because the median day of the study was 35.5 days after the summer solstice (June 22), whereas in Miami it was 19 days before the solstice.

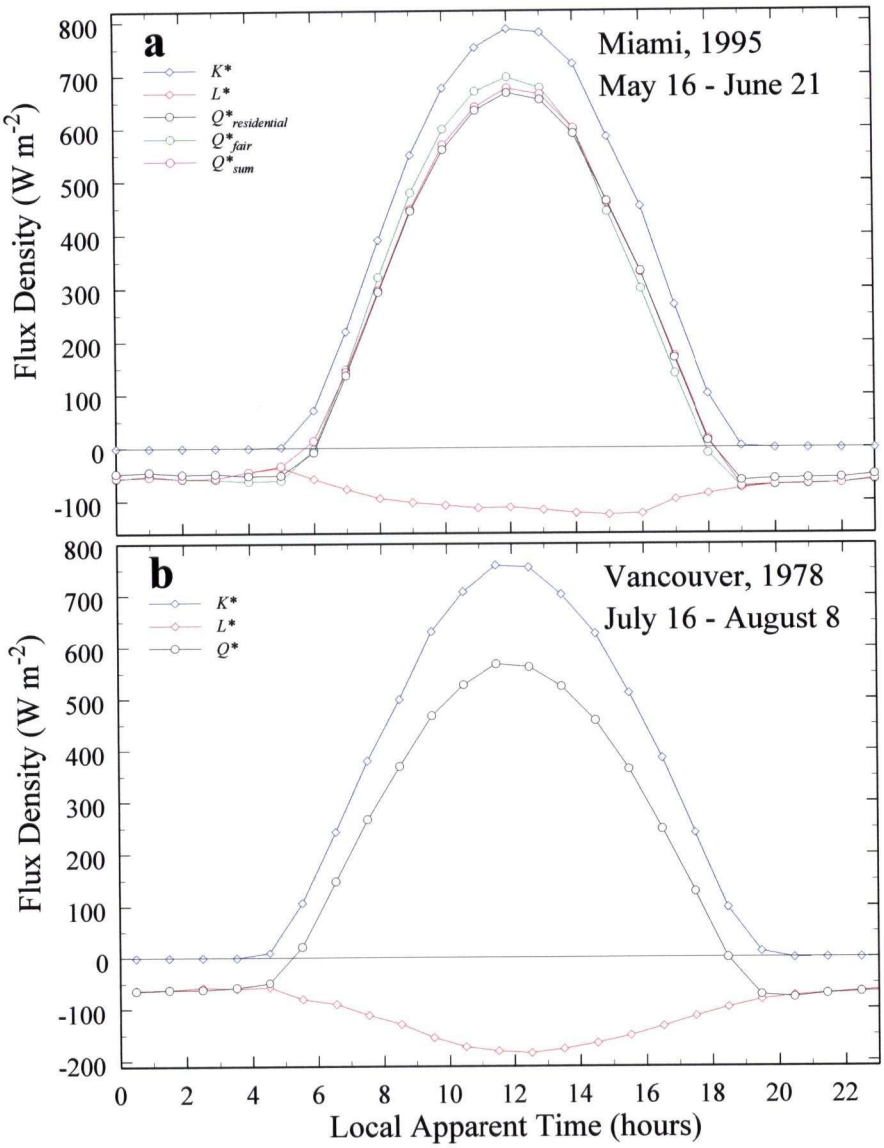

Fig. 3.4 Measured net radiative flux densities. Ensemble hourly averages over Residential sites during periods with clear skies in a) Miami, this study, and b) Vancouver (T. R. Oke, *pers. comm.* 1999).

Nocturnal Q^* values in the two cities are quite similar (Fig. 3.4), but at noon, Miami's $Q^*_{residential}$ exceeds Vancouver's Q^* by 100 W m^{-2}, due in large part (73 of 100 W m^{-2}) to daytime differences in the longwave fluxes. $L\downarrow$ in Miami is relatively constant over 24 hours,

averaging 381 W m^{-2}, whereas in Vancouver it shows some diurnal variation, and averages 342 W m^{-2}, which is approximately equal to the noontime value. This variation is presumably due to morning heating of the lower atmosphere, which by midday and through the afternoon is offset by mixing. At noon, Miami's clear sky $L\downarrow$ exceeds Vancouver's by 53 W m^{-2}, and Vancouver's $L\uparrow$ is 20 W m^{-2} greater than Miami's. This $L\uparrow$ difference is likely due to a combination of factors: Vancouver's slightly longer daylength and lower α, and the higher levels of soil moisture in Miami. The latter is supported by the difference in the overall shapes of the $L\uparrow$ graphs: Miami's is a low, almost flat curve that 'peaks' about an hour after noon, consistent with the delay that would presumably be required to heat a damp surface; Vancouver's has a much stronger diurnal range, with a higher maximum (544 vs. 509 W m^{-2}) that occurs just before noon, consistent with a drier, more thermally-responsive surface. The higher $L\downarrow$ in Miami is attributed to the presence of greater amounts of heat and moisture in the urban boundary layer (UBL).

At night in Miami, Q^*_{sum} and Q^*_{fair} are nearly identical (differences < 10 W m^{-2}) as Fig. 3.4a shows, with $Q^*_{residential}$ being a slightly smaller loss (by approximately 5 W m^{-2}). It is understandable that $Q^*_{residential}$ shows smaller nocturnal radiative losses than Q^*_{fair} because the sensor for the former is over a suburb, which has relatively cold roofs, thereby decreasing $L\uparrow$. The fairground, on the other hand, consists largely of ground surfaces which draw on the ground heat reservoir of the previous day and cool less. Further, the slight calibration difference between the two sensors goes in the same direction (Appendix 1). However, it was expected that at night, Q^*_{sum} would agree

more closely with $Q^*_{residential}$ than with Q^*_{fair} because they both obtain their $L\uparrow$ flux from the same, suburban, site. Perhaps the close agreement between Q^*_{sum} and Q^*_{fair} at night is somewhat fortuitous, and the small difference between Q^*_{sum} and $Q^*_{residential}$ is due to differences between the Eppley and REBS instruments.

The three Miami Q^* measurements agree quite closely during the daytime (mostly within 5%), although Q^*_{fair} is slightly larger than the other two. This is either due to differences between the two REBS radiometers (Appendix 1), or between the upwelling fluxes at the fairground and Residential sites. $K\uparrow$ and $L\uparrow$ were not measured separately at the Fairground site because the surface is atypical of suburban Miami. Therefore, attempts to ascribe specifically the differences between net fluxes at the two sites to features of the upwelling fluxes can only be speculative, but presumably the fairground's surface is no cooler than that of the suburb, and therefore a lower albedo at the fairground is the more likely explanation for its higher Q^*.

Given the radiative source areas of the two Q^* sensors, $Q^*_{residential}$ is favoured for the purposes at hand. This is because it measures the surface-affected fluxes ($K\uparrow$ and $L\uparrow$) from the suburban area which is within the source area region of the turbulent fluxes (see Ch. 4). As mentioned, it is expected that $Q^*_{residential}$ will agree with Q^*_{sum}, but only if $K\downarrow$ and $L\downarrow$ do not vary greatly between the Fairground and Residential sites. Since those two Q^* measures agree closely (Fig. 3.4a), $K\downarrow$ and $L\downarrow$ are relatively conservative spatially. Therefore, differences between Q^*_{fair} and $Q^*_{residential}$ are probably due to real radiative differences between the surfaces, and are indicative of intra-urban variability of Q^*.

3.2.2 All-sky Conditions

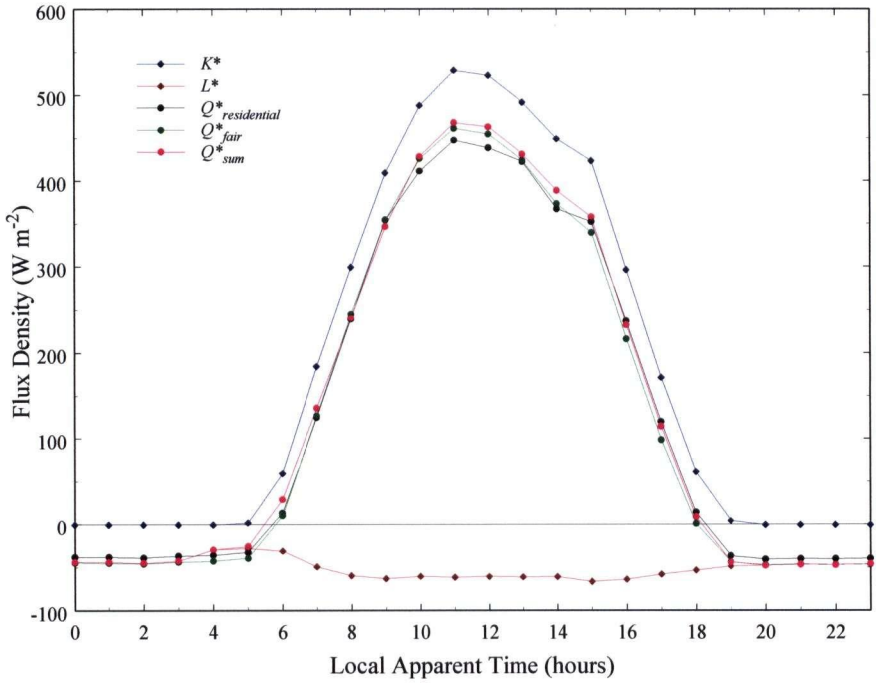

Fig. 3.5 Measured net radiative flux densities. Ensemble hourly averages of observations under all-sky conditions.

Cloud cover differences between the fairground and Residential sites affect $K\downarrow$ and $L\downarrow$. Added to the previously described surface differences, they help explain the fact that the three Q^* measurements do not agree as closely in the daytime (Fig. 3.5) as in Fig. 3.4a. Under all-sky conditions, Q^*_{sum} agrees more with Q^*_{fair} than with $Q^*_{residential}$, because the former two obtain their solar flux at the Fairground site, while the latter may have different cloud cover at the Residential site, 0.7 km to the southeast. Most clouds observed in Miami were convective cumulus and not horizontally extensive, with cloud base areas on the order of a few hundred metres squared. Therefore it is certain that at times, one site was shaded by cloud while the other was not. In view of this, the agreement between the three versions of Q^* in Fig. 3.5 is acceptably, perhaps surprisingly, close.

Daytime energy losses via net longwave radiation (L^*) are reduced under all-sky conditions to about half their clear sky value, due chiefly to the increase in $L\downarrow$ by cloud. $L\uparrow$ is virtually the same under clear and all-sky conditions.

Another similarity, in addition to those mentioned earlier in this chapter, between the flux patterns observed in suburban Miami and those measured at rural sites (e.g. McCaughey 1985) is that Q^* turns negative about an hour before $K\downarrow$ drops to zero. This is observed in other summertime rural studies (e.g. Figs 1.9, 3.13, and 4.23 of Oke 1987), as well as suburban observations made in Vancouver, B.C. in 1977. The timing does of course depend upon the strength of L^* as well as $K\downarrow$ (e.g. see Fig. 3.5 in Oke 1987).

3.3 Observed Surface Albedo (α)

The albedo (α) values in Fig. 3.6 are calculated from the $K\uparrow$ and $K\downarrow$ values in Figs 3.1 and 3.2, using

$$\alpha = K\uparrow / K\downarrow \tag{3.4}$$

The relatively steady downward trend in α through the daytime is not expected, but then neither is the upward trend found by Rouse and Bello (1979) in Hamilton, Ontario, and by Steyn and Oke (1980) in Vancouver. It is most likely to be the result of local control (e.g. horizon obstructions, shade patterns, unusual surface types, dew), or the $K\uparrow$ sensor was not sufficiently level (e.g. tilted up slightly to the east, causing it to see too much upwelling sunlight as the sun rose, and too little as it set).

In the absence of further information it seems most reasonable to restrict consideration to midday values where sun angles and tilt effects should be minimized. Of the total energy delivered to the surface daily by $K\downarrow$, about half arrives between 1000 and 1400 LAT, based on

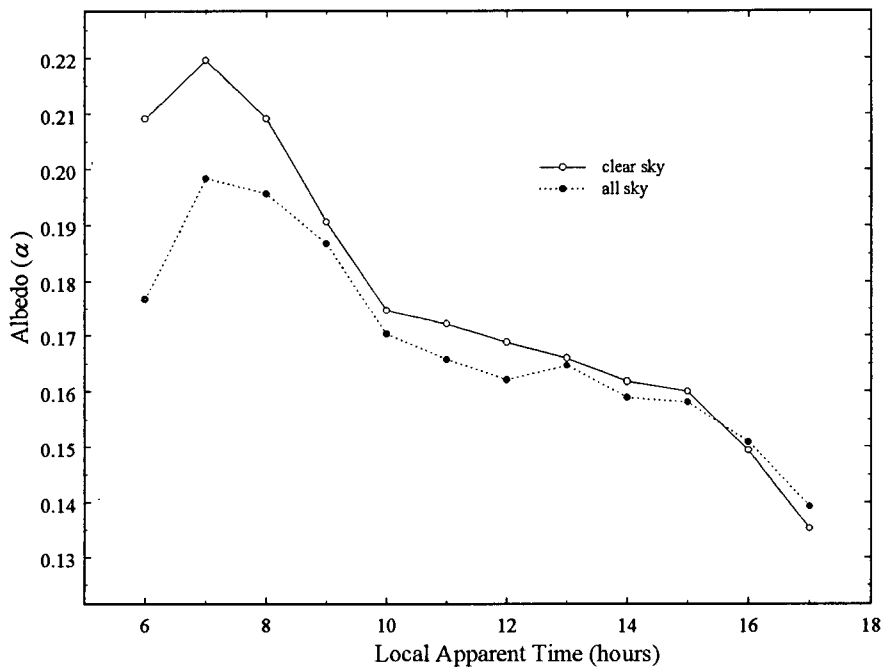

Fig. 3.6 Ensemble hourly averages of surface albedo at the Miami Residential site.

an integration of the $K\downarrow$ curve in Figs 3.1 or 3.2, and solar zenith angles are less than 35°. The average observed albedo during this time is 0.168 under clear skies, and 0.164 under all-sky conditions. The curves are reasonably flat in this period and these values are reasonably consistent with the average α of 0.15 (Oke 1988), based on a survey of many suburban experimental studies.

3.4 Observed Surface Temperature (T_o)

The apparent surface radiant temperature (T_o) is calculated from $L\uparrow$ using the Stefan-Boltzmann equation:

$$T_o = (L\uparrow / \varepsilon_o \sigma)^{0.25} \qquad \text{(K)}, \tag{3.5}$$

where T_o is in degrees Kelvin, ε_o is the surface emissivity, and σ is the Stefan-Boltzmann proportionality constant = 5.67×10^{-8} W m^{-2} K^{-4}. Arnfield (1982) suggests ε_o values of 0.953 and

0.944 for low and high-density residential areas, respectively, and because the Miami study area more closely resembles his description of the former, T_o was calculated using an ε_o of 0.95. It was also calculated using an ε_o of unity, i.e. a black body emitter. As will be shown, results suggest that ε_o for the Miami site is closer to 0.95 than to 1.0.

Air temperature (T_a) data were available from the top of the 40 m tower at the Fairground site, and the 2 m screen observations (downloaded from a U.S. National Climate Data Center ftp server) were made at Miami International Airport. Although the airport is 10 km northeast of the study area, the air temperature observations from the two locations correlate well, due in part to the fact that both are approximately 12 km northwest of the Atlantic coast, giving them similar fetch areas with respect to the predominantly southeasterly winds. As expected in clear sky conditions, the 2 m T_a observations are warmer than those at 40 m during the day, and the two are virtually the same at night (Fig. 3.7). It is noteworthy that it takes until midnight, six hours after sunset, until the two T_a values are essentially equal. This behaviour is consistent with the presence of an urban heat island (Oke 1995).

In Fig. 3.7, the T_o curve with $\varepsilon_o = 0.95$ suggests that the surface is always warmer than the air directly above it. The implication of such a temperature structure is that the turbulent sensible heat flux, Q_H,would be positive at all hours; heat would be convected upward, away from the surface, by day and night. Eddy correlation observations of Q_H (ch. 4) do not show this to be the case. The T_o curve with $\varepsilon_o = 0.97$ illustrates a situation that agrees more closely with Q_H observations, suggesting that the actual ε_o of the Miami site is close to that value. However, this line of reasoning cannot be taken too far because the sites are not identical and a lapse rate calculated in this manner is clearly open to errors.

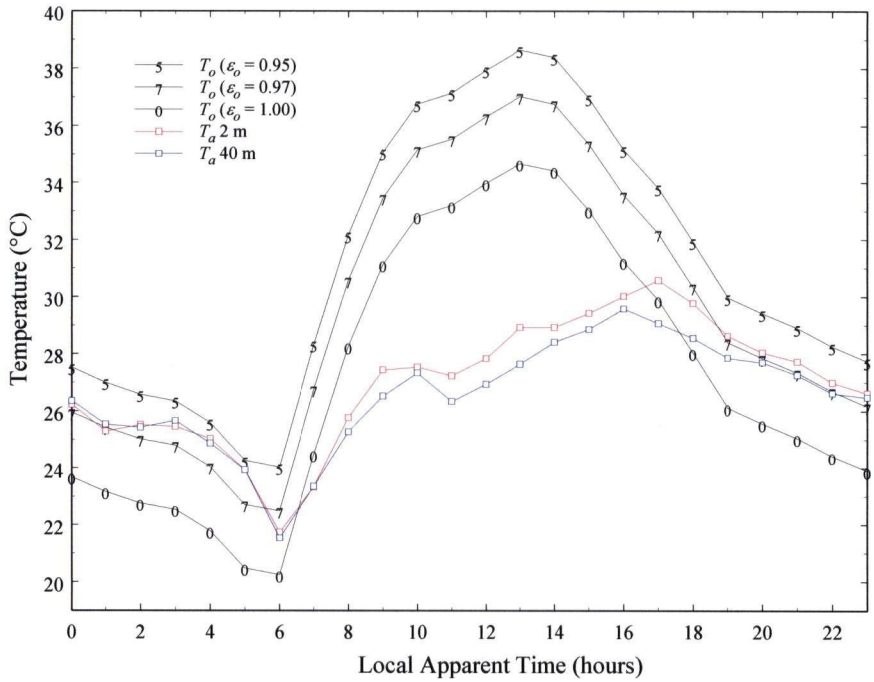

Fig. 3.7 Hourly ensemble averages of apparent surface radiant, and air temperatures observed under clear sky conditions. T_o is calculated from $L\uparrow$, using the indicated values of ε_o. (No boxplots are presented because insufficient clear sky data were collected).

The ε_o = 1.0 curve is perhaps in agreement with intuitive conceptions of rural surface microclimates in general, in which the surface is colder than the overlying air at night, becomes warmer than the air shortly after sunrise, is warmer throughout the day, and becomes cooler at or shortly before sunset. The time lag from solar noon to the maximum observed temperature for each curve is also unsurprising, for a rural or urban environment. T_o peaks at 1300 LAT, and the T_a curves peak hours later, shortly before sunset, corresponding to the time required to achieve maximum heating of the top few centimetres of the surface, and the bottom 40 m of the atmosphere, respectively. Validation of intuitive models is satisfying, but here it belies the likelihood that this site's ε_o lies between 0.95 and 1.0, and that the temperature regime is not quite as flashy as depicted in Fig. 3.7. A value close to 0.97 seems reasonable. A great deal of water is present in the surface: in canals, soil, and vegetation, giving the surface a large thermal

inertia, and enabling it to store large quantites of energy. This energy keeps the air at 2 m warmer than that at 40 m for the first half of the night, and probably keeps the surface warmer at night than the T_o ($\varepsilon_o = 1.00$) curve indicates. Heat storage will be discussed in chapter 4.

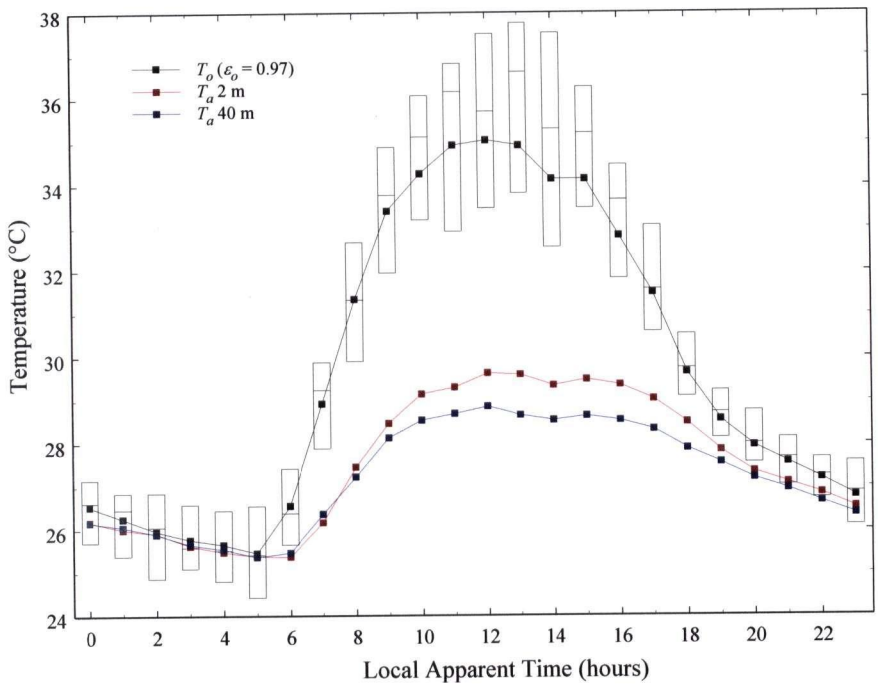

Fig. 3.8 Ensemble hourly averages of apparent surface radiant, and air temperatures observed under all-sky conditions. T_o is calculated from $L\uparrow$, using ε_o = 0.95. In boxplots the top of each box corresponds to the 75th percentile of that hour's data; the horizontal line within is the median, and the bottom is the 25th percentile.

The all-sky temperature data (Fig. 3.8) follow a smoother diurnal curve than the clear sky case because here the ensemble average is meaningful. The dip in all three curves at 1400 LAT is due to shading by cumulus clouds, which tend to appear and congregate in the afternoon. Several features in Fig. 3.7 are also present here: the greater lag from solar noon to maxima in the T_a curves, compared to the T_o lag, and the 2 m T_a is again slightly larger than the 40 m value until midnight. A small difference between the two figures is that T_o is in phase with solar noon under all-sky conditions. This may be due to a reduction of early afternoon temperatures caused by prolific cloud production during that part of the day.

3.5 Parameterization of Radiation Fluxes

A full set of radiation observations, such as those presented here, is rarely available. Therefore, for routine operational and modelling work it is useful to have parameterizations and simple calculations of radiative fluxes. The following section uses the observed fluxes to check the validity and applicability of commonly used rural parameterizations in an urban context. It is possible to calculate the components of (1.1) from astronomical data and readily available screen-level observations such as T_a and e_a. $K\downarrow$ can be computed from the local solar elevation angle (ϕ), which requires knowledge of the site's latitude and longitude, and the time and day number. $K\uparrow$ can then be estimated using a reasonable α, and $L\downarrow$ can be parameterized using T_a, or T_a and e_a. Q^* can be estimated from $K\downarrow$, since they have a strong linear correlation, leaving $L\uparrow$ to be found as a residual, although $L\uparrow$ thus estimated would be of limited value, because it would contain the errors of the other four terms.

3.5.1 Solar Radiation

Holtslag and Van Ulden (1983) refer to a simple formula for the calculation of clear sky $K\downarrow$ which requires only the solar elevation angle ϕ:

$$K\downarrow = a_1 \sin\phi + a_2, \tag{3.6}$$

where a_1 and a_2 are empirical coefficients. The same paper refers to a_1 values ranging from 910 to 1100 W m^{-2}, and a_2 values from –69 to –30 W m^{-2}. Values of 990 and –30 W m^{-2}, respectively, are used here (Fig. 3.9) with satisfactory results. These values are suggested for temperate, mid-latitude sites (Hanna and Chang, 1992), but efforts to achieve better results by altering a_1 and a_2 have been unsuccessful. Using 1024 and –82 W m^{-2} causes the regression line

to overlap the 1:1 line, but r^2 is unchanged at 0.997, and the standard error of the estimate increases from 16.48 to 17.01 W m^{-2}.

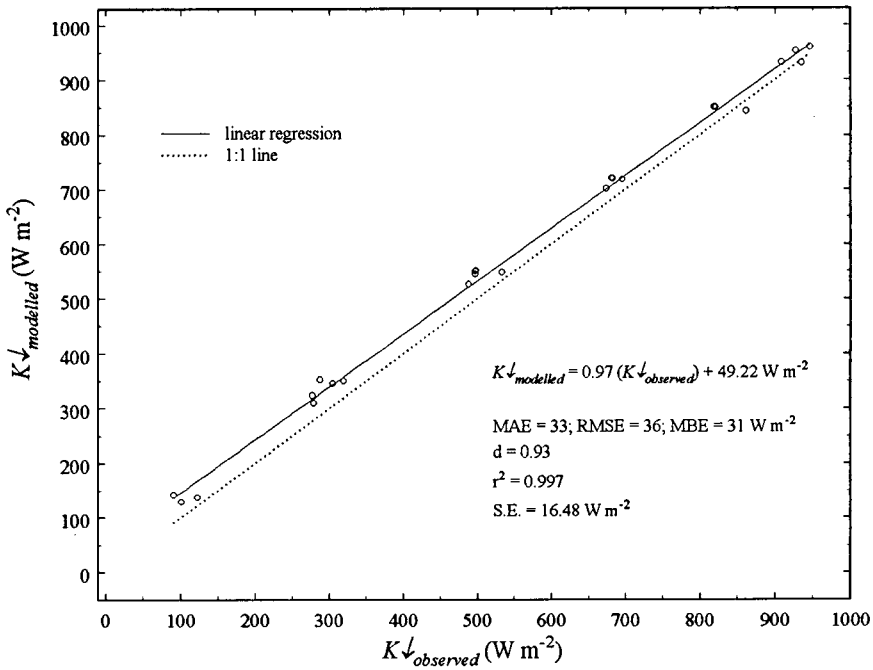

Fig. 3.9 $K\downarrow$ parameterized using the formula recommended by Holtslag and Van Ulden (1983) vs. $K\downarrow$ observed with clear skies.

Nevertheless, the formula works acceptably well (Fig. 3.9), especially considering that the coefficients used are meant for a different climatic zone. Overall (3.6) predicts higher $K\downarrow$ values than were observed, presumably due to decreased atmospheric transmissivity over Miami, as a result of pollution and vapour haze. Comparing time series of $K\downarrow$ modelled and observed reveals the decrease from the modelled to the observed value is greater in the morning than in the afternoon. This may be because the study site was in west Miami, therefore in the morning the solar path is through the more polluted air overlying the downtown area, whereas in the afternoon it is through the less polluted air overlying the Everglades.

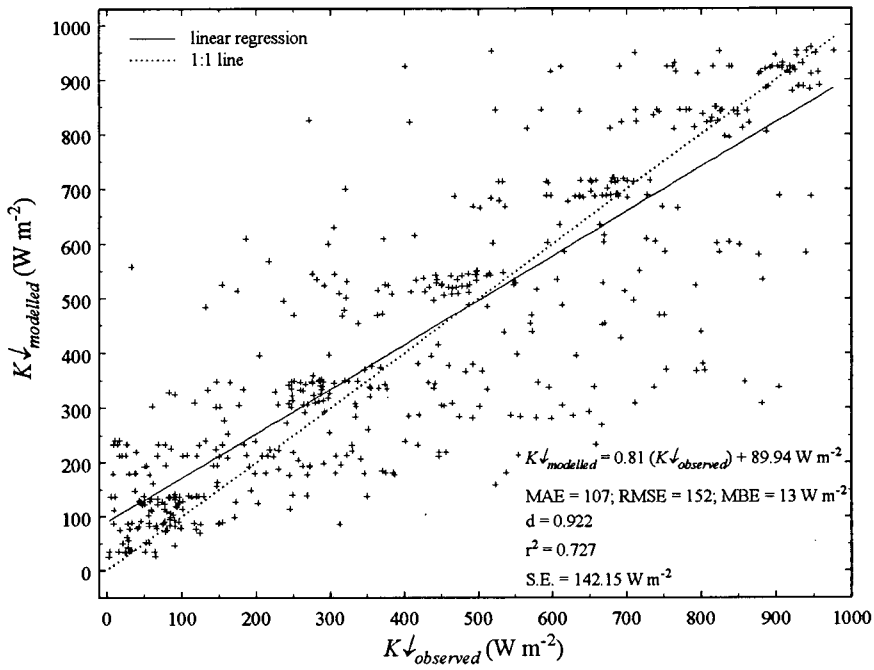

Fig. 3.10 $K\downarrow$ parameterized using the formula suggested by Holtslag and Van Ulden (1983) vs. $K\downarrow$ observed under all-sky conditions.

Holtslag and Van Ulden (1983) also recommend a simple formula for the calculation of all-sky $K\downarrow$ from ϕ and fractional cloud cover N:

$$K\downarrow = (a_1 \sin\phi + a_2)(1 - b_1 N^{b_2}), \tag{3.7}$$

where ϕ, a_1, and a_2 are as in (3.6), N varies from 0 (no clouds present) to 1 (overcast), and b_1 and b_2 are assumed to be 0.75 and 3.4, respectively, although these values were obtained from 10 years of observations at Hamburg, Germany, and may be expected to vary with cloud type and ceiling height.

The formula is evidently inept at predicting $K\downarrow$ under all-sky conditions (Fig. 3.10), although results are undoubtedly worsened by the fact that $K\downarrow$ was observed at the study site, whereas the hourly cloud fraction values were recorded at the airport, 10 km away. Given the high degree of spatial and temporal variability in cloud cover in Miami, this

discrepancy can be expected to significantly worsen performance. Altering a_1 and a_2 to force the regression line to lie on the 1:1 line by changing a_1 from 990 to 1319 W m^{-2} and a_2 from –30 to –259 W m^{-2} does not appreciably improve $K\downarrow$ estimates, because r^2 only improves from 0.727 to 0.749, but the standard error increases from 142.15 to 164.98 W m^{-2}.

3.5.2 Longwave Radiation

Prata (1996) presents a summary of commonly available formulae to calculate clear sky $L\downarrow$: the Swinbank (1963) and Idso-Jackson (1969) formulae require only near-surface air temperature (T_a, in K) as an input, while the other four, Brutsaert (1975), Satterlund (1979), Idso (1981), and Prata (1996), use the near-surface water vapour pressure (e_a, in hPa) as well as T_a. The equations are as follows, and all give $L\downarrow$ in W m^{-2}:

Swinbank's 1963 formula:

$$L\downarrow = 9.2\ 10^{-6}\ T_a^2\ \sigma\ T_a^4. \tag{3.8}$$

Idso-Jackson's 1969 formula:

$$L\downarrow = [1 - 0.261\ \exp\{-7.77\ 10^{-4}(273 - T_a)^2\}]\sigma\ T_a^4. \tag{3.9}$$

Brutsaert's 1975 formula:

$$L\downarrow = 1.24\ (e_a/T_a)^{1/7}\sigma\ T_a^4. \tag{3.10}$$

Satterlund's 1979 formula:

$$L\downarrow = 1.08[1 - \exp\{-e_a^{T_a/2016}\}]\sigma\ T_a^4. \tag{3.11}$$

Idso's 1981 formula:

$$L\downarrow = [0.7 + 5.95\ 10^{-5} e_a\ \exp\{1500/T_a\}]\sigma\ T_a^4. \tag{3.12}$$

Prata's 1996 formula:

$$L\downarrow = [1 - (1 + \xi)\ \exp\{-(1.2 + 3.0\xi)^{1/2}\}]\sigma\ T_a^4, \text{ where } \xi = 46.5(e_a/T_a). \tag{3.13}$$

Swinbank (1963) suggests two different equations; one uses the above coefficient of 9.2, and the other uses 9.365. Subsequent studies have alternated between the former (e.g. Prata 1996), and the latter (e.g. Paltridge 1970, Saunders and Bailey 1997).

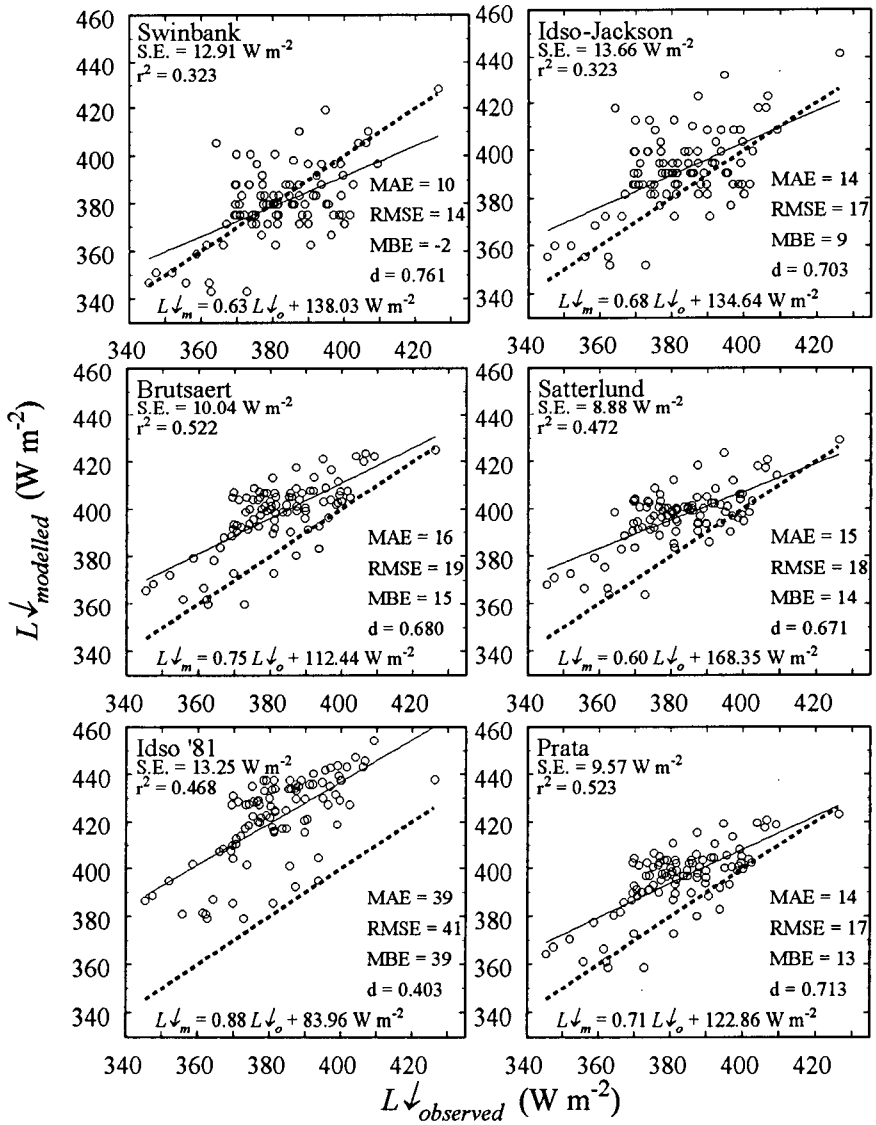

Fig. 3.11 Hourly averages of $L\downarrow_{modelled}$ ($L\downarrow_m$ in the linear regression equations) versus $L\downarrow_{observed}$ ($L\downarrow_o$ in the linear regression equations), under clear sky conditions. In all cases, n = 95, MAE, MBE, and RMSE are in W m^{-2}, the heavy dashed line is the 1:1 line, and the solid line is the linear regression line.

All formulae provide reasonable rough estimates of Miami's clear sky $L\downarrow$ (Fig. 3.11), but none stands out as a particularly strong performer. Judging by the standard error and r^2, the two single-input formulae are least discriminating; they have the lowest r^2 values, and the first and third-largest standard errors. They produce a vaguely circular cluster of data points around the 1:1 line, and some outliers. The Willmott statistics give a different impression—according to those, the Swinbank equation does the best job, with the highest d, and the smallest MAE, RMSE, and MBE of the six formulae. The Idso-Jackson equation produces relatively good Willmott statistics also, performing about as well as the best of the four dual-input equations, i.e. Prata's formula. Perhaps the sharpest contrast between the two groups of statistical indicators can be seen in a comparison of the Idso-Jackson and Idso '81 equations. Based on the Willmott statistics, and a cursory examination of the graphs, the Idso '81 formula does a much poorer job, yet it has a slightly lower standard error. The two sets of statistics concur that the Brutsaert, Satterlund, and Prata formulae offer similar performance to one another.

The four dual-input formulae display somewhat better skill according to r^2 and the standard errors, with the Satterlund and Prata formulae producing the best, or perhaps the least disappointing clear sky statistics, with the lowest standard error and the highest r^2 values, respectively (Fig. 3.11). Compared to the present study, Prata (1996) achieved much more impressive results from the six formulae, using four different datasets to compare their output, providing 24 opportunities for evaluation. Of the 24 r^2 values thereby produced, only two were below 0.9; the two single-input formulae (Swinbank, and Idso-Jackson) had r^2 values of 0.86 when used in conjunction with a 229-point dataset, the smallest of the four used in that study. In

the present study, only 95 clear sky data points are available, a limitation which contributes to the lower r^2 values obtained.

No explanation is available as to why the Idso formula so consistently over-estimates $L\downarrow$ in Miami (Figs 3.11 and 3.12). In his comparisons, Prata did not encounter significant differences between the four dual-input formulae; all performed very well. However, an alpine tundra study by Saunders and Bailey (1997) also found significant over-estimation by the Idso '81 equation in comparison to others. Compared to the present study, better estimates of clear sky $L\downarrow$ were obtained by Saunders and Bailey (1997) who, like Prata, used over 200 data points in comparing the formulae.

Under all-sky conditions (Fig. 3.12), which for this study essentially means cloudy conditions, the standard error for each formula is approximately twice its clear sky value. There are three main reasons for this. Firstly, the formulae were designed for clear sky conditions. They were modified as part of this study, by adding the Bolz (1949) cloud correction term (see Oke 1987), so that:

$$L\downarrow_{all\text{-}sky} = L\downarrow_{clear}(1 + aN^2) \qquad (\mathrm{W\ m^{-2}}), \qquad (3.14)$$

where a is 0.2275 for low cloud, 0.185 for mid-level cloud, and 0.06 for high cloud. Mid-level clouds are defined as those with a base elevation of 2 to 6 km above ground; low and high clouds have base elevations below and above that range. N is fractional cloud cover, as in (3.7). This correction assumes that only one level of cloud is present, but often in Miami two or three are present simultaneously, so the correction was modified, based on the assumption that all clouds are uniformly distributed across the sky hemisphere. The amount of mid-level cloud seen

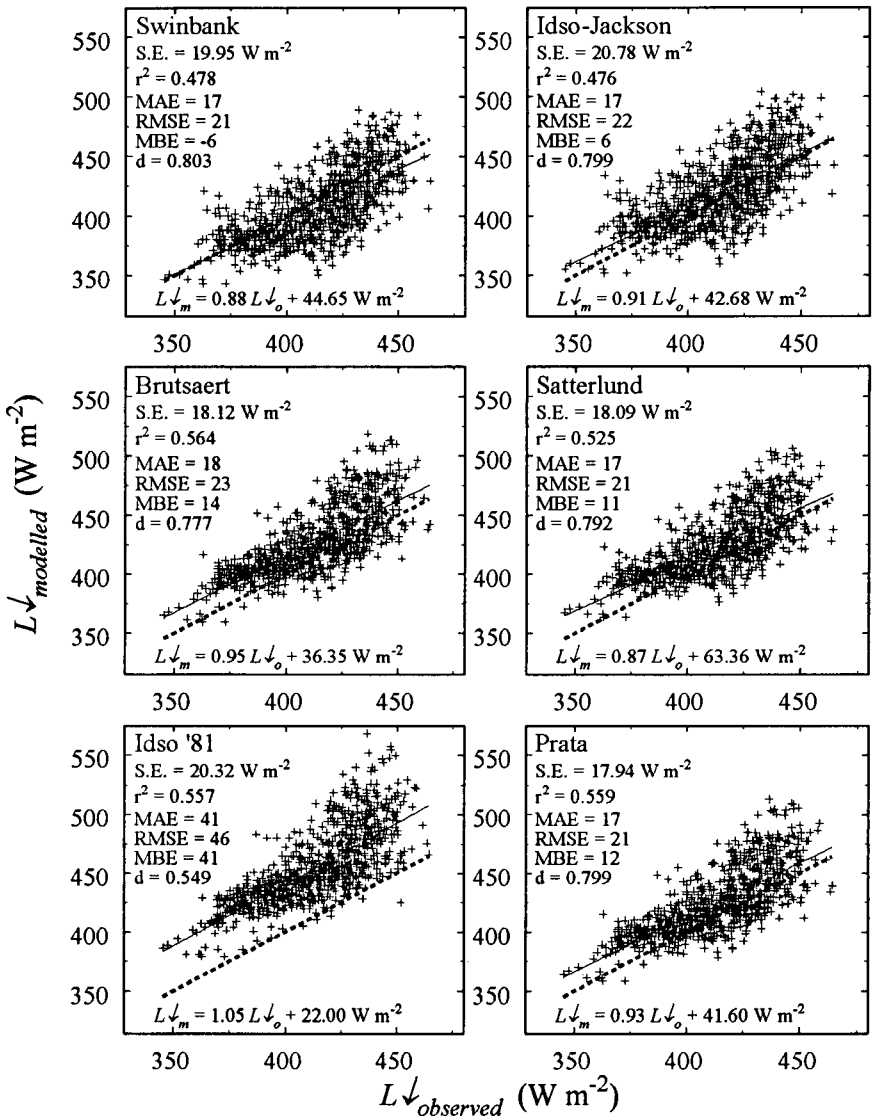

Fig. 3.12 Hourly averages of $L\downarrow_{modelled}$ ($L\downarrow_m$ in the linear regression equations) versus $L\downarrow_{observed}$ ($L\downarrow_o$ in the linear regression equations), under all-sky conditions. Here $L\downarrow_{modelled}$ uses the named equation, modified by the Bolz cloud relation (3.14). In all cases, n = 974, MAE, MBE, and RMSE are in W m^{-2}, the heavy dashed line is the 1:1 line, and the solid line is the linear regression line.

by the surface, for example, is reduced by the fraction of sky obscured by low cloud. This gives

$$L\downarrow_{all\text{-}sky} = L\downarrow_{clear}(1 + a_l N_l^2 + a_m((1-N_l)N_m)^2 + a_h((1-(N_l+(1-N_l)N_m))N_h)^2), \qquad (3.15)$$

where a_l is the low cloud coefficient, a_m is the mid-level cloud coefficient, a_h is the high cloud coefficient, N_l is the low cloud sky fraction, N_m is the mid-level cloud sky fraction, and N_h is the high cloud sky fraction.

This assumption, that clouds are equally distributed across the sky vault, is flawed. There are times when clouds overlap so the correction under-estimates the amount of clear sky seen from the surface.

The second reason for the significant increase in error when estimating all-sky, as opposed to clear sky $L\downarrow$, is due to the fact that the radiation and cloud observations were not co-located. At times, the formulae receive cloudy input, whereas the pyrgeometer 'sees' clear sky, and vice versa.

The third reason is that clouds are physically complex and highly variable in their characteristics. Therefore, assigning three coefficients to all of them is an oversimplification bound to give rise to various degrees of inaccuracy, depending on how closely these crude equations can mimic reality.

The attempt to modify the six formulae to facilitate all-sky $L\downarrow$ estimation was neither decisively successful nor futile. It appears that the cloud correction tends to over-estimate $L\downarrow$ under very cloudy skies (Fig. 3.12). Each scatterplot has an upward curve, with maximum over-estimation occurring when observed $L\downarrow$ is at its highest. An attempt was made to counteract this trend by decreasing the a coefficients in (3.15).

In order to improve the performance of the all-sky $L\downarrow$ formulae, a_l and a_m are both decreased from 0.2275 and 0.185 respectively, to 0.1, and a_h is decreased from 0.06 to 0.03. The results are moderately encouraging (Fig. 3.13); there is an almost 20% reduction of the

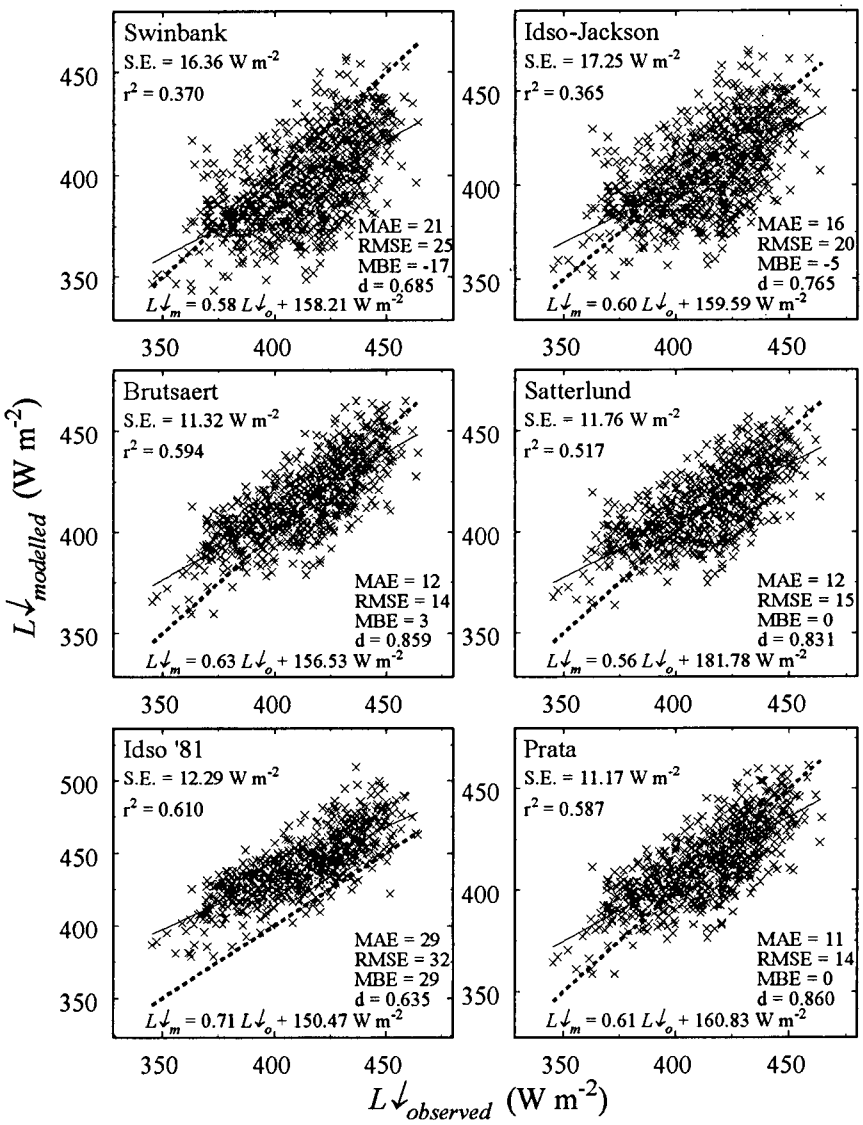

Fig. 3.13 Hourly averages of $L\downarrow_{modelled}$ ($L\downarrow_m$ in the linear regression equations) versus $L\downarrow_{observed}$ ($L\downarrow_o$ in the linear regression equations), under all-sky conditions. Here the a coefficients of the cloud relation (3.15) have been decreased in order to lessen the upward curve exhibited by the plots in Fig. 3.12. In all cases, n = 974, MAE, MBE, and RMSE are in W m^{-2}, the heavy dashed line is the 1:1 line, and the solid line is the linear regression line.

standard error in the single-input formulae, and nearly 40% reduction in the dual-input formulae. Also, r^2 is increased for the Brutsaert, Idso, and Prata formulae, but decreased substantially for the single-input equations and slightly for the Satterlund formula. Perhaps the lower a coefficients produce better results because the clear atmosphere is warm and humid in Miami,

thus the boost provided by clouds to already high $L\downarrow$ fluxes is less than expected.

The $L\downarrow$ formulae assume that screen-level values of air temperature (and humidity for the dual-input methods) give a good representation of the emissive power of the overlying atmosphere. This is predicated on the fact that most of $L\downarrow$ at the surface originates in the lower portions of the boundary layer, where variations of T_a and e_a are greatest. This is true for bulk values over a day, but it ignores the characteristic diurnal variations of T_a and e_a with height—typically lapse by day and inversion at night.

Paltridge (1970) recognized this and showed a recurrent diurnal over- and under-estimation of the Swinbank equation. Use of the screen-value results in over-estimates by day when the atmosphere above the screen is cooler, and vice versa at night. This systematic diurnal 'error' contributes to scatter in Fig. 3.11. In his figures, Paltridge uses $L\downarrow_{observed} - L\downarrow_{modelled}$, but here the reverse is used, for two reasons. Firstly, using $L\downarrow_{modelled} - L\downarrow_{observed}$ gives plots that are above zero when the equations are over-estimating, and below it when they are under-estimating, which makes sense intuitively. Secondly, the Willmott statistics use $L\downarrow_{modelled} - L\downarrow_{observed}$, so that, for example, MBEs are positive when formulae are over-estimating, and negative when they are under-estimating.

Ensemble hourly averages of $L\downarrow_{modelled} - L\downarrow_{observed}$ were computed from the scatterplot data in Fig. 3.11. This shows that the single-input formulae tend to exhibit a sinusoidal pattern, under-estimating $L\downarrow$ at sunrise, and over-estimating at sunset (Fig. 3.14). Paltridge (1970) also found a sine wave, but in his study it is shifted so that maximum over-estimation occurs at 1500 LAT, and under-estimation is at night; (observations from 2300 through midnight to 0700 LAT were evidently unavailable in that study). Therefore the results from the Swinbank [9.2] equation

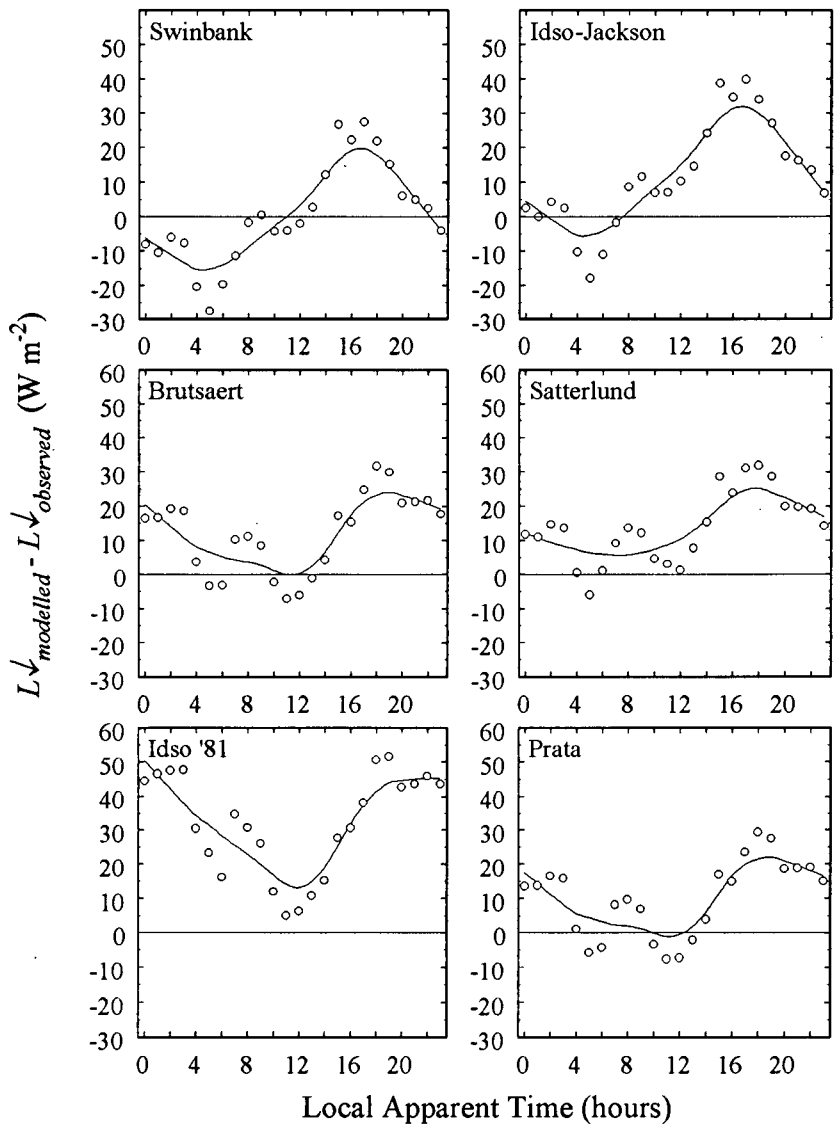

Fig. 3.14 Ensemble hourly averages of $L\downarrow_{modelled}$ minus $L\downarrow_{observed}$, under clear sky conditions. The line on each plot uses weighted least squares.

(Fig 3.14) show an over-estimation maximum that is delayed by about two hours in comparison to Paltridge's (1970) output from the [9.365] version of the formula. (The different coefficients affect the amount of over- or under-estimation, but not the timing of the sine wave.) This may be due to the fact that the Miami data are urban, and are also subject to sea/land breezes.

Of the dual-input formulae, the Brutsaert, Satterlund, and Prata equations produce

similar outputs from the Miami data, with maximum over-estimation at sunset, and with the best estimates coming at midday (Fig. 3.14). The Idso formula also performs best at midday, but that still means $L\downarrow$ over-estimation by about 20 W m^{-2}; it is at its worst at midnight, when over-estimation increases to nearly 50 W m^{-2}. Overall, clear sky $L\downarrow$ is over-estimated by all four of the dual-input equations, possibly because they over-estimate the contribution of e_a to ε_a because of a sharper drop in e_a at the top of the mixing layer (Fig. 2.6a) over Miami. South Florida is dominated by a marine atmospheric layer over tropical ocean, leading to high e_a in the surface and mixing layers, which may give rise to a larger (than in the midlatitudes) decrease at the top of the mixing layer. For example, over the tropical Atlantic Ocean, specific humidity (q) has been observed to drop from about 7.5 g kg^{-1} at a height of 50 m to 1 g kg^{-1} at 5000 m (Oke 1987), whereas in typical midlatitude profiles, this decrease is on the order of 3 to 4 g kg^{-1} (R. B. Stull, *pers. comm.* 1999).

An attempt was made (Paltridge 1970) to correct for the sinusoidal error in the clear sky $L\downarrow$ estimate of Swinbank's equation by adding or subtracting the appropriate amount. Here this is repeated, but the 'correction' is calculated by the following iteratively derived equation:

$$L\downarrow_{corrected} = L\downarrow_{modelled} + (c_1 \sin\{(H + c_2)(\pi / 12)\} - c_3), \tag{3.16}$$

Formula	c_1	c_2	c_3
Swinbank	17.5	1	2
Idso-Jackson	19	1	13
Brutsaert	12	–2.5	12
Satterlund	10.75	0.5	15.75
Idso '81	17	–5	30
Prata	11.5	–2.5	10.5

Table 3.1 Iteratively derived constants for clear sky $L\downarrow$ formulae's sinusoidal correction equation.

where the sine function is calculated in radians, H is the local apparent time (LAT) in hours, and c_1, c_2, and c_3 are empirical constants with different values for each of the formulae, as shown in Table 3.1.

This correction (3.16) was applied to the clear sky plots in Fig. 3.11 with favourable

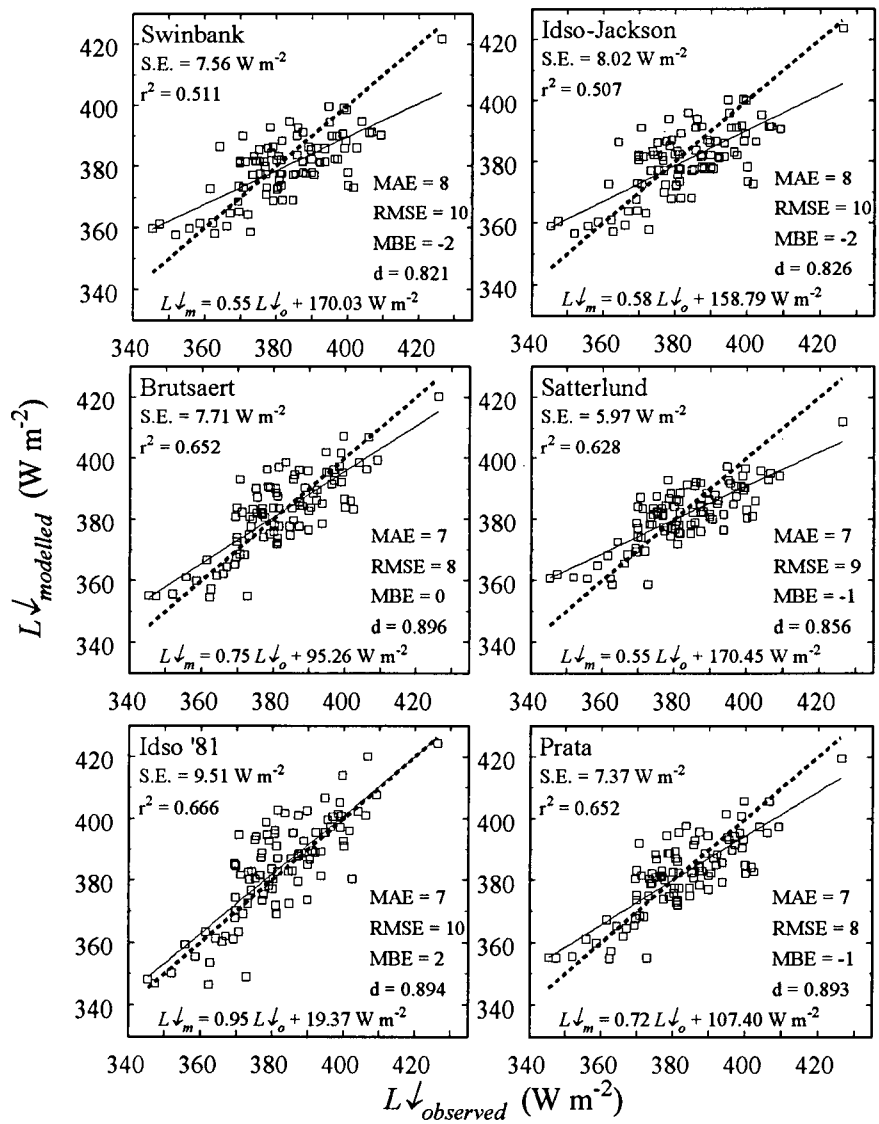

Fig. 3.15 Hourly averages of $L\downarrow_{modelled}$ ($L\downarrow_m$ in the linear regression equations) versus $L\downarrow_{observed}$ ($L\downarrow_o$ in the linear regression equations), under clear sky conditions. This is a sine-corrected version of Fig. 3.11. Here the formulae have been corrected for sinusoidal errors, using (3.16). In all cases, n = 95, MAE, MBE, and RMSE are in W m^{-2}, the heavy dashed line is the 1:1 line, and the solid line is the linear regression line.

results, as shown in Fig. 3.15. Although (3.16) is intended merely as an example of how one might correct for systematic diurnal under- and over-estimation of clear sky $L\downarrow$ by these formulae, generalized coefficients are provided (Table 3.2) to facilitate its use by others.

Formula Type	c_1	c_2	c_3
single–input	18	1	8
dual–input	11	−1.5	13

Table 3.2 Generalized coefficients for clear sky $L\downarrow$ formulae's sinusoidal correction equation.

These generalized values were obtained by averaging those in Table 3.1, excluding the Idso '81 coefficients, because that formula's output is evidently atypical of the dual-input equations.

Naturally, correcting the sinusoidal error in the clear sky formulae brings an improvement in the statistics (Fig. 3.15). The corrected equations that perform best, according to all of the statistical indicators used, are the four dual-input formulae. The Idso '81 equation, which uncorrected produced the worst Willmott statistics of the six formulae (Fig. 3.11), shows the most improvement, performing as well as the other three dual-input equations after correction. The single-input formulae, the Swinbank and Idso-Jackson equations, are slightly better uncorrected than the dual-input formulae, according to the Willmott statistics, but according to the other statistics they are worse (Fig. 3.11). However, all the statistics show that (3.16) brings improvements, and that the dual-input formulae are superior after correction.

Under all-sky conditions the amplitude of the sinusoidal error for each equation is decreased (Fig. 3.16) relative to the clear sky case (Fig. 3.14). This is likely due to moderation by clouds of the diurnal variation of the lapse rate. The error pattern of the

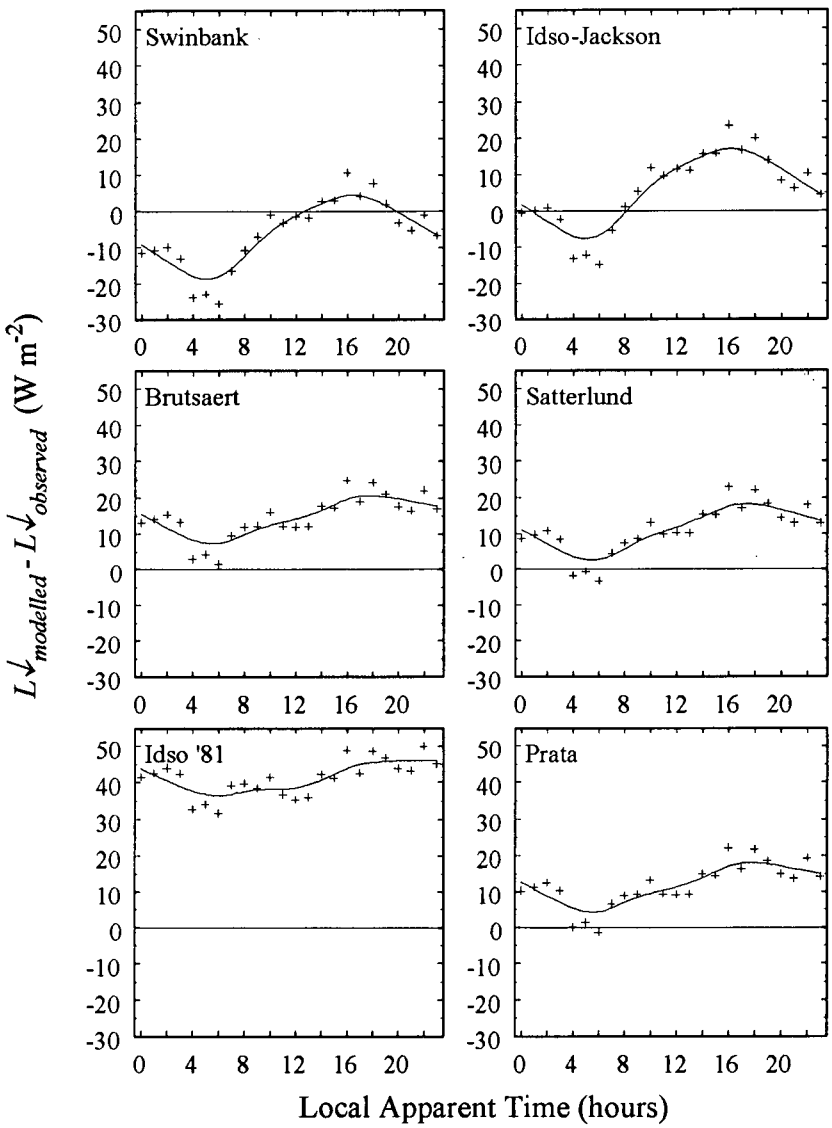

Fig. 3.16 Ensemble hourly averages of $L\downarrow_{modelled}$ minus $L\downarrow_{observed}$, under all-sky conditions. As in Fig. 3.12, the models are modified to account for $L\downarrow$ increases due to clouds. The line on each plot uses weighted least squares.

Swinbank equation is shifted downward, so that a symmetrical combination of under- and over-estimation is replaced by under-estimation all day, except for slight over-estimation from 1300 to 2000 LAT. Curiously the Idso-Jackson equation, which like Swinbank's also depends solely on T_a, shows no such shift.

As in the clear sky case (Fig. 3.14), the Brutsaert, Satterlund, and Prata formulae all

produce similar error patterns under all-sky conditions (Fig. 3.16). The clear sky sine waves increase fairly sharply from 1200 to 1800 LAT, with a gradual decrease from 1800 through midnight to 1200. Under all-sky conditions, however, the waves' increasing portions are damped, resulting in more symmetrical curves, which suggests that the application of (3.16), with all-sky c values, might be more effective. The most dramatic change in the shape of the error pattern, from clear to all-sky conditions, is exhibited by the Idso '81 equation, whose clear sky wave has the sharp afternoon increase of the other formulae, but also a decrease from midnight to noon that is nearly as steep. Under all-sky conditions, absolute over-estimation is still significant, but the wave has a significantly lower amplitude, appearing virtually flat by comparison.

The sine correction applied to the clear sky $L\downarrow$ calculations is not applied to the all-sky $L\downarrow$ because (3.16) is intended as an illustrative exercise, not a generally applicable empirical correction. A visual comparison of the clear sky (Fig. 3.14) and all-sky (Fig. 3.16) sine waves reveals that they are sufficiently similar that (3.16) would likely improve all-sky estimates, but sufficiently different to discourage adoption of (3.16) as a general, 'all-conditions' correction.

Decreasing the a coefficients in (3.15) changes the shape of the sinusoidal error curves of the dual-input equations, but essentially does nothing to the error curves of the single-input formulae but shift them downward (Fig. 3.17). Over-estimation by the dual-input equations is decreased also, but it is the alteration of the shape of the curves that is noteworthy. As before, the Brutsaert, Satterlund, and Prata equations all respond similarly to the change; here the apex and trough of each sine wave from those three formulae in Fig. 3.16 are flattened in Fig. 3.17,

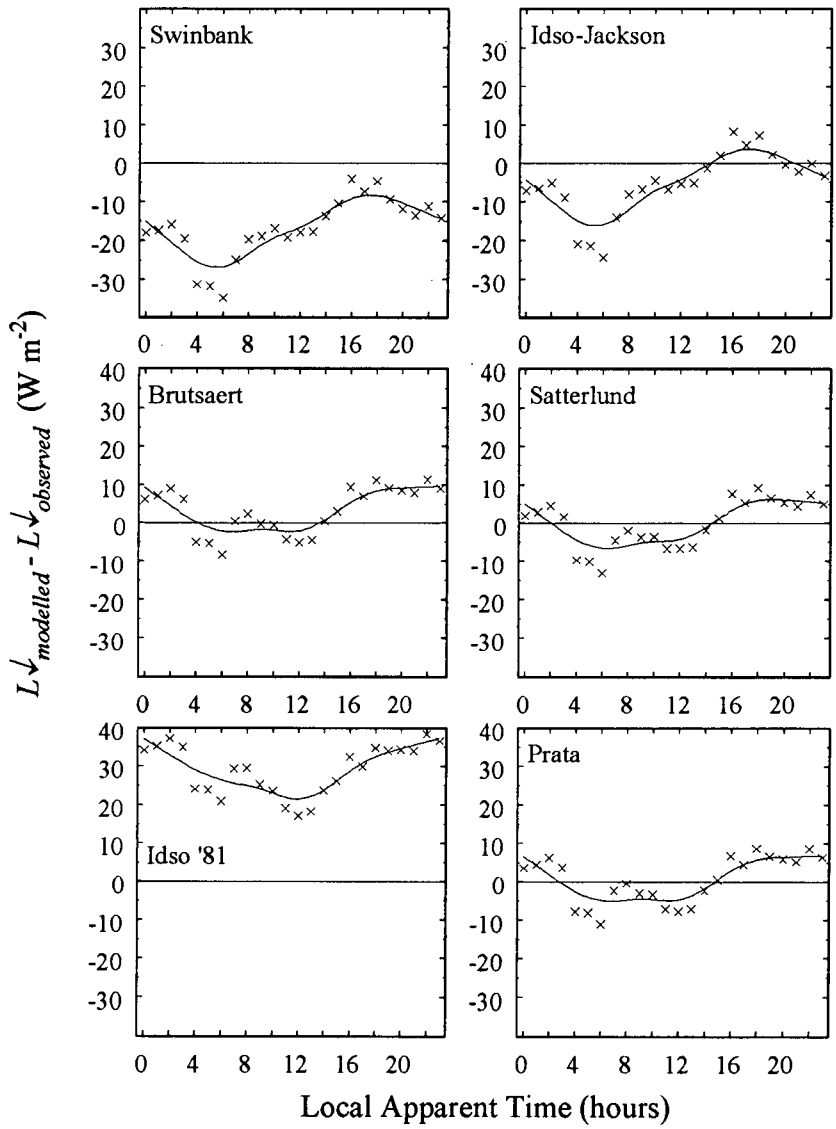

Fig. 3.17 Ensemble hourly averages of $L\downarrow_{modelled}$ minus $L\downarrow_{observed}$, under all-sky conditions. As in Fig. 3.13, the cloud correction term has been modified in order to decrease the upward curve exhibited by the plots in Fig. 3.12. The line on each plot uses weighted least squares.

thus under-estimation becomes reasonably constant at about –4 W m^{-2} from 0500 to 1200 LAT, as does over-estimation at about 7 W m^{-2} from 1800 to 0000, with smooth transitional periods in between. In contrast, the error curve of the Idso '81 formula is less flat with the lower *a* coefficients (Fig. 3.17) than with the unaltered ones (Fig. 3.16). That equation produces

maximum over-estimation at midnight (Fig. 3.17), and a minimum at noon, as is the case under clear skies, although here the amplitude is less than 20 W m^{-2}, whereas under clear skies it is nearly twice that (Fig. 3.14).

3.5.3 Net Radiation

Since the daytime variation of Q^* closely parallels that of $K\downarrow$ it is logical to see if Q^* can

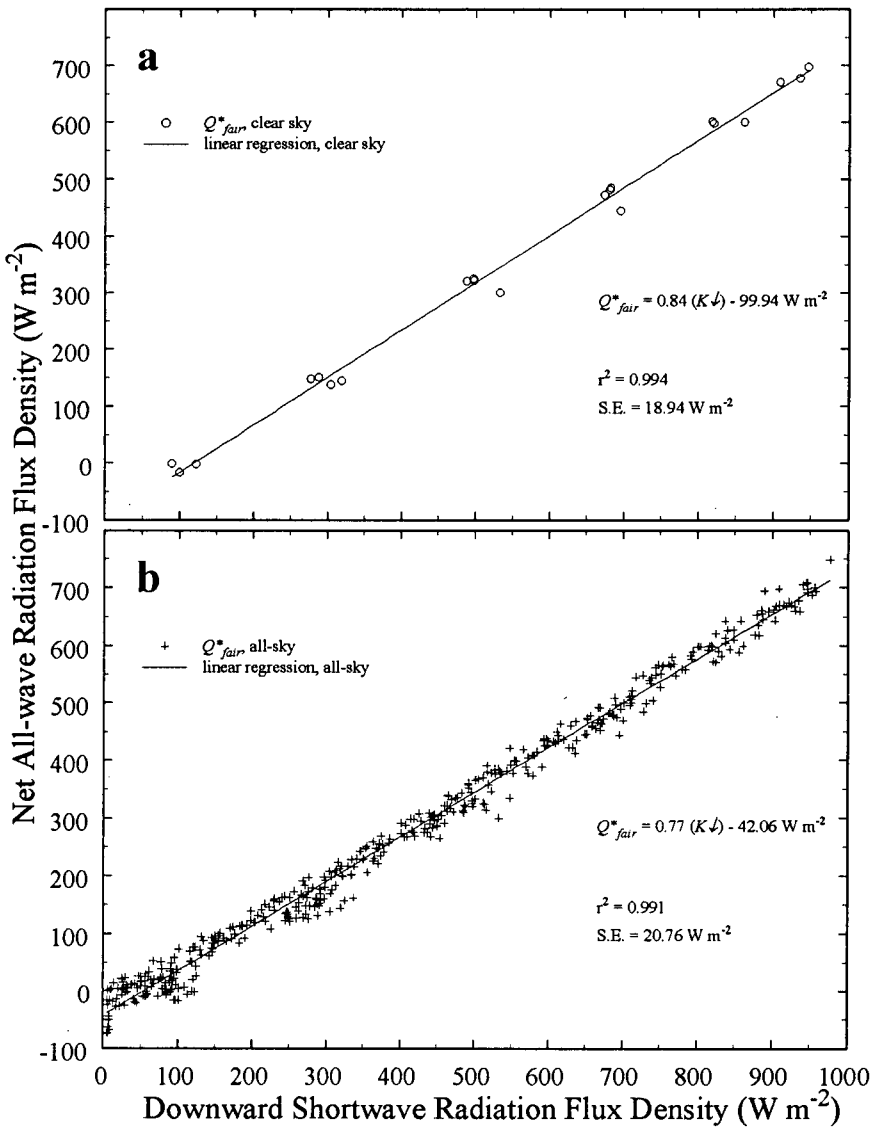

Fig. 3.18 Hourly averages of daytime Q^*_{fair} plotted against $K\downarrow$, a) for cloudless, and b) all-sky conditions.

be obtained from a regression between the two, i.e. $K\downarrow$ is the surrogate. In this manner only $K\downarrow$ measured (or even calculated) is necessary, and since $K\downarrow$ is more readily available, this is potentially useful. There is a strong linear relation between Q^* and $K\downarrow$ ($r^2 > 0.99$) in both cloudless and all-sky conditions (Fig. 3.18). The fit seems relatively constant at both low and high radiation loads. Even in cloudy conditions the standard error is less than 21 W m^{-2}. These results suggest there is merit in using a solarimeter to parameterize Q^*.

The slope coefficient for the clear sky case, 0.84, is slightly larger than the value of 0.79 obtained over a rural surface by Davies and Idso (1979), implying that the urban surface is somewhat more efficient than the rural for converting $K\downarrow$ into Q^*. However, the all-sky coefficient of 0.77 is virtually identical to the 0.79 obtained by Davies and Idso, suggesting that in the absence of abundant direct (as opposed to diffuse) $K\downarrow$, the urban surface has no heightened ability to facilitate this conversion.

Under clear sky conditions, the correlation between K^* and $Q^*_{residential}$ (Fig. 3.20a) is stronger than that with Q^*_{fair} (Fig. 3.19a). In this case a switch to $Q^*_{residential}$ brings an r^2 increase from 0.986 to 0.997, and a drop in the standard error from 28.45 to 12.76 W m^{-2}. This is because K^* is calculated using $K\uparrow$ from the Residential site. Under clear skies, $K\downarrow$ is the same for both sites, but $K\uparrow$ is different, because the Fairground site likely has a slightly lower albedo than the Residential site, as speculated during the discussion of Fig. 3.4a.

Hourly averages of all-sky $Q^*_{residential}$ plotted against K^* (Fig. 3.20b) produce more scatter than Q^*_{fair} vs. K^* (Fig. 3.19b) because the $K\downarrow$ measurement that dominates K^* is taken at the Fairground site. Thus when cloud conditions differ between the two sites, large $K\downarrow$ differences exist, causing poorer correlation between observations made at the different sites

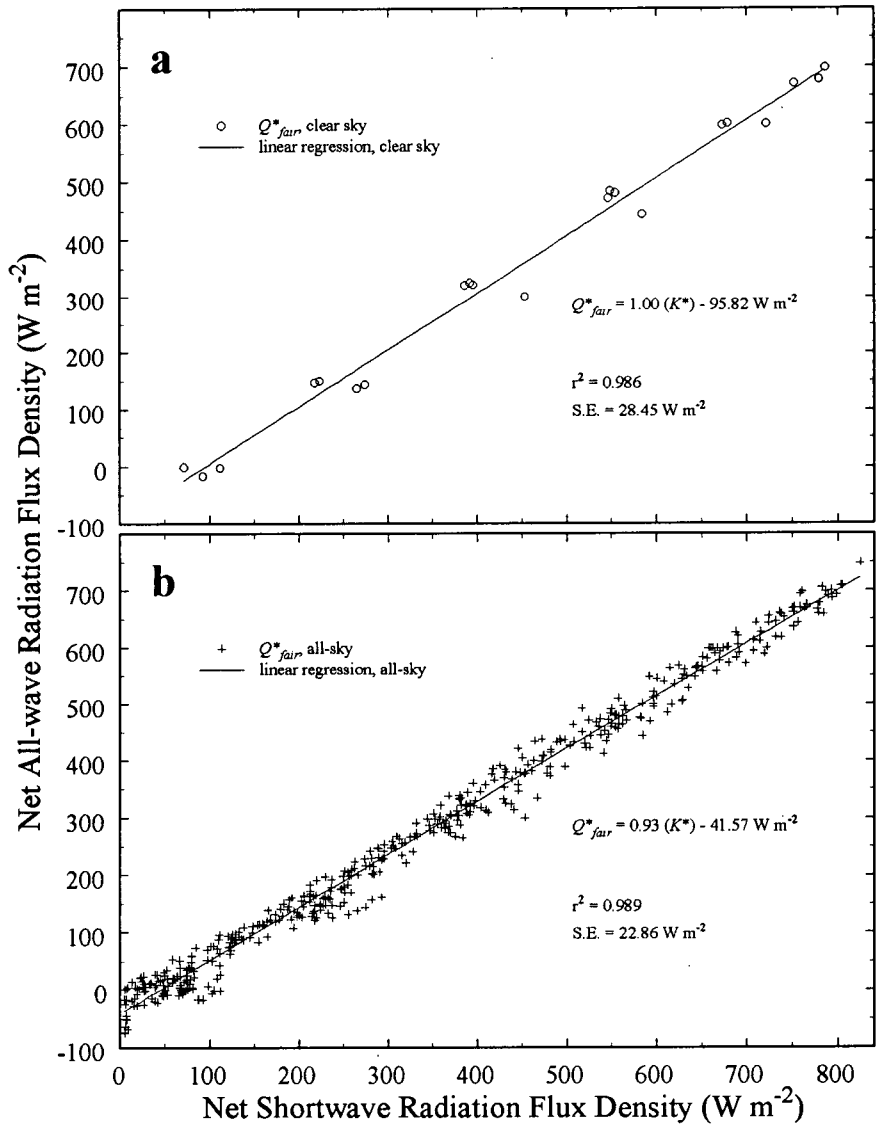

Fig. 3.19 Hourly averages of daytime Q^*_{fair} plotted against K^*, a) for cloudless, and b) all-sky conditions.

than those made at the same site. Hence under all-sky conditions, the standard error is nearly 13 W m^{-2} larger than under clear skies; nevertheless, the correlation between $Q^*_{residential}$ and K^* is reasonably strong, with an r^2 value of 0.971. The conclusion is that colocation of the pyranometer with the site of interest is important to the all-sky case.

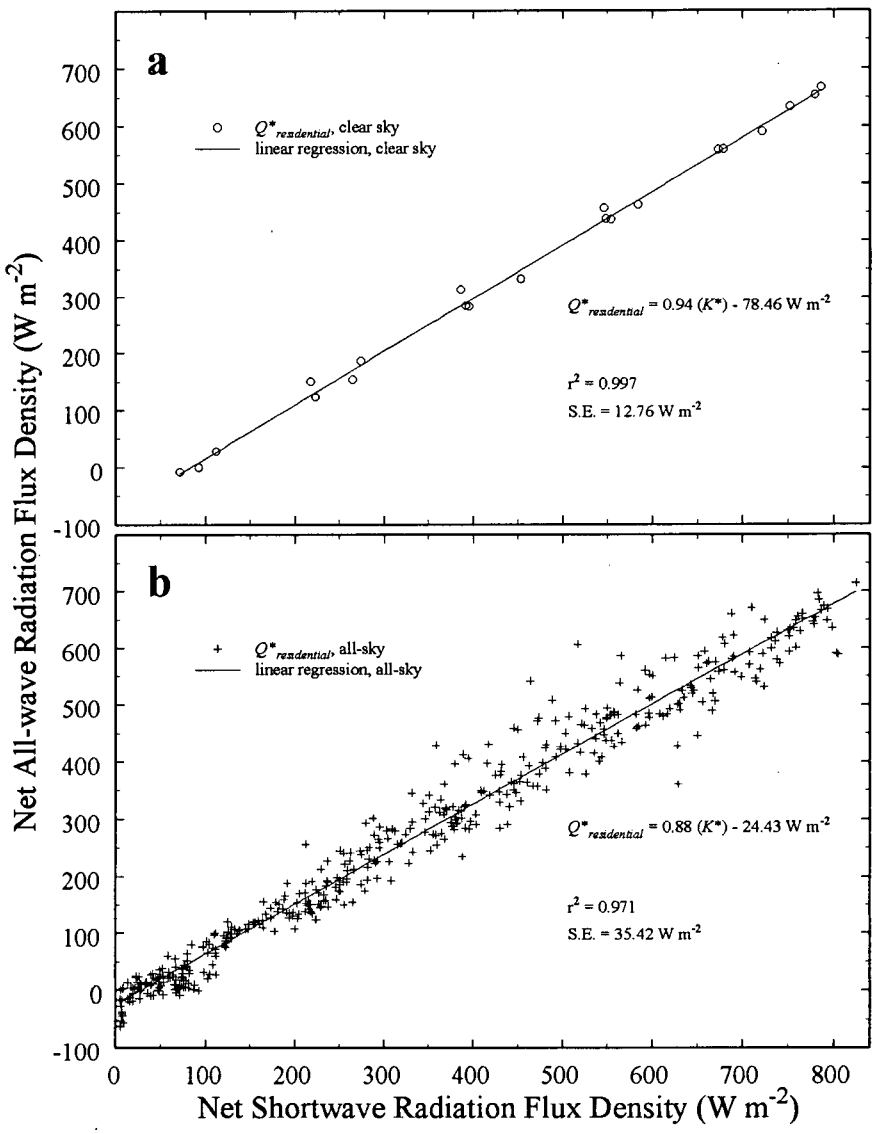

Fig. 3.20 Hourly averages of daytime $Q^*_{residential}$ plotted against K^*, a) in cloudless, and b) all-sky conditions.

Holtslag and Van Ulden (1983) recommend the following formula to calculate Q^* from knowledge of α, observed near-surface T_a, N, the Penman-Monteith surface moisture availability factor α_{PM}, S [$= c_p/(L_e \partial q_s/\partial T)$], and observed or calculated $K\downarrow$:

$$Q^* = ((1-\alpha)K\downarrow + d_1 T_a^6 - \sigma T_a^4 + d_2 N) / (1 + d_3) \qquad (\mathrm{W\ m^{-2}}), \qquad (3.17)$$

where c_p is the specific heat of air at constant pressure, 1004.67 J kg^{-1} K^{-1}, L_e is the latent heat of water vaporization, which is temperature-dependent, $\partial q_s/\partial T$ is the slope of the saturation specific humidity curve, or the Clausius-Clapeyron relation, $d_1 = 5.31 \times 10^{-13}$ W m^{-2} K^{-6}, $d_2 = 60$ W m^{-2}, and d_3 is given by

$$d_3 = 0.38((1 - \alpha_{PM})S + 1) / (S + 1), \tag{3.18}$$

where α_{PM} and S are defined above.

The model inputs were assigned here as if no specialized data were available: an α of 0.15 is used, after the suggestion of a typical suburban value (Oke 1988); $K\downarrow$ is calculated from (3.7); T_a and N are taken from the Miami airport observations; an α_{PM} of unity is used, taken from the moist extreme of the urban range (0.5 – 1.0) suggested by Hanna and Chang (1992); and S is calculated from the airport T_a.

The model output is not sensitive to variations in α_{PM}, so there is no appreciable difference between the results obtained using the calculated α_{PM}, which will be discussed in a chapter 4, and those shown here. In fact, for clear sky conditions reducing α_{PM} to zero, which Hanna and Chang suggest for desert environments, causes r^2 to increase marginally, from 0.991 to 0.992, and brings a slight decrease in the standard error, from 17.77 to 15.89 W m^{-2}. In contrast, the Willmott statistics indicate that an α_{PM} of zero is worse: d decreases from 0.985 to 0.969, and the MAE, RMSE, and MBE all increase by approximately 20 W m^{-2}. Reducing α_{PM} from unity to zero under all-sky conditions brings no appreciable change in r^2, and a decrease in the standard error, from 90.45 to 85.12 W m^{-2}. Again the Willmott statistics disagree, but in this case less decisively than under clear skies. The all-sky MAE, RMSE, and MBE all increase when α_{PM} is reduced to zero, but only by 3, 5, and 14 W m^{-2} respectively—a small percentage of the

already large errors. The change in d is also slight; it decreases from 0.909 to 0.897. One might ask why α_{PM} is included.

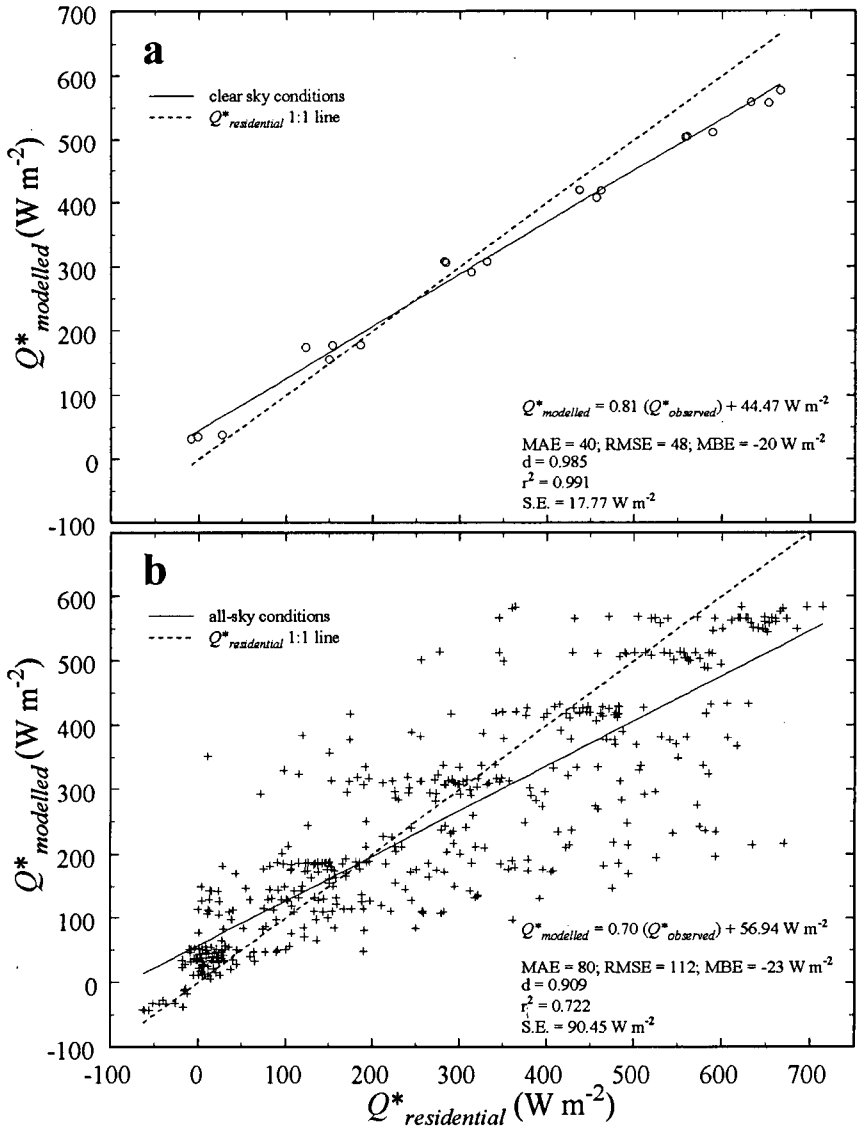

Fig. 3.21 Scatterplot with linear regression of daytime Q^* parameterized using the formula suggested by Holtslag and Van Ulden (1983) against daytime $Q^*_{residential}$ observations, in a) cloudless and b) all-sky conditions.

Under clear sky conditions the Holtslag and Van Ulden formula works relatively well (Fig. 3.21a). Under these conditions (3.7) works well and it seems possible that Q^* can be calculated to an acceptable accuracy for energy balance purposes. There is a tendency to under-

estimate at values greater than 500 W m^{-2}, and to over-estimate below 100 W m^{-2}. Q^* is largely dependent upon $K\downarrow$, therefore since the $K\downarrow$ formula (3.7) performs poorly under all-sky conditions with the given inputs, the Q^* parameterization is also weak in those conditions. This is indeed the case (Fig. 3.21b), but the Q^* formula actually works quite well, considering the errors in the input $K\downarrow$. Equation (3.7) produces a standard error for $K\downarrow$ of 142 W m^{-2} under all-sky conditions (Fig. 3.10). The error in Q^* is just under two thirds of that.

3.6 Conclusions

The chief points made in this chapter are:

- if $K\downarrow$ observations are to be used as part of a measured or parameterized site budget, it is important that the $K\downarrow$ site not be far distant because of spatial variation of $K\downarrow$ under patchy cloud conditions
- observations suggest that $K\downarrow$ in west Miami is slightly lower in the morning than at corresponding solar times in the afternoon due to decreased transmissivity through the urban plume
- urban surface geometry, like that of forests, tends to mitigate the midday peak in surface temperature, resulting in $L\uparrow$ plots that are flattened and essentially in phase with $K\downarrow$
- the surface albedo, averaged over clear and all-sky conditions, is observed to be 0.166, and ε_o is estimated to be 0.97 in suburban Miami
- under clear sky conditions, and without applying any corrections, reasonable estimates of $L\downarrow$ are provided by 5 of the 6 formulae used, with the Idso '81 equation producing the poorest results. Under clear skies, with a correction for systematic diurnal under-

and over-estimation, the dual-input (T_a, e_a) $L\downarrow$ equations consistently outperform the single-input (T_a) equations

- under all-sky conditions, using the Bolz cloud relation, $L\downarrow$ estimation by the formulae is worse than under clear skies, but with errors on the order of 5% from 5 of the 6 equations used, results are still useful. Again the Idso '81 equation appears to be an unusually poor performer, with errors roughly twice as large as the others
- under all-sky conditions a slight modification to the Bolz cloud relation produces improved $L\downarrow$ estimates from the dual-input equations, with approximately a 25% reduction of the errors obtained using the unmodified Bolz relation. Performance of the single-input equations is slightly worsened by the modification, thus in this case the dual-input equations are superior
- Q^* can be estimated satisfactorily from co-located observations of $K\downarrow$

CHAPTER 4. ENERGY BALANCE CLIMATOLOGY

4.1 Observed Turbulent Heat Fluxes (Q_H and Q_E)

No daytime measurements of Q_H and Q_E were made with clear skies when winds were from the acceptable sector (60° to 210°), but 232 hours of nighttime and daytime all-sky observations were made. Based on these data, insights are offered regarding the general characteristics of Miami's summertime energy regime, but the lack of clear sky data means that comparisons with results from other cities should be made with caution.

4.1.1 Turbulent Sensible Heat Flux — Q_H

The ensemble mean daily sensible heat flux peaks with a value of 263 W m^{-2} at 1300 LAT, an hour after the radiation maximum (Fig. 4.1). Q_H turns negative shortly after 2100 LAT, and remains so until 0600.Therefore, Q_H remains positive for several hours after Q^* becomes negative in the evening. This behaviour has been observed at most other urbanized sites (Oke 1988).

The variability of the midday Q_H corresponds to that of the midday T_o. Both have a noticeable decrease at 1400 LAT (Figs 3.8, 4.1), when cumulus clouds tend to form.

The absolute values of Q_H in Miami are similar to those observed in other North American residential suburbs. The midday maximum in the ensemble average is higher than those in Chicago, Sacramento, and Los Angeles, and lower than that of Tucson (Grimmond and Oke 1995). The average total amount of energy channelled into Q_H in Miami in a 24 hour period is 6.74 MJ m^{-2} d^{-1}, and during the daytime ($Q^* > 0$) it is essentially the same, at 6.76 MJ m^{-2} d^{-1}. Both of these values are the 6th largest in a 10-dataset comparison of

Grimmond and Oke, 1999a.

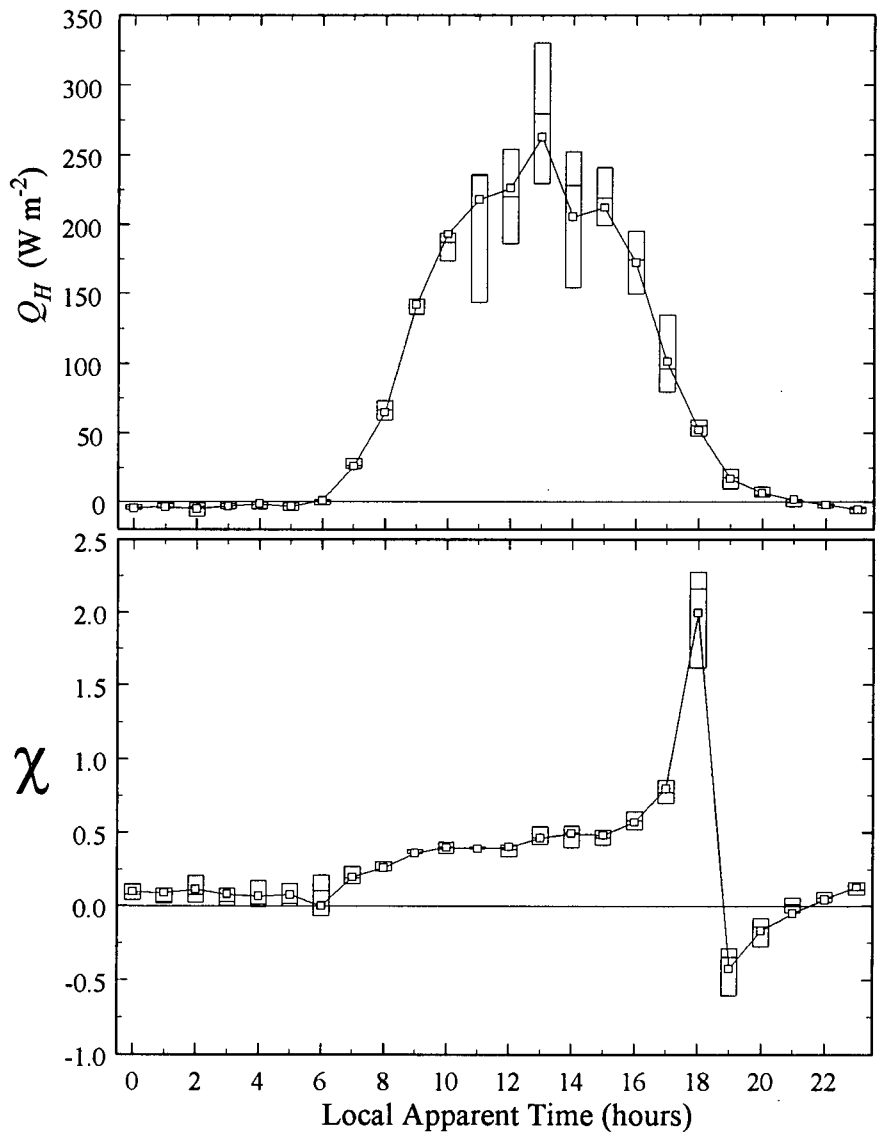

Fig. 4.1 Ensemble hourly averages of Q_H and χ (Q_H/Q^*) over the entire observation period. In boxplots the top of each box corresponds to the 75th percentile of that hour's data; the horizontal line within is the median, and the bottom is the 25th percentile. In the Q_H graph at 1100 LAT, the box represents three data points, and the median is virtually equal to the 75th percentile.

The χ plot is shows remarkably little variability in the daytime (Fig. 4.1). Hence, irrespective of meteorological conditions the share of the net radiation going into convection remains about the same each day. This suggests a robust basis for parameterization. The upward

trend of the daytime χ curve is part of a hysteresis pattern; Q_H is larger, relative to Q^* in the afternoon than in the morning (Fig. 4.1). This is presumably due to the diurnal variation of static stability; increasing instability aids convection relative to conduction, so sensible heat sharing favours ΔQ_S in the morning (Fig. 4.11) but Q_H in the afternoon. The upward spike in the χ curve at 1800 LAT is caused by small values of the net radiation at sunset.

The daytime and all-day absolute values of χ are approximately in the middle of the range of values observed in urban areas (Grimmond and Oke 1999a). Similarly, the diurnal variation in Miami is like those observed in other cities. A notable exception to this is that in Chicago, Los Angeles, Sacramento, and Tucson, χ is observed to be positive at all hours in the all-sky ensemble average (Grimmond and Oke 1995), but not in the clear sky case. Therefore in those studies, Q_H changed sign along with Q^* rather than remaining positive for a few hours in the evening after Q^* turns negative, as is the case in Miami.

4.1.2 Turbulent Latent Heat Flux — Q_E

The temporal behaviour and absolute hourly values of Q_E observed in Miami (Fig. 4.2) are similar to those made in other North American suburban areas (Grimmond and Oke 1995). This is a surprise because larger Q_E fluxes were expected, due to the (presumed) increased availability of heat and moisture at the surface in this humid subtropical city (see Section 4.3.2). The expectation that more radiative energy would be available at the surface in Miami than in higher-latitude cities is not strongly supported by the present observations. During an average 24 hour period, the total amount of radiative energy absorbed by the surface (Q^*) in Miami is 13.80 MJ m^{-2} d^{-1}. If daytime only ($Q^* > 0$ W m^{-2}) values are examined, this figure rises to 15.56 MJ m^{-2} d^{-1}.

In a 10-dataset comparison, Miami's 24 hour Q^* total is the third highest, behind Chicago and Los Angeles (1994), and its daytime total is fourth highest, despite its being the second lowest in latitude (Grimmond and Oke 1999a). With one exception (Tucson in the daytime), all cities in both the daytime and all-day categories that have greater Q^* totals

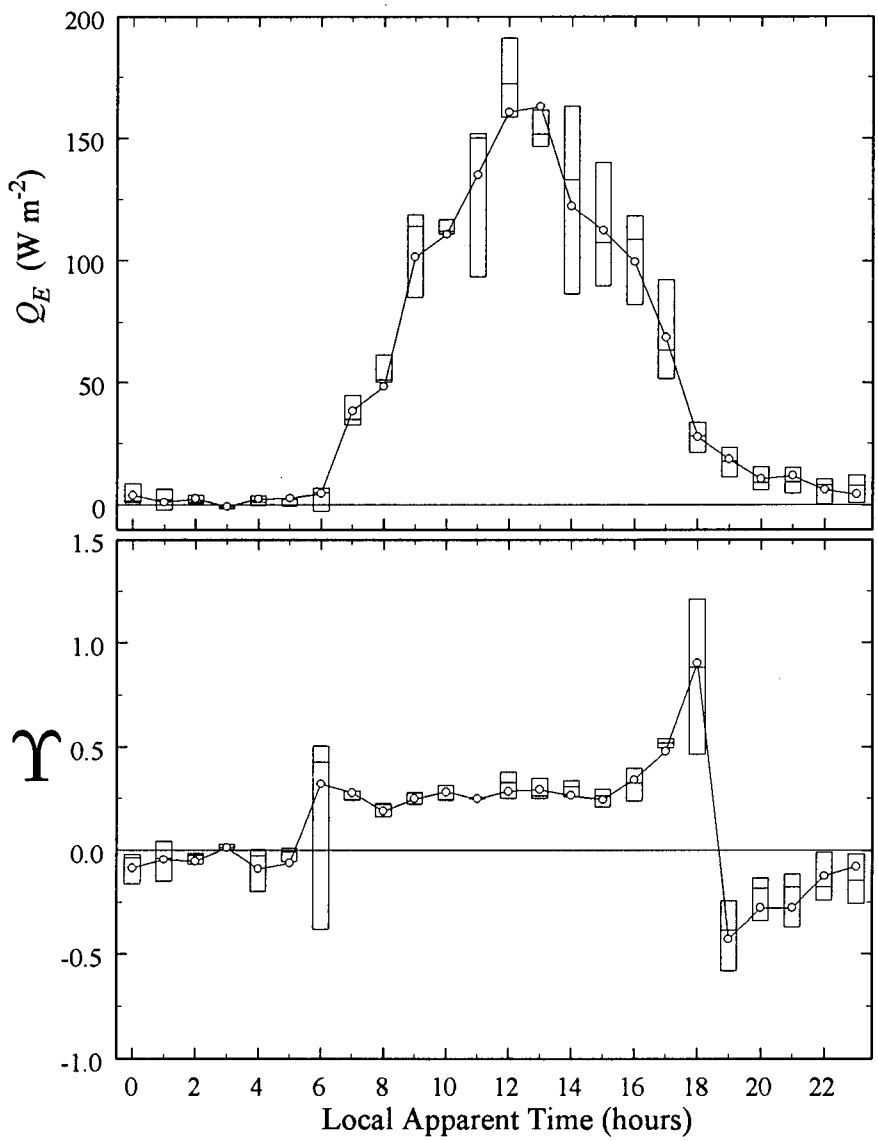

Fig. 4.2 Ensemble hourly averages of Q_E and ϒ (= Q_E/Q^*) over the entire observation period. In boxplots the top of each box corresponds to the 75th percentile of that hour's data; the horizontal line within is the median, and the bottom is the 25th percentile.

than Miami, also have greater Q_E totals. One city (Los Angeles, 1993) has slightly lower Q^* totals, yet slightly higher Q_E totals.

The observed ensemble average turbulent latent heat flux Q_E follows a reasonably smooth diurnal pattern; it describes a unimodal curve with the maximum hourly average (163 W m^{-2}) occurring at 1300 LAT, but the maximum hourly median value (173 W m^{-2}) occurs at 1200 (Fig. 4.2). Evaporation remains positive, although small, throughout the night, which is typical in urban environments; overall the Q_E observations in Fig. 4.2 are similar to those made in Los Angeles in 1993 by Grimmond and Oke (1995).

Unlike the χ plot, the Υ (= Q_E/Q^*) plot does not show an obvious hysteresis pattern. The Υ curve shows that, through the middle eight hours of the day, Q_E is approximately 27% of Q^*. The all-day figure is slightly higher, at 33%. [Initially Fig. 4.2 might suggest that a daytime average of Υ would be larger than an all-day average, and if the hourly values of Υ are averaged, that is true. However, comparing the quantities of energy transferred by Q^* and Q_E, in MJ m^{-2} d^{-1}, leads to an increase in the all-day average Υ because the inclusion of the nocturnal data brings a slight increase to the Q_E total, but an appreciable decrease to the Q^* total; thus the averaged Υ increases from the daytime to the all-day value.]

The averaged Υ values calculated here are the same as those calculated by Grimmond and Oke (1999a) from the same dataset, despite the fact that that study, unlike the present one, uses the Q^* measurement from the Fairground, rather than the Residential site, and 24° to 170°, rather than 60° to 210°, as the preferred wind-direction sector. Like χ, Υ behaves erratically at sunrise and sunset, because the small Q^* fluxes at those times allow a

wide variety of ratios to exist. Aside from those transition periods, Υ, like χ, is robust. Not only is there little variation throughout the daytime, but the standard deviation for any given hour is small.

The overall appearance of the Υ plot is reasonably similar to those of four other cities (Grimmond and Oke 1995). In all five cities Q_E is virtually always positive, so Υ changes sign when Q^* does. The daytime values of Υ are roughly similar in the five cities, averaging 0.3 ± 0.1. In Miami, Chicago, and Los Angeles, Υ lacks the gradual increase from sunrise to sunset that is present in the Sacramento and Tucson data, which have the two lowest evaporation rates of the five.

4.2 Partitioning and Coupling Parameters (β, α_{PT}, Ω)

4.2.1 Theory

General trends in energy partitioning and evaporation may be examined using several descriptive parameters. Here the Bowen ratio β, Priestley-Taylor aridity parameter α_{PT}, and McNaughton and Jarvis (1983) atmospheric coupling coefficient Ω are used in order to scrutinize and describe the surface evaporation climate of Miami.

- β (= Q_H/Q_E) describes the partitioning of available energy A (= $Q^* - \Delta Q_S$) into sensible and latent heat fluxes, and is calculated from the observed fluxes.
- α_{PT} (= Q_E/Q_{Eq}) is defined as the ratio of observed Q_E to the equilibrium evaporation Q_{Eq}, which is the expected evaporation for extensive surfaces with sufficient water (Priestley and Taylor 1972). Q_{Eq} is calculated by

$$Q_{Eq} = [s / (s + \gamma)] (Q^* - \Delta Q_S) \qquad (\mathrm{W\ m^{-2}}), \qquad (4.1)$$

where $s = \partial q_s/\partial T$, which is the slope of the saturation specific humidity vs. temperature curve, or the Clausius-Clapeyron relation, γ is the psychrometric 'constant' = c_p/L_e, where c_p is the specific heat of air at constant pressure (1004.67 J kg^{-1} K^{-1}), and L_e = latent heat of vaporization of water, which is temperature-dependent (see Table 4.1 in Section 4.5.2). s is calculated using (9.9) from Hartmann 1994:

$$\partial q_s/\partial T \approx q_s(T)\,(L_e/R_vT^2), \tag{4.2}$$

where R_v is the gas constant for water vapour, 461 J kg^{-1} K^{-1}; $q_s(T)$ is calculated in units of g of water per g of air using:

$$q_s(T) = [R_d / (R_v \times P)]\,(6.11)\exp\{L_e / R_v\,(1/273 - 1/T_a)\}, \tag{4.3}$$

where R_d is the gas constant for dry air, 287 J kg^{-1} K^{-1}, which is a combination of (B.3) from Hartmann 1994 and the definition:

$$q_s \equiv \rho_v/\rho_{as} = (e_s/R_vT_a) / (P/R_dT_a) = (R_d\,e_s) / (R_vP), \tag{4.4}$$

where q_s is the saturation specific humidity, ρ_v is the saturation density of water vapour, ρ_{as} is the saturation density of air, e_s is the saturation pressure of water vapour, T_a is the near-surface air temperature, and P is the atmospheric pressure in mb. As necessary, s is converted from units of kg of water per kg of air per K, to Pa K^{-1} using (5.4) from Stull 1995:

$$s\,(\text{Pa K}^{-1}) = [s\,(\text{kg/kg K}^{-1}) \times R_vP] / R_d \tag{4.5}$$

α_{PT} is useful to quantify the extent to which evaporation rates depend on A (Thompson *et al.* 1999). For a range of surface types with sufficient moisture, α_{PT} has been found to equal ~1.26 (McNaughton and Spriggs 1989). A suggested explanation for $Q_E > Q_{Eq}$ by about one fourth is that downward mixing of dry, warm air from the inversion at the top of the

planetary boundary layer ('PBL' in Fig. 2.6) increases the demand for evaporation above that driven by A (de Bruin 1989, Oke 1997).

The McNaughton-Jarvis coupling factor is defined as:

- $$\Omega = [1 + \gamma (r_c / r_{aH}) / (s + \gamma)]^{-1}, \quad (4.6)$$

where r_c is the surface or canopy resistance to the vertical transfer of water vapour, and r_{aH} is the aerodynamic resistance to the vertical transfer of heat. The methods used to calculate these resistances are discussed in Section 4.3.1. Ω ranges from 0 to 1.0, and demonstrates the degree of coupling between the surface layer and the PBL. Ω varies directly with r_{aH}, and inversely with r_c. For relatively smooth surfaces with sufficient moisture, r_{aH} is large, and A, rather than the vapour pressure deficit V, dominates in controlling evaporation. In essence, the surface layer is decoupled from the rest of the PBL by the large r_{aH}. However, over rough surfaces such as cities, r_{aH} is signficantly smaller than r_c, and the importance of V increases. Evaporation is then sensitive to the dryness (V) of the whole PBL, thus the surface layer is 'coupled' to the advective influences of the PBL and larger-scale effects. Ω can be as high as 0.8 for grassland and as low as 0.2 for cities (Oke 1997). Other published values of Ω range from ~0.8 for a Sacramento peat farm to ~0.05 for dry sites in Sacramento and Tucson, Arizona (Oke *et al.* 1999b). In a forest on Vancouver Island, B.C., midday summertime Ω values of ~0.27 (calculated by averaging the maximum and minimum monthly median values) have been observed. At the same site during the winter, averaging the maximum and minimum monthly means gives Ω = 0.87 (Humphreys 1999).

4.2.2 Results

The all-day and daytime averages of β, 1.47 and 1.55 respectively, are greater than unity, indicating that more energy is going into heating the air than evaporating water. As anticipated, β in Miami is near the bottom of the observed daytime range (1.37 – 2.87) of

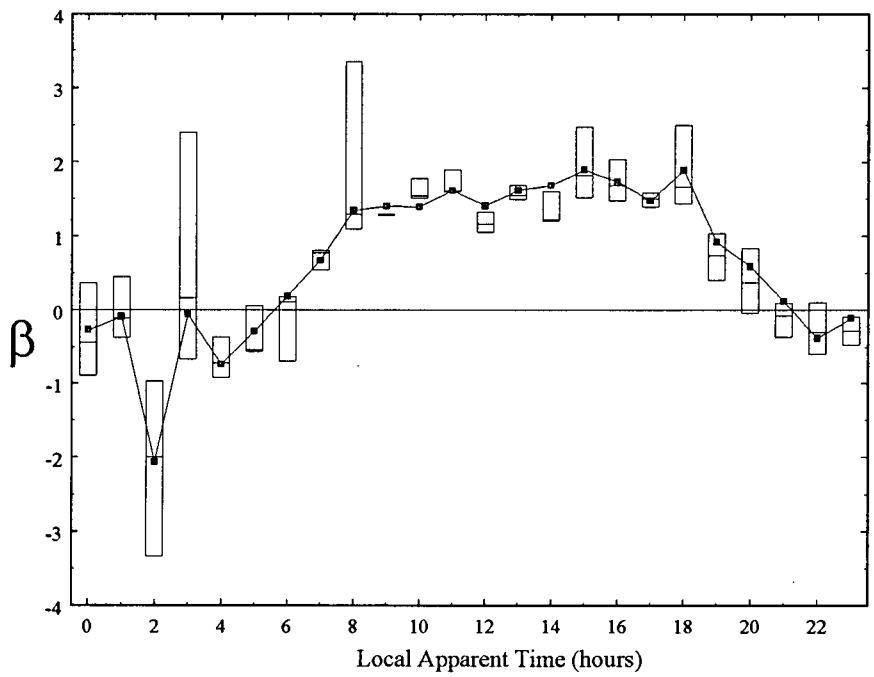

Fig. 4.3 Ensemble hourly averages of the Bowen ratio (β) over the entire observation period. The black squares are the averages of all data (the 0th through the 100th percentile) for each hour. In boxplots the top of each box corresponds to the 75th percentile of that hour's data; the horizontal line within is the median, and the bottom is the 25th percentile. At 0900 LAT the 'box' represents three data points, all of which are virtually identical.

suburban β for various cities (Grimmond and Oke 1999a).

Because Q_H and Q_E have such small absolute values at night, β can behave erratically, thus no significance is attached to the downspike at 0200 LAT (Fig. 4.3). Q_E is positive at all hours, hence the times in the morning and evening at which β changes sign correspond to when Q_H changes sign. Nocturnal β in Miami is less negative than in other cities, where it has been observed to be approximately – 1 (Grimmond and Oke 1995). This

suggests that at night, Miami's surface transfers less heat to the atmosphere, or that the nocturnal evaporation rate is higher than elsewhere.

Observed hourly averages of α_{PT} are well within the range of those from other studies (Oke *et al.* 1999b). This suggests that the dependence of Q_E on A is similar in

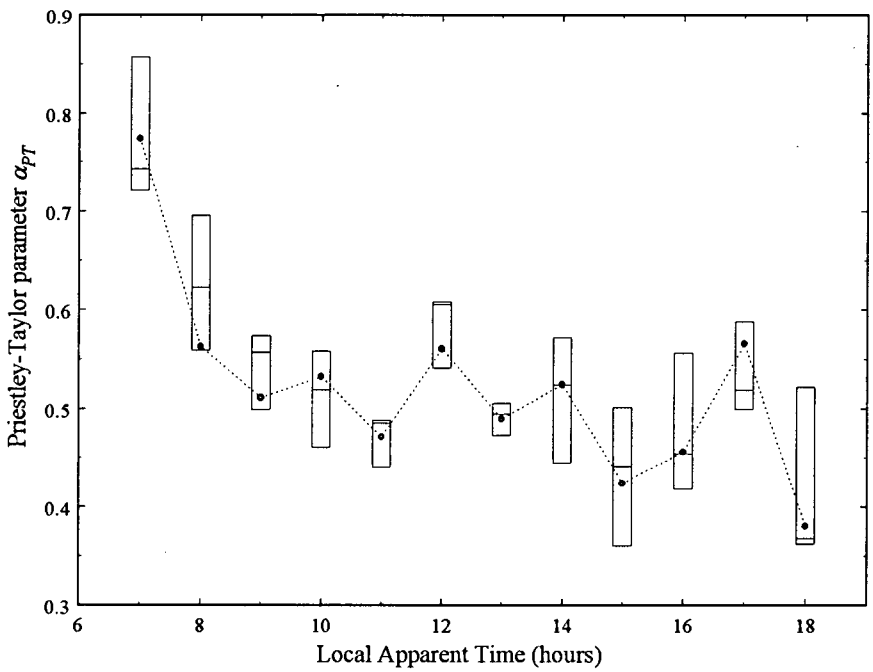

Fig. 4.4 Ensemble hourly averages of the Priestley-Taylor parameter α_{PT} during the entire observation period. In boxplots the top of each box corresponds to the 75th percentile of that hour's data; the horizontal line within is the median, and the bottom is the 25th percentile.

suburban areas located across a fairly wide range of climate zones. In many suburban and rural areas, α_{PT} tends to be reasonably constant during the middle ~ 6 hours of the day, with higher values towards sunrise and sunset. This is seen in the morning in Miami, but not in the evening, when in fact there may be a slight decrease (Fig.4.4). This evening decrease in α_{PT} appears to be due, at least in part, to a drop in Q_E that is disproportionately large, relative to the decrease in Q^* at that time, i.e. from 1700 to 1800 LAT, (Fig. 4.2). This is also illustrated by β, which has an anomalous increase at 1800 LAT (Fig. 4.3). The reason

for Q_E decreasing more rapidly than Q_H and Q^* may be an increase in stomatal resistance r_s, brought on by falling light levels in the evening. Earth – Sun geometry leads to a rapid setting of the sun and little twilight in regions in and near the tropics.

A second explanation for the drop in α_{PT} in the evening, and in particular at 1800 LAT, is the relatively high value of A at that time. This is not so much due to Q^* which is still positive, but to ΔQ_S, which is fairly large and negative (Fig. 4.11). Hence A (= Q^* – ΔQ_S) is fairly large and positive, leading to a low α_{PT}. It is unlikely that the evening decrease in $\bar{u}$ is the cause of the decrease in α_{PT} because there is no sudden decline in $\bar{u}$ at 1800; the decrease is roughly linear from 1600 to 2300 LAT (Fig. 2.8).

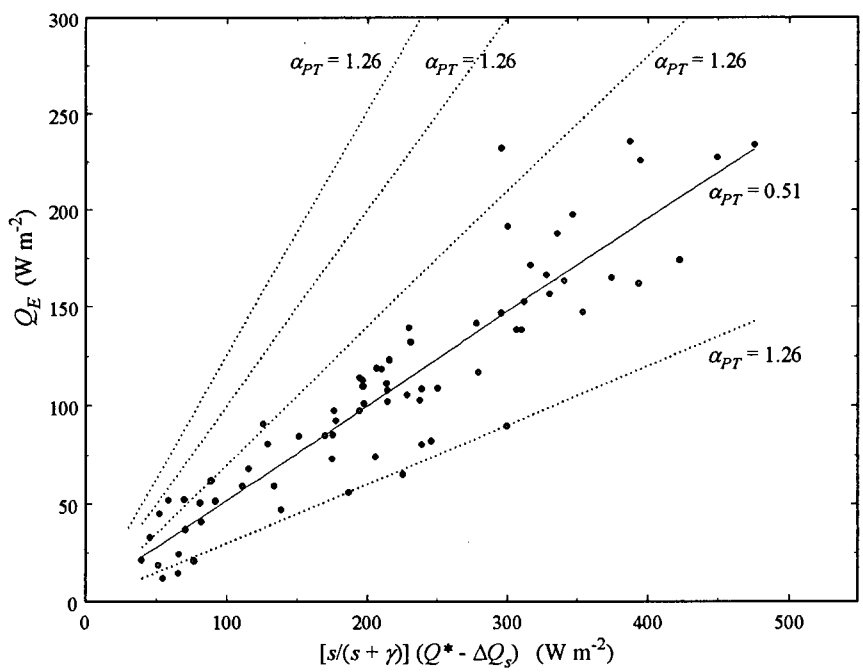

Fig. 4.5 Ensemble daytime ($Q^* > 0$ W m^{-2}) hourly averages of observed evaporation Q_E vs. the equilibrium evaporation Q_{Eq} during the entire observation period. The slope of the solid line is the average α_{PT} for these data, i.e. 0.51. For a variety of surface types with sufficient moisture, α_{PT} has been found to equal ~1.26 (McNaughton and Spriggs 1989).

Observed daytime α_{PT} values mostly lie in the range 0.3 to 0.7, with an average of

0.51 (Fig. 4.5). This is well below the value of ~1.26 observed for numerous different surfaces with sufficient moisture (McNaughton and Spriggs 1989). However, it is in the upper-middle portion of the observed urban range, which includes daytime averages as low as ~0.35, in Tucson and during a particularly dry summer without irrigation in Vancouver, and as high as 0.55, in Sacramento (Oke *et al.* 1999b). It is reasonable to expect that summertime Q_E would be greater in Miami than Sacramento, but Q_E may be somewhat stifled in Miami by the low vapour pressure deficit, and enhanced in Sacramento by oasis-edge effects, particularly around the perimeters of irrigated lawns and parks. Another factor contributing to its relatively large Q_E is Sacramento's high proportion of vegetated surfaces, compared to most cities (Grimmond and Oke 1999a). Although expectations were not supported by observations in Miami, the relation between the numerator and denominator

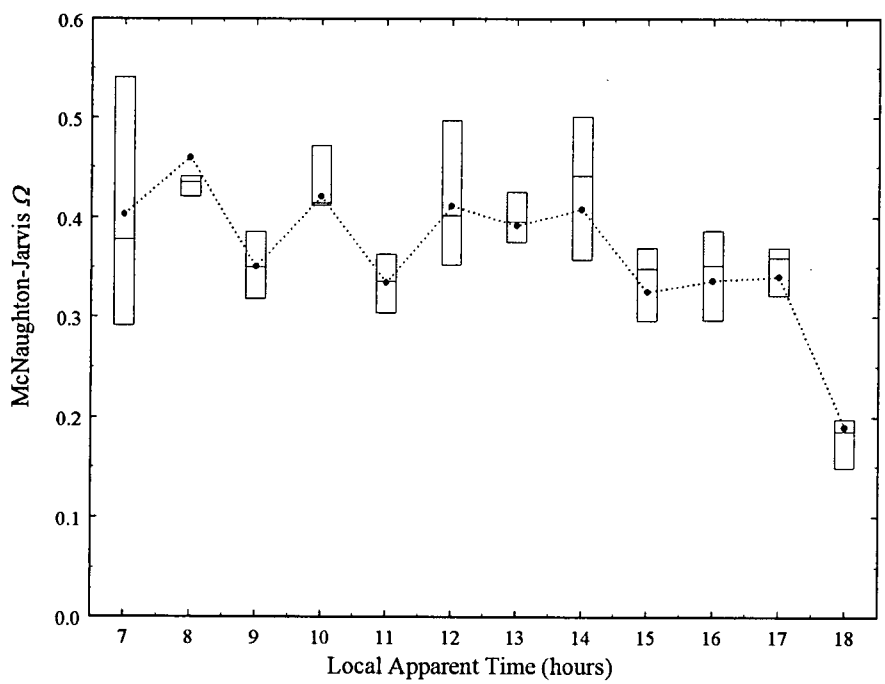

Fig. 4.6 Ensemble hourly averages of the McNaughton-Jarvis coupling parameter Ω, during the entire observation period. In boxplots the top of each box corresponds to the 75th percentile of that hour's data; the horizontal line within is the median, and the bottom is the 25th percentile.

of α_{PT} is reasonably linear (Fig. 4.5), indicating that fairly simple parameterizations may be appropriate there in the future.

In Miami, the daytime behaviour of Ω (Fig. 4.6) puts Miami at the more 'decoupled' end of the urban spectrum, but still much lower than low plant covers. The average daytime value in Miami is ~0.4, whereas previously published urban values of Ω include ~0.2 to 0.3 for Sacramento, ~0.1 to 0.2 for Vancouver, and ~0.1 for Tucson (Oke *et al.* 1999b). This relatively large average daytime Ω in Miami suggests that A is a more significant control on evaporation in Miami than in the other cities. It also suggests that Miami would be less responsive to variations of V than elsewhere, but this may simply be due to the fact that V is absolutely low compared to the others.

4.3. Analysis of Evaporation using the Penman-Monteith Combination Framework

4.3.1 Theory

Generally the Q_E fluxes observed in Miami are lower than expected, based on similar studies in other cities (Grimmond and Oke 1995 and 1999a). Therefore the Penman-Monteith version of the Combination Model was used to simulate the effect on Q_E of altering the vapour pressure deficit, in order to examine the possibility that evaporation was stifled by the high concentration of water vapour typically present in the near-surface air in Miami. The Penman-Monteith equation is:

$$Q_E = [\, s\,(Q^* - \Delta Q_S) + (\rho_a\, c_p\, V) / r_{aH} \,] / [\, s + \gamma\,(1 + r_c / r_{aH})\,] \qquad (\mathrm{W\ m^{-2}}), \qquad (4.7)$$

where ρ_a is the observed air density, and V is the observed vapour pressure deficit.

ρ_a is calculated in from observed T_a in K and P in Pa using (5.5) from Stull 1995:

$$\rho_a = P / (T_a \times R_d) \qquad (\mathrm{kg\ m^{-3}}) \qquad (4.8)$$

V is computed in Pa from observed T_a and relative humidity.

The aerodynamic resistance to the vertical transfer of heat r_{aH} required in (4.7) is calculated using $\bar{u}$ and u_* from the sonic anemometer. First, the aerodynamic resistance to the vertical transfer of momentum r_{aM} is calculated as

$$r_{aM} = \bar{u} \,/\, u_*^2 \qquad (\mathrm{s\ m^{-1}}), \tag{4.9}$$

where $\bar{u}$ is measured by the 3-D sonic anemometer on the 40 m tower, and u_* is observed directly by eddy correlation. Then r_{aH} is calculated using

$$r_{aH} = 2.32 \times r_{aM} \qquad (\mathrm{s\ m^{-1}}), \tag{4.10}$$

where 2.32 is derived from comparisons between r_{aM} and r_{aH} calculated by a log-profile approach. This involves computing r_{aM} and r_{aH} as functions of their roughness lengths, z_{oM} and z_{oH} respectively. In this section, it is assumed that $z_{oH} = 0.1 \times z_{oM}$, where $z_{oM} = 0.46$ m. The resistances are calculated as functions of $(\ln \{z'/z_o\})^2$, where z' is the tower height z_s (40.84 m) minus the zero-plane displacement height z_d (3.45 m). This gives the r_{aH}:r_{aM} ratio of 2.32, which holds under all stability conditions.

The final component of the Penman-Monteith equation to be discussed is r_c, by re-arranging it to read (e.g. Grimmond 1988):

$$r_c = [(s\beta/\gamma) - 1]\, r_{aH} + [(\rho_a\, c_p V)/(\gamma\, Q_E)] \qquad (\mathrm{s\ m^{-1}}), \tag{4.11}$$

Here the purpose is to explore the effect on Q_E of various values of V.

4.3.2 Analysis Results

The roles of several terms in the Penman-Monteith equation (4.7) are investigated:

V — According to the Penman-Monteith equation, if the vapour pressure deficit is reduced, then evaporation decreases. Q_E calculations suggest that dividing observed V by

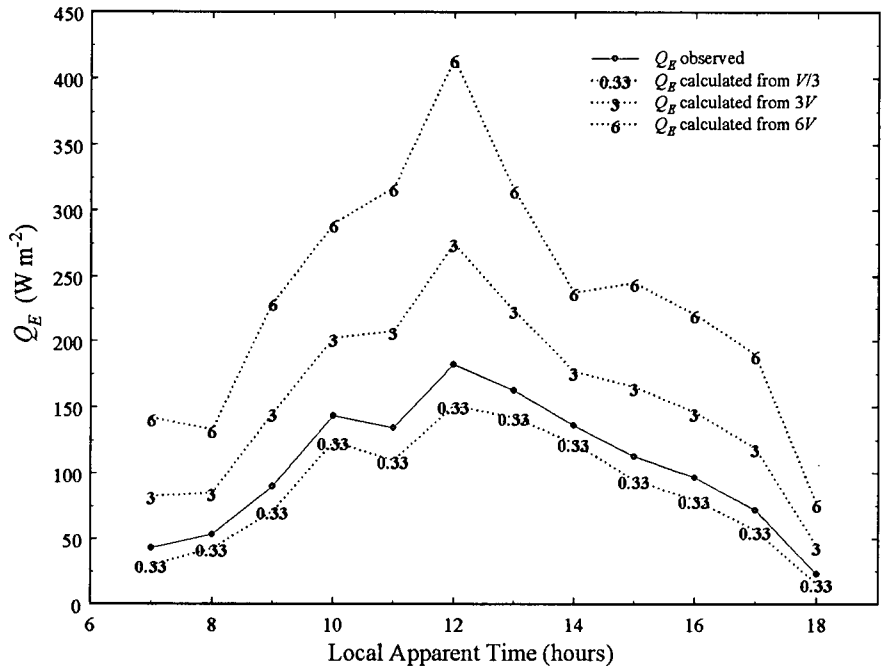

Fig. 4.7 Ensemble hourly averages of Q_E observed, and calculated using the Penman-Monteith equation with various multiples of the observed vapour pressure deficit (V).

three will cause a drop in the daytime mean evaporation of approximately 17 W m^{-2}, from that observed (Fig. 4.7). This decrease averages only about 20% of observed Q_E, because V in Miami is quite low to begin with, typically ranging from 7 to 14 mb (Fig. 2.8) during the daytime.

Grimmond and Oke (1995) observed V in Chicago, Los Angeles, Sacramento, and Tucson. Those measurements, as well as the present Miami observations (Fig. 2.8), show the same pattern of diurnal variation of V, with a minimum shortly before sunrise, a smooth unimodal curve during the day and evening, and a maximum in the late afternoon/early evening. By contrast, the absolute values of V in the five cities are very different from each other. Miami and Chicago have similar V values, with Los Angeles' about twice as large;

Sacramento's V is approximately triple that of Miami, and in Tucson it is roughly 6 times Miami's.

Q_E output from the Penman-Monteith equation using triple the observed vapour pressure deficit brings a noontime Q_E increase of 93 W m^{-2}, or 50% of the observed flux, and the average hourly increase is 52 W m^{-2}. With six times the observed V, the noontime Q_E is more than doubled, and the average hourly increase jumps to 130 W m^{-2} (Fig.4.7). Therefore it appears that in Miami, the absolute value of V is a significant control which suppresses Q_E, and that increases in V of the order of 30 to 40 mb (3000 to 4000 Pa) would bring significant increases in evaporation. This of course begs the question as to why Q_E in Chicago is so large. This probably focusses on Miami–Chicago differences of ΔQ_S, but because both are residuals this is unanswerable.

r_{aM} — Values of aerodynamic resistance to the vertical transfer of horizontal momentum are expected to be low in cities, in comparison with most rural or water surfaces, due to the large roughness. In Miami, values of r_{aM} are indeed low but vary considerably in the first half of the day (Fig. 4.8). Other suburban observations of r_{aM} are less variable (Oke *et al.* 1999b). They tend to start the daytime at about 30 to 40 s m^{-1}, and decrease to 20 – 30 s m^{-1} at midday. In the evening, some datasets show a decrease to approximately 10 s m^{-1}, some remain fairly constant at 20, and others increase to 40 s m^{-1} by nightfall. Given that surface roughness does not alter, these variations relate to the wind climate. In Miami, r_{aM} falls within the range observed elsewhere, with the exception of the peaks at 0800, 1000, and 1400 LAT. Overall the values are fairly consistent within a given hour.

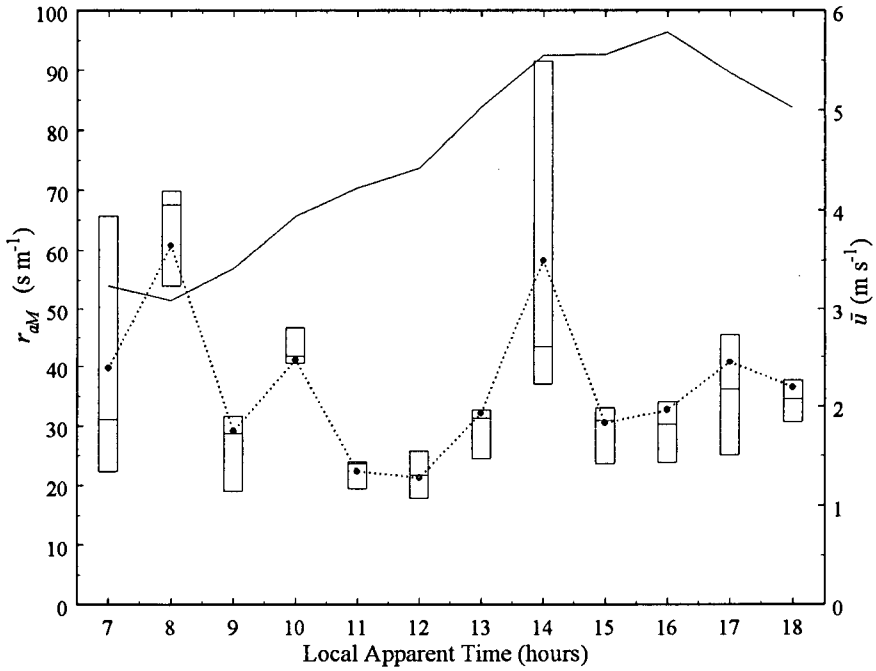

Fig. 4.8 Ensemble hourly averages of the aerodynamic resistance to vertical transfer of horizontal momentum r_{aM}, during the entire observation period. In boxplots the top of each box corresponds to the 75th percentile of that hour's data; the horizontal line within is the median, and the bottom is the 25th percentile. The solid line is the hourly average $\bar{u}$ from the 3-D sonic anemometer on the 40 m tower.

r_c — The canopy resistance to the vertical transfer of water vapour is a major control on evaporation. In natural systems it essentially expresses the physiologic control exerted by plant stomata. In a city this remains true, but the role of soil and construction materials as stores of water is also involved. Due to Miami's lush vegetation and numerous lakes and canals, it is reasonable to presume that water is readily available at the surface, and therefore that the resistance to its transport is relatively low by urban standards.

In Miami r_c tends to be about 500 s m^{-1} during the morning, 800 s m^{-1} in the evening, and jumps to ~1800 s m^{-1} at 1800 LAT (Fig. 4.9). These values are in the middle of the previously observed range of suburban values, and are similar to r_c observations from Vancouver (Oke *et al.* 1999b), rather than on the lower end as expected.

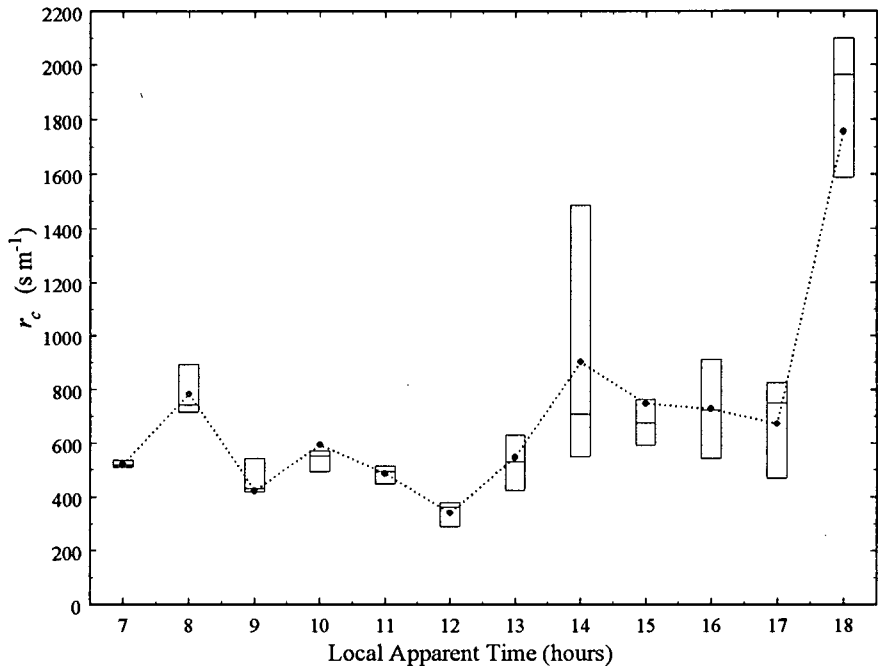

Fig. 4.9 Ensemble hourly averages of the canopy resistance to vertical transfer of water vapour r_c, calculated from the Penman-Monteith equation and observed Q_E, during the entire observation period. In boxplots the top of each box corresponds to the 75th percentile of that hour's data; the horizontal line within is the median, and the bottom is the 25th percentile.

Water may be less available than expected in Miami due to mitigation of r_c by the spatial averaging of wet and vegetated surfaces with impervious ones, such as roofs and roads, which when dry have extremely high r_c. Miami has a greater porportion of impervious surfaces than Chicago, Los Angeles, Sacramento, and Vancouver, and a smaller proportion than Tucson (Grimmond and Oke 1999a).

Another explanation is that the stomatal resistance of the vegetation is higher than anticipated. In order to test this possibility, leaf stomatal resistances (r_s) were measured using a portable porometer during the day and late night of June 14-5, 1995. Each datapoint but one represents an average of r_s measurements from 10 to 20 leaves, and a variety of trees and bushes at the site. The r_s observation at 2000 LAT is an average of measurements

from six leaves. The r_s values are surprisingly similar to the canopy resistances calculated for the same times (Fig. 4.10). An urban canopy resistance r_c must consist of a weighted average of r_s values due to the vegetative components plus the almost infinite resistances of dry built surfaces, hence r_c should be greater than the r_s of the local vegetation. Here there is one observation time, 2000 LAT, for which $r_s > r_c$, and at the other observation times, essentially $r_s = r_c$ (Fig. 4.10).

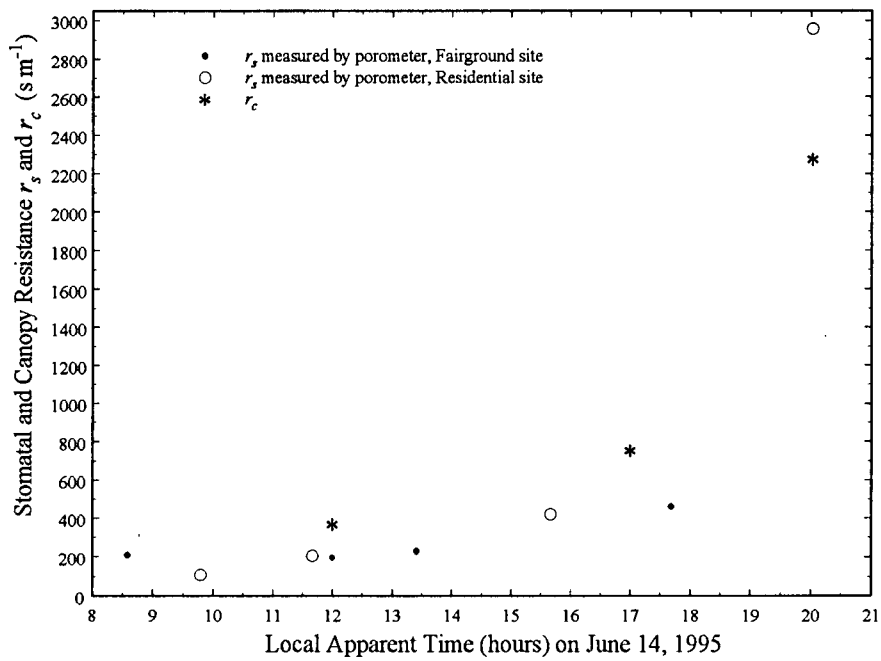

Fig. 4.10 Time series of hourly averages of leaf stomatal resistance to water vapour removal r_s, and canopy resistance to vertical transfer of water vapour r_c, during June 14, 1995, when winds were from the northwest. A notable exception to this are the points at 1200 LAT, which are from June 10, 1995, when winds were from the east-southeast. r_s was measured by porometer, and r_c is calculated using the Penman-Monteith equation, and measured Q_E.

The calculated r_c values for June 14 in Fig. 4.10 are normal for the site (e.g. compare with Fig. 4.9), despite the unusual synoptic conditions on this day. Skies were completely cloudless, which it was hoped would facilitate comparisons between the r_s measurements made in Miami, and those from other sites. However, the clear skies were

due to a cold front that passed over the area, causing winds to blow from the northwest, rather than from the southeast, the usual direction. For this reason the r_c values at 1700 and 2000 LAT in Fig. 4.10 are excluded from Fig. 4.9.

A further oddity of the June 14 data is that the source area for the turbulent fluxes was located in the 270° to 0° quadrant, which consists of slightly more dry (buildings and paved, i.e. impervious) surfaces and slightly fewer wet/moist (trees, grass, and water) surfaces than the preferred area (see Table 2.1). This alone would presumably cause evaporation to decrease. However, here the downmixing of cool, dry air associated with the cold front could have aided evaporation, thus counteracting the effect of the slightly drier source area. This would explain two facts which, given that synoptic conditions on June 14 were unusual, are surprising. The first is that the r_s values throughout the daytime on June 14 agree well with the 1200 LAT data point, which is from June 10 (Fig. 4.10). At that time, conditions were essentially typical; winds were from the east-southeast (i.e. 109°), with 25% of the sky hemisphere obscured by low cloud, and no mid-level or high cloud visible. The second is that the three r_c values in Fig. 4.10 are in close agreement with those in Fig. 4.9. Therefore in the final analysis, more data are needed, because due to synoptic conditions, the present observations are atypical, yet they are indistinguishable from measurements that qualify as typical.

4.4 Storage Heat Flux — ΔQ_S

The present 'measurements' of heat storage change are not direct because ΔQ_S is calculated as a residual from (1.3). Therefore errors in the measured Q_*, Q_H, and Q_E are collected in ΔQ_S, and values of the latter should be considered with that in mind.

The absolute values and diurnal behaviour of ΔQ_s in Miami (Fig. 4.11) are similar to those observed in other cities, and nearly identical to those recorded in Tucson (Grimmond and Oke 1995). For both cities, ΔQ_s peaks at about 200 W m^{-2} shortly before solar noon, drops to its daily minimum around sunset, and recovers somewhat by midnight, remaining

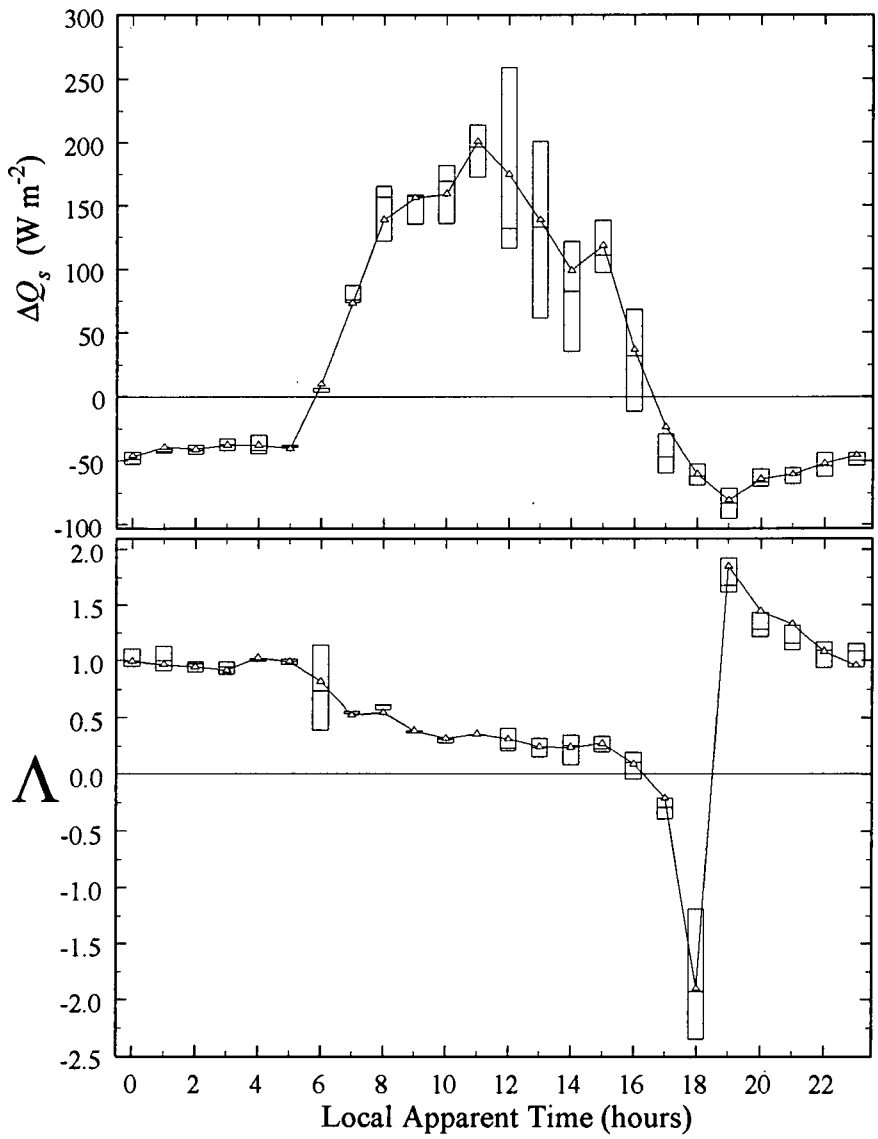

Fig. 4.11 Ensemble hourly averages of ΔQ_s and Λ ($\Delta Q_s/Q^*$) over the entire observation period. In boxplots the top of each box corresponds to the 75th percentile of that hour's data; the horizontal line within is the median, and the bottom is the 25th percentile. At 1100 LAT the 'box' represents three data points, all of which are virtually identical.

fairly constant until sunrise. The main differences between the ΔQ_S of the two cities are that the negative nocturnal values are larger in Tucson (–100 vs. –50 W m^{-2}), and the average daytime Λ is larger in Miami (0.30 vs. 0.23) (Grimmond and Oke 1999a).

The diurnal variation of Λ in Miami is essentially the same as that observed in suburban residential areas of Chicago, Los Angeles, Sacramento, and Tucson (Grimmond and Oke 1995). The steady daytime decrease from ~0.5 at sunrise to zero at sunset is present in those observations as well as the Miami measurements (Fig. 4.11), and is due to a hysteresis pattern between the radiative forcing and the storage change. The hysteresis pattern is particularly pronounced in Miami and Chicago, in comparison to other cities (Grimmond and Oke 1999a). Essentially this hysteresis is the mirror-image of that for Q_H (Fig. 4.1) and reflects the daily change in sensible heat sharing between conduction and convection.

At night, in Chicago, Sacramento, and Tucson, Λ is fairly constant at 1.0 as upwelling radiation is supplied primarily by removal of heat from storage. The same is largely true for Miami, although ΔQ_S is larger than Q^* for four hours after sunset, therefore a portion of the energy removed from storage during that time is partitioned into Q_E, and during the first two of those four hours, into Q_H. Similar post-sunset 'blips' are seen in the Λ plots for Chicago and Tucson, but those last for one hour, not four. Again the abrupt nature of sunset near the tropics may play a role.

The average daytime and all-day Λ in Miami, 0.30 and 0.18, respectively, are at the upper end of the observed suburban range (Grimmond and Oke 1999a). Only in Los Angeles (i.e. Arcadia) have slightly higher values been recorded: 0.31 for the daytime, and

0.21 for the all-day value. It is not particularly suprising that heat storage should play a large role in the energy regime of Miami, because the significant amounts of water present in the soil, vegetation, air, and canals and lakes facilitate efficient absorption of heat and provide a large heat capacity.

4.5 Parameterization Approaches

4.5.1 Bulk Aerodynamic Approach

Q_H is calculated from the following aerodynamic relation (Oke 1987):

$$Q_H = C_a\, k^2\, \bar{u}\, (T_o - T_a)\, (\Phi_M \Phi_H)^{-1} / (\ln \{ z'/z_{oH} \})^2 \qquad (\mathrm{W\ m^{-2}}), \qquad (4.12)$$

where C_a is the heat capacity of air (1200 J m^{-3} K^{-1}); T_o is the surface temperature. In this study T_o is approximated by T_{orad} calculated from the downward-facing pyrgeometer ($L\uparrow$), and T_a is the air temperature at the top of the Fairground tower. Φ_M is the dimensionless stability function to account for curvature of the logarithmic wind profile due to buoyancy effects, and Φ_H is the dimensionless stability function for heat. These functions are calculated using

$$(\Phi_M \Phi_H)^{-1} = (1 - 5\ \mathrm{Ri})^2 \qquad (4.13)$$

for the stable case (Ri positive), and

$$(\Phi_M \Phi_H)^{-1} = (1 - 16\ \mathrm{Ri})^{3/4} \qquad (4.14)$$

for the unstable case (Ri negative). Ri is assumed to equal z'/L. It is commonly thought that z_{oH} is much smaller than z_{oM} because of the excess resistance that heat encounters as it diffuses across the boundary layer without pressure effects, and/or the differing heat source and momentum sink locations (Verhoef *et al.* 1997). Thus z_{oH} is calculated using

$$z_{oH} = z_{oM} / \exp \{\mathrm{kB}^{-1}\}, \qquad (4.15)$$

where the range of kB^{-1} values used follows the suggestions of Voogt and Grimmond (1998).

The degree of agreement between observations in Miami and the output from the formula is relatively poor (Fig. 4.12). The erratic behaviour of the calculated Q_H from

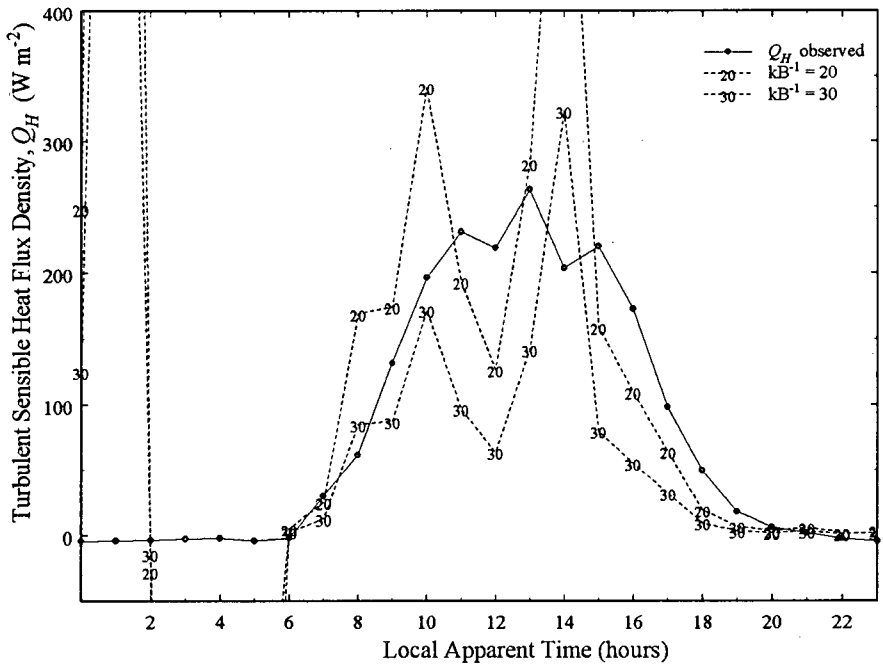

Fig. 4.12 Ensemble hourly averages of Q_H modelled and observed, under all-sky conditions. The plots of modelled Q_H use an ε_o of 0.95 to extract T_o from $L\uparrow$, and have been adjusted to account for stability. Each point is an average of about 5 hours of data.

midnight to 0600 LAT might be dismissed as a result of small fluxes giving rise to large percentage errors, or in some other manner producing perturbations in the equation output, but the pre-midnight values are in agreement with observed Q_H. In fact, a kB^{-1} of 15 produces acceptable results from 1500 to 2300 LAT. It appears that a kB^{-1} of about 25 would work well from 0600 to 1000 inclusive. kB^{-1} has been observed to vary diurnally in other studies (Verhoef *et al.* 1997), but in the present study during the middle of the day, from 1100 to 1400 LAT, the equation simply fails to reproduce the observed Q_H variations.

A kB^{-1} of 25 concurs with other suggested urban values and ranges, despite the fact that some of those studies used infrared thermometers, rather than pyrgeometers, to measure T_o (J. A. Voogt, *pers. comm.* 1999; Voogt and Oke 1997).

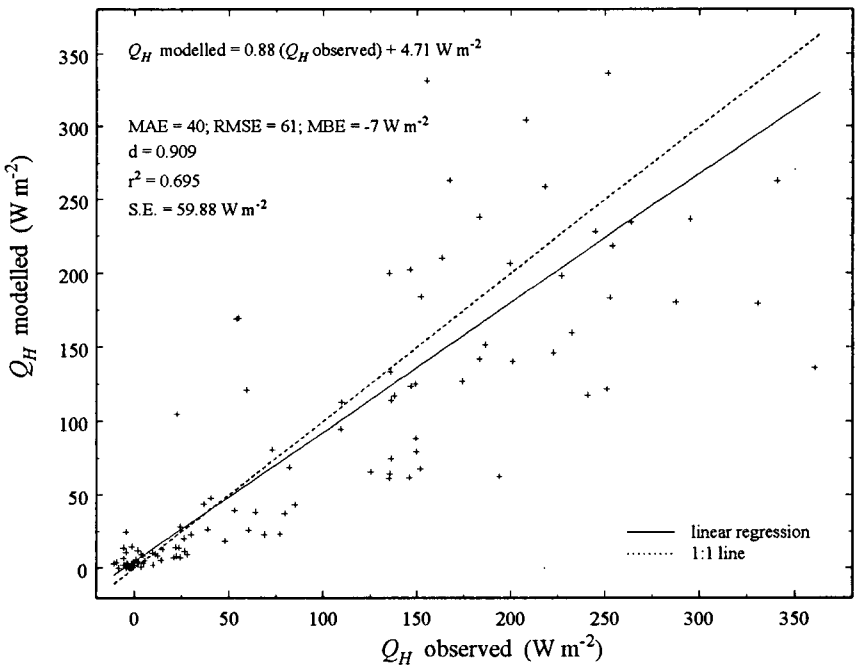

Fig. 4.13 Scatterplot with linear regression of hourly averages of Q_H parameterized using (4.1), with a kB^{-1} of 17.5, against Q_H observations. These are the same data as in Fig. 4.13, except that all hourly averages from 0000 to 0500 LAT, inclusive, are excluded. Also, seven daytime hourly averages are excluded because the calculated Q_H was larger than the observed Q^*; these seven points did not fall during twilight hours, were non-consecutive, and are from six different days.

In addition to confirming that (4.12) does not work well with these data, Fig. 4.13 indicates that 17.5 is appropriate as an average daily kB^{-1}. This value was determined iteratively to give the lowest Willmott statistics. A kB^{-1} of 25 produces significantly higher errors, and a lower d, in the Willmott statistics, but gives a standard error of only 33 W m^{-2}, and the same r^2 (0.695). However, on the strength of the better Willmott statistics, and the fact that the regression line is reasonably close to the 1:1 line (Fig. 4.13), 17.5 is probably better in the daily mean for this dataset. Errors of the estimated Q_H are on the order of 60

W m^{-2}, which is similar to the standard deviation of observed Q_H. Therefore the equation can provide a reasonable order-of-magnitude estimate of hourly Q_H. This is largely counterbalanced, however, by the failure of the calculated flux to track the observed hourly variation in the ensemble average, especially in the middle of the day.

A possible reason for the discrepancies between observed and calculated Q_H is the difference between the source areas of the radiative and turbulent fluxes. Turbulent flux source areas change with wind speed and direction, whereas the radiative source area is the same throughout the study period. Moreover, a disproportionately small fraction of the down-facing pyrgeometer's field of view is occupied by vertical elements, primarily walls. Walls affect turbulent heat fluxes significantly, but their effect on upwelling radiative fluxes can be slight, depending on the location and field of view of the radiometer.

Another possible explanation for the disappointing performance of the formula is that the surface temperature should be the surface aerodynamic temperature, $T_{o\ aero}$, not the surface radiative temperature (i.e. $T_{o\ rad}$). Differences between $T_{o\ rad}$ and $T_{o\ aero}$ are important because Q_H is sensitive to even small errors in the difference $T_{o\ aero} - T_a$ (Voogt and Oke 1997). Furthermore, the T_o used here may contain errors, especially in the middle of the day. This is because the pyrgeometer used lacks a thermistor to measure the temperature of the dome. This is now deemed useful since the silicon coating of the dome makes it susceptible to solar heating.

4.5.2 Simplified Penman-Monteith Approach

A simplified version of the Penman-Monteith approach (4.7) to surface energy flux parameterization is put forth by De Bruin and Holtslag (1982), and reviewed by Holtslag

and Van Ulden (1983). It was suggested for use in urban areas by Hanna and Chang (1992). It requires inputs of near-surface air temperature (T_a), net all-wave radiation (Q^*), and storage heat flux (ΔQ_S in urban areas). Two empirical parameters are also required. One is the Penman-Monteith surface moisture availability factor (α_{PM}), which accounts for the (strong) correlation of Q_H and Q_E with ($Q^* - \Delta Q_S$) and depends on surface moisture availability. (The difference between α_{PM} and α_{PT} is discussed in Appendix 2.) The other is β_{PM}, which accounts for the uncorrelated part. This parameterization provides daytime estimates of Q_H and Q_E, using the following equations:

$$Q_H = [(1 - \alpha_{PM} + S) / (1 + S)] (Q^* - \Delta Q_S) - \beta_{PM} \qquad (\mathrm{W\ m^{-2}}) \qquad (4.16)$$

$$Q_E = [\alpha_{PM} / (1 + S)] (Q^* - \Delta Q_S) + \beta_{PM} \qquad (\mathrm{W\ m^{-2}}), \qquad (4.17)$$

where S is defined by $c_p/(L_e \partial q_s/\partial T)$; c_p is the specific heat of air at constant pressure (1004.67 J kg^{-1} K^{-1}), L_e is the latent heat of vaporization of water, which is temperature-dependent, and $\partial q_s/\partial T$ is calculated using (4.2). S and L_e vary with temperature (i.e. T_a at a height of 2 m) as follows:

T **(°C)**	-5	0	5	10	15	20	25	30	35
S	2.01	1.44	1.05	0.79	0.60	0.45	0.35	0.27	0.21
L $_e$ (MJ kg^{-1})	2.513	2.501	2.488	2.476	2.464	2.453	2.442	2.432	2.422

Table 4.1. Variation of S and L_e with temperature.

The observed energy budget in Miami is used to solve for the surface moisture parameters α_{PM} and β_{PM} by linear regression of Q_H and Q_E against the available energy A, = (Q^* – ΔQ_S). This was done for two sets of conditions: daytime all-sky conditions and all-time all-sky conditions (Fig. 4.14). The formulae, (4.16) and (4.17), were devised for daytime all-sky use, but

in fact, alternating between daytime and all-time data produces relatively minor changes in suburban α_{PM} and β_{PM}.

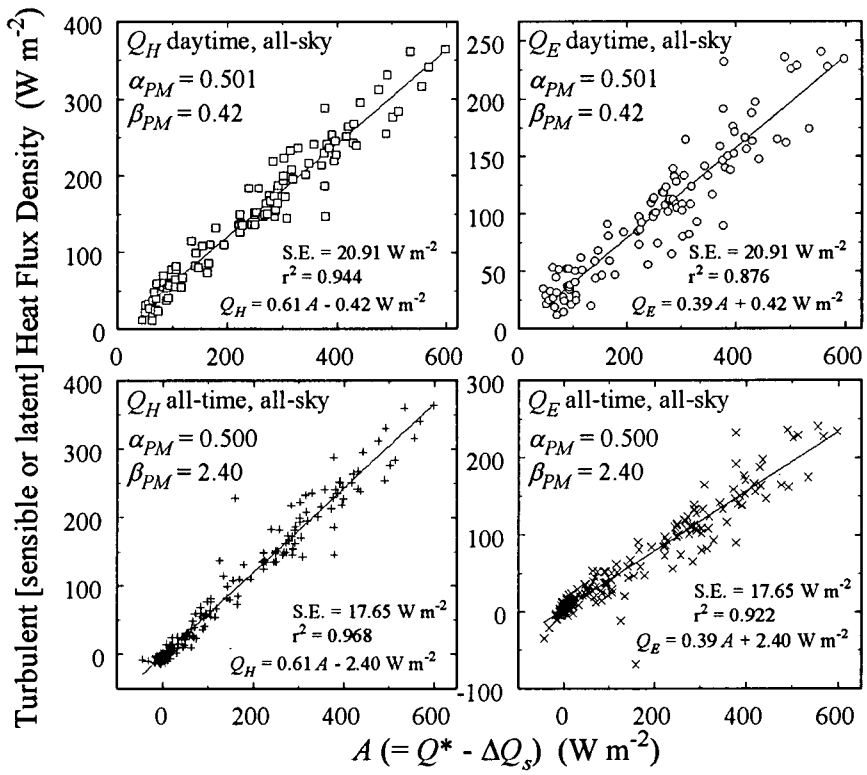

Fig. 4.14 Scatterplot with linear regression of hourly averages of Miami's Q_H and Q_E vs. available energy A. The y-intercepts are equal to $-\beta_{PM}$ and β_{PM} respectively, and S is used to extract α_{PM} from the slope coefficients.

Hanna and Chang (1992) propose ranges of α_{PM} values for various types of sites: for a dry desert, 0.0 – 0.2; for arid rural areas, 0.2 – 0.4; for moderately dry crops, 0.4 – 0.6; for cities, 0.5 – 1.0; for crops and forests with moist soils, 0.8 – 1.2; and for large water bodies, with land more than 10 km distant, 1.2 – 1.4. Newton (1995) used the above method on a dataset collected during the summer of 1991 in Sacramento, California and found a suburban α_{PM} of 0.52. Except for garden irrigation Sacramento is a dry city, particularly in summertime, and as would be expected, the α_{PM} value is at the dry end of the suggested urban range. Thus in Miami,

α_{PM} might be anticipated to be closer to 1.0, but this is not found (Fig. 4.14).

The suburban α_{PM} values in Table 4.2, all of which are at or slightly above 0.5, imply that the similarities in suburban surface morphology between Miami and Sacramento outweigh the climatological differences in terms of their impact on surface energy partitioning and moisture availability. This raises the question: what is the basis for the suggested urban range of 0.5 to 1.0 given by Hanna and Chang (1992)? The present observations together with those from Sacramento suggest that an α_{PM} of approximately 0.5 may apply to suburban sites across a range of different climatic regions.

Rural / Suburban site, conditions	α_{PM}	β_{PM} (W m^{-2})	β'_{PM} (W m^{-2})
rural Cabauw, Netherlands, daytime all-sky (wet)	1	20	20
rural Sacramento, all-time all-sky (wet)	1.20	14.9	12.4
rural Sacramento, daytime all-sky (wet)	**1.08**	**22.8**	**21.2**
rural Sacramento, all-time all-sky (dry)	0.52	-49.4	-94.1
rural Sacramento, daytime all-sky (dry)	0.01	8.0	785.1
suburban Sacramento, all-time all-sky	0.55	6.3	11.4
suburban Sacramento, daytime all-sky	**0.52**	**11.2**	**21.4**
suburban Miami, all-time all-sky	0.50	2.4	4.8
suburban Miami, daytime all-sky	**0.50**	**0.4**	**0.8**

Table 4.2. Calculated values of Penman-Monteith surface moisture availability parameters for rural and suburban sites. Values in **boldface** are considered preferable; see text for explanation.

The first published estimate of β_{PM} was 20 W m^{-2}, made in a study at the moist vegetated Cabauw site in the Netherlands, where $\alpha_{PM} \sim 1$ (De Bruin and Holtslag 1982). In that study it was suggested that the variable β_{PM} be replaced with the product of the constant β'_{PM} and the variable α_{PM}:

$$\beta_{PM} = \beta'_{PM}\, \alpha_{PM} \qquad (\mathrm{W\ m^{-2}}), \tag{4.18}$$

where β'_{PM} = 20 W m^{-2}. Results from Newton (1995) found β'_{PM} = 21.2 W m^{-2} for a moist

vegetated surface, using measurements made at an irrigated grass site in Sacramento under all-sky conditions. β'_{PM} in Miami is calculated to be 0.8 W m^{-2} under daytime all-sky conditions (Table 4.2). The daytime all-sky β'_{PM} is preferred for all sites because those are the conditions for which the scheme is intended. The β_{PM} and β'_{PM} values in Table 4.2 cover a fairly wide range. A switch from all-time to daytime data in Sacramento brings a decrease in α_{PM}, and increases in both β_{PM} and β'_{PM}, whereas in Miami α_{PM} remains unchanged, and the two β values decrease.

Despite the proposal to replace β_{PM} as shown in (4.18), it is worth examining this term because it lends itself well to discussions of diurnal flux behaviour, accounting as it does for the observation that in the evening, Q_H generally tends to become negative before sunset. This characteristic may be different at urbanized sites, indeed at heavily-developed sites Q_H may not turn negative until well after sunset. Of the two values calculated in the present study (Fig. 4.14), the daytime β_{PM} of 0.4 W m^{-2} is favoured because, as stated above, those are the intended conditions for use of (4.16) and (4.17). This β_{PM} for Miami is lower than that calculated for a suburban site in Sacramento, implying that in the evening, Q_H remains positive longer in Miami than in Sacramento, possibly because of the larger releases of ΔQ_S which should tend to keep Miami's surface warm longer. ΔQ_S is larger in Miami than in Sacramento, both in absolute terms (i.e. in MJ m^{-2} d^{-1}), and when normalized by Q^* (i.e. Λ).

Agreement between observed Q_H and Q_E, and the same fluxes calculated using (4.16) and (4.17) is good (Fig. 4.15), but this is to be expected since these calculations are made from observed Q^* and 'observed' (i.e. calculated as a residual) ΔQ_S, and using α_{PM}

and β_{PM} values derived from observed Q_H and Q_E. Therefore the purpose here is not to evaluate the equations as a way of calculating Q_H and Q_E in the absence of specialized observations, but rather to assess their ability to relate the turbulent heat fluxes to (Q^* – ΔQ_S). This relation appears to be captured relatively effectively by the equations, particularly in the all-time (i.e. both day and night) case, when errors are below 20 W m^{-2}, despite the fact that, as mentioned above, the equations are intended for use with daytime data only.

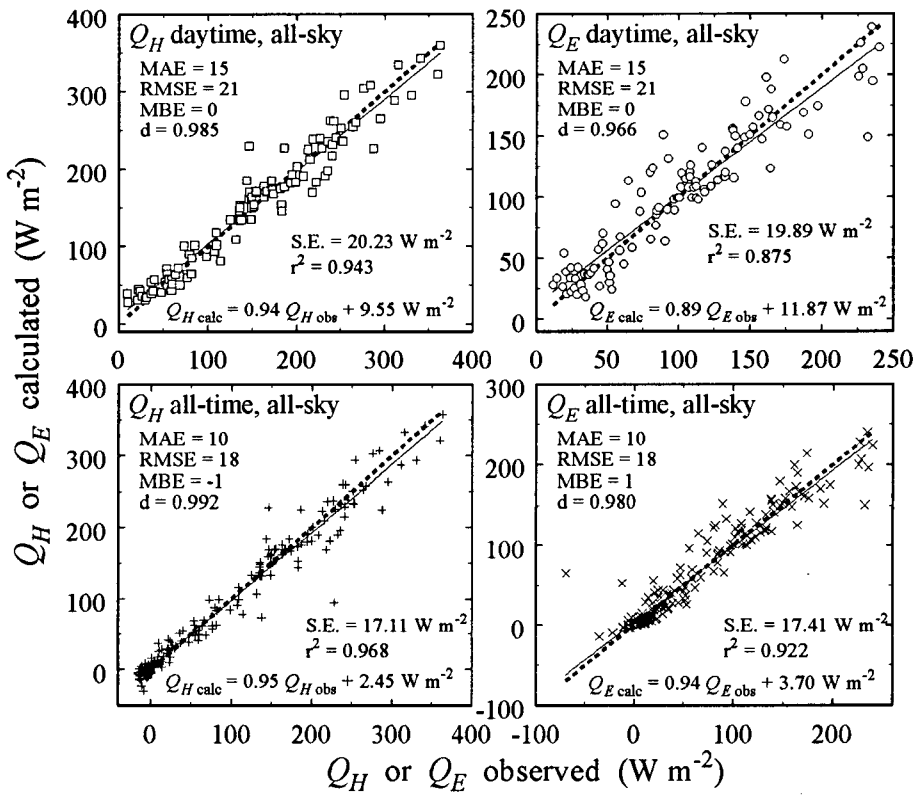

Fig. 4.15 Scatterplot with linear regression of hourly averages of Q_H and Q_E calculated using (4.5) and (4.6) vs. the observed fluxes.

The statistics improve from the daytime to the all-time situations (Fig. 4.15), but this is due in part to the increasing size of the datasets, and the small absolute values of the

nocturnal fluxes. More meaningful is the fact that the d and r^2 values indicate that estimation of Q_H is slightly better than that of Q_E, although in the daytime case, the standard error is slightly higher for Q_H. The Willmott statistics, excluding d, are identical in each case (with a change in the sign of the MBE) for Q_H and Q_E, which is a mathematical occurrence arising from the fact that ΔQ_S is calculated as a residual from Q^*, Q_H, and Q_E. The calculated turbulent heat fluxes are thus linked by their use of the same observed Q^* and calculated ΔQ_S, in addition to their sharing values of S, α_{PM}, and β_{PM}.

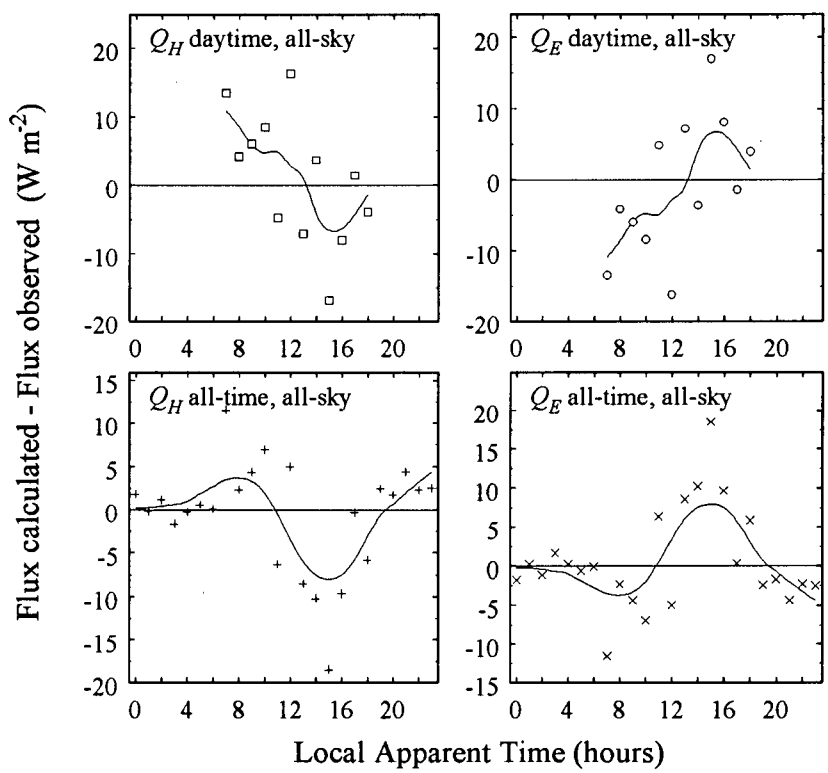

Fig. 4.16 Ensemble hourly averages of calculated minus observed Q_H and Q_E under the conditions indicated on each graph. The line on each plot uses weighted least squares.

Another function of the mathematic link between the calculated Q_H and Q_E can be seen in plots of the calculated minus observed fluxes (Fig. 4.16). In both cases, the Q_E plot is the same as the Q_H plot flipped vertically. The daytime portions of the all-time plots are

different from the daytime all-sky plots because different α_{PM} and β_{PM} values were used for the two scenarios, as noted in Table 4.2.

For this dataset, prediction of Q_H and Q_E is better in the all-time case than in the daytime (Figs 4.15, 4.16), but the equations are meant for daytime use, so the daytime α_{PM} and β_{PM} are presumed to be preferable to the others. However, as Fig. 4.16 shows, the all-time α_{PM} and β_{PM} produce as good or better Q_H and Q_E estimates than the daytime values, implying that the equations are equally applicable at night and during the day. Further encouragement for expanded use of (4.16) and (4.17) is given by the regularity of the all-time modelled – observed plot, which follows a sinusoidal pattern (Fig. 4.16). Evidently an empirical function could readily be applied to the equations to counteract this 'error' pattern.

4.6 Conclusions

The chief points made in this chapter are:

- measurements of Q_H, χ, Q_E, Υ, ΔQ_S, and Λ in Miami are reasonably similar to observations in similar residential districts of other North American cities, and χ and Υ show remarkably little variability in the daytime, suggesting a robust basis for parameterization
- the expectation that Q_E would be large relative to other cities was not observed, in part because Q^* is not appreciably larger than in other cities, but also because Q_E is stifled by the small vapour pressure deficit in Miami, and the larger than normal amount of heat storage

- the Bowen ratio $\beta \sim 1.5$ in Miami, which as expected is near the bottom of the range of observed daytime values in suburban areas
- Miami, along with Los Angeles, has the highest recorded suburban Λ values; a characteristic feature of Miami's ΔQ_s regime is prolonged removal of heat from storage during the near-sunset hours, which may be an effect of the abrupt nature of sunset near the tropics
- in Miami on average the Priestley-Taylor aridity parameter $\alpha_{PT} \sim 0.51$, and the Penman-Monteith moisture parameter $\alpha_{PM} \sim 0.50$; observations from Sacramento also suggest suburban $\alpha_{PT} \sim \alpha_{PM} \sim 0.5$
- the second Penman-Monteith parameter, β_{PM}, is 0.4 W m^{-2} in Miami, and 11.2 W m^{-2} in Sacramento
- in Miami the average daytime McNaughton-Jarvis coupling factor ($\Omega \sim 0.4$) is at the upper end of the observed suburban range, which suggests that in Miami, A is a more significant control on evaporation than in other cities
- the observed r_{aM} and r_c in Miami fall within the ranges observed in other suburban areas
- kB^{-1}, a parameter that relates z_{oH} to z_{oM}, is found to be approximately 17.5 in the daily mean

CHAPTER 5. SUMMARY

5.1 Radiation Budget

In chapter 3, which deals with radiative energy fluxes, the following conclusions are made:

- if $K\downarrow$ observations are to be used as part of a measured or parameterized site budget, it is important that the $K\downarrow$ site not be far distant because of spatial variation of $K\downarrow$ under patchy cloud conditions
- observations suggest that $K\downarrow$ in west Miami is slightly lower in the morning than at corresponding solar times in the afternoon due to decreased transmissivity through the urban plume
- urban surface geometry, like that of forests, tends to mitigate the midday peak in surface temperature, resulting in $L\uparrow$ plots that are flattened and essentially in phase with $K\downarrow$
- the surface albedo, averaged over clear and all-sky conditions, is observed to be 0.166, and ε_o is estimated to be 0.97 in suburban Miami
- under clear sky conditions, and without applying any corrections, reasonable estimates of $L\downarrow$ are provided by 5 of the 6 formulae used, with the Idso '81 equation producing the poorest results. Under clear skies, with a correction for systematic diurnal under- and over-estimation, the dual-input (T_a, e_a) $L\downarrow$ equations consistently outperform the single-input (T_a) equations
- under all-sky conditions, using the Bolz cloud relation, $L\downarrow$ estimation by the formulae is worse than under clear skies, but with errors on the order of 5% from 5 of the 6

equations used, results are still useful. Again the Idso '81 equation appears to be an unusually poor performer, with errors roughly twice as large as the others

- under all-sky conditions a slight modification to the Bolz cloud relation produces improved $L\downarrow$ estimates from the dual-input equations, with approximately a 25% reduction of the errors obtained using the unmodified Bolz relation. Performance of the single-input equations is slightly worsened by the modification, thus in this case the dual-input equations are superior
- Q^* can be estimated satisfactorily from co-located observations of $K\downarrow$

5.2 Energy Balance Climatology

The focus in chapter 4 is on the measured sensible and latent turbulent heat fluxes (Q_H and Q_E, respectively) and heat storage (but ΔQ_S is not measured directly). The main observations made in chapter 4 are:

- measurements of Q_H, χ, Q_E, Υ, ΔQ_S, and Λ in Miami are reasonably similar to observations in similar residential districts of other North American cities, and χ and Υ show remarkably little variability in the daytime, suggesting a robust basis for parameterization
- the expectation that Q_E would be large relative to other cities was not observed, in part because Q^* is not appreciably larger than in other cities, but also because Q_E is stifled by the small vapour pressure deficit in Miami, and the larger than normal amount of heat storage
- the Bowen ratio $\beta \sim 1.5$ in Miami, which as expected is near the bottom of the range of observed daytime values in suburban areas

- Miami, along with Los Angeles, has the highest recorded suburban Λ values; a characteristic feature of Miami's ΔQ_S regime is prolonged removal of heat from storage during the near-sunset hours, which may be an effect of the abrupt nature of sunset near the tropics
- in Miami on average the Priestley-Taylor aridity parameter $\alpha_{PT} \sim 0.51$, and the Penman-Monteith moisture parameter $\alpha_{PM} \sim 0.50$; observations from Sacramento also suggest suburban $\alpha_{PT} \sim \alpha_{PM} \sim 0.5$
- the second Penman-Monteith parameter, β_{PM}, is 0.4 W m^{-2} in Miami, and 11.2 W m^{-2} in Sacramento
- in Miami the average daytime McNaughton-Jarvis coupling factor ($\Omega \sim 0.4$) is at the upper end of the observed suburban range, which suggests that in Miami, A is a more significant control on evaporation than in other cities
- the observed r_{aM} and r_c in Miami fall within the ranges observed in other suburban areas
- kB^{-1}, a parameter that relates z_{oH} to z_{oM}, is found to be approximately 17.5 in the daily mean

LIST OF SYMBOLS AND ABBREVIATIONS

Some symbols are relevant for one equation and are not listed here

A	available energy at the surface (= $Q^* - \Delta Q_S$)
BL	atmospheric boundary layer
C_a	heat capacity of air, (= 1200 J m^{-3} K^{-1})
c_p	specific heat of air at constant pressure, (= 1004.67 J kg^{-1} K^{-1})
d	Willmott agreement factor
D	horizontal spacing of surface roughness elements (m)
e_a	near-surface water vapour pressure (mb, hPa)
e_s	saturation pressure of water vapour (mb, hPa)
FSAM	flux source area model
ITCZ	inter-tropical convergence zone
K^*	net shortwave radiation (W m^{-2})
$K\downarrow$	incoming shortwave radiation (W m^{-2})
$K\uparrow$	reflected shortwave radiation (W m^{-2})
kB^{-1}	$\equiv \ln \{z_{oM}/z_{oH}\}$
K_H	turbulent diffusivity of heat (m^2 s^{-1})
K_V	turbulent diffusivity of water vapour (m^2 s^{-1})
L	Obukhov length; length scale (m)
L^*	net longwave radiation (W m^{-2})
$L\downarrow$	downwelling longwave radiation (W m^{-2})
$L\uparrow$	upwelling longwave radiation (W m^{-2})

LAT local apparent time

L_e latent heat of vaporization of water (J kg^{-1})

MAE mean absolute error

MBE mean bias error

N fractional cloud cover

OHM objective hysteresis model

P atmospheric pressure (mb)

PBL planetary boundary layer

q' instantaneous deviation from the mean specific humidity (g kg^{-1})

Q^* net all-wave radiation flux density (W m^{-2})

ΔQ_A net heat advection (W m^{-2})

Q_E turbulent latent heat flux density (W m^{-2})

Q_{Eq} equilibrium evaporation (W m^{-2})

Q_F anthropogenic heat flux density (W m^{-2})

Q_G ground heat flux density (W m^{-2})

Q_H turbulent sensible heat flux density (W m^{-2})

ΔQ_S storage heat flux (W m^{-2})

q_s saturation specific humidity (g [water vapour] g^{-1} [air])

$\partial q_s/\partial T$ slope of the saturation vapour pressure (or specific humidity) vs. temperature curve (Pa K^{-1}, g [water vapour] g^{-1} [air] K^{-1})

r_{aH} aerodynamic resistance to the vertical transfer of heat (s m^{-1})

r_{aM} aerodynamic resistance to the vertical transfer of momentum (s m^{-1})

r_c surface or canopy resistance to the vertical transfer of water vapour (s m^{-1})

R_d gas constant for dry air, (= 287 J kg^{-1} K^{-1})

RH relative humidity (%)

Ri Richardson's Number

RMSE root mean squared error

r_s leaf stomatal resistance to water vapour transfer (s m^{-1})

R_v gas constant for water vapour, (= 461 J kg^{-1} K^{-1})

S $\equiv c_p/(L_e \partial q_s/\partial T)$

s $\equiv \partial q_s/\partial T$ (Pa K^{-1}, g [water vapour] g^{-1} [air] K^{-1})

S.E. standard error

T' instantaneous deviation from the mean air temperature (°C)

T_a air temperature (°C)

T_o surface temperature (°C)

u' instantaneous deviation from the mean horizontal (x-plane) wind speed (m s^{-1})

$\bar{u}$ mean horizontal (x-plane) wind speed (m s^{-1})

u_* friction velocity (m s^{-1})

UBL urban boundary layer

UCL urban canopy layer

v' instantaneous deviation from the mean horizontal (y-plane) wind speed (m s^{-1})

V vapour pressure deficit (Pa)

w' instantaneous deviation from the mean vertical wind speed (m s^{-1})

YD day of the year

z'	effective measurement height, $= z_s - z_d$ (m)
z^*	blending height (m)
z_d	zero-plane displacement (m)
z_o	roughness length (m)
z_{oH}	roughness length for heat (m)
z_{oM}	roughness length for momentum (m)
z_s	sensor height (m)
α	surface albedo
α_{PM}	Penman-Monteith surface moisture availability factor
α_{PT}	Priestley-Taylor evaporation coefficient
β	Bowen ratio ($= Q_H/Q_E$)
β_{PM}	Penman-Monteith correlation parameter (W m^{-2})
β'_{PM}	alternate Penman-Monteith correlation parameter (W m^{-2})
γ	psychrometric 'constant' $= c_p/L_e$ (Pa K^{-1})
ε_a	atmospheric emissivity
ε_o	surface emissivity
Λ	storage heat flux normalized by net radiation, $\Delta Q_s/Q^*$
ρ_a	observed air density (kg m^{-3})
ρ_{as}	the saturation density of air (kg m^{-3})
ρ_v	the saturation density of water vapour (kg m^{-3})
σ	Stefan-Boltzman constant (W m^{-2} K^{-4})
σ_v	standard deviation of lateral (y-plane) wind speed fluctuations (m s^{-1})

Υ latent heat flux normalized by net radiation, Q_E/Q^*

ϕ local solar elevation angle

Φ_H stability function for heat

Φ_M stability function for momentum exchange

χ sensible heat flux normalized by net radiation, Q_H/Q^*

Ω McNaughton-Jarvis coupling factor

REFERENCES

Adebayo, Y., 1990: Aspects of the variation of radiation budget in the urban canopy of Ibadan. *Atmos. Environ.*, **24B** (1), 9-17.

———, 1991: Day-time effects of urbanization on relative humidity and vapour pressure in a tropical city. *Theor. Appl. Climatol.*, **43**, 17-30.

Ahrens, C. D., 1991: *Meteorology Today: an Introduction to Weather, Climate, and the Environment*, fourth edition. St. Paul: West Publishing Company.

Aida, M., 1982: Urban albedo as a function of the urban structure – a model experiment. *Bound.-Layer Meteor.*, **23**, 405-414.

———, and K. Gotoh, 1982: Urban albedo as a function of the urban strucure – a two-dimensional numerical simulation. *Bound.-Layer Meteor.*, **23**, 415-424.

Arnfield, A. J., 1982: An approach to the estimation of the surface radiative properties and radiation budgets of cities. *Phys. Geog.*, **3**, 97-122.

Atwater, M. A., 1977: Urbanization and pollutant effects on the thermal structure in four climatic regimes. *J. Appl. Meteor.*, **16**, 888-895.

Berlyand, M. Ye., K. Ya. Kondratyev, V. V. Zhvalev, and I. M. Zrazhevskiy, 1974: Tasks and program of the CAENEX-72 experiment. *Trudy, Glavnia Geofizicheskaya Observatoriya*, **332**, 2-9.

Bolz, H. M., 1949: Die Abhängigkeit der infraroten Gegenstrahlung von der Bewölkung. *Zeitschritt für Meteorologie*, **3**, 201-203.

Bretz, S., H. Akbari, and A. Rosenfeld, 1998: Practical issues for using solar-reflective materials to mitigate urban heat islands. *Atmos. Environ.*, **32**, 95-101.

Ching, J. K. S., J. F. Clarke, and J. M. Godowitch, 1983: Modulation of heat flux by different scales of advection in an urban environment. *Bound.-Layer Meteor.*, **25**, 171-191.

Clarke, J. F., J. K. S. Ching, and J. M. Godowitch, 1982: An experimental study of turbulence in an urban environment. Tech. Rep. U.S. E.P.A. NMS PB 226085, Research Triangle Park, NC, 150pp.

Cleugh, H. A., 1995: Urban climates. In *Future Climates of the World: a Modelling Perspective*. A. Henderson-Sellers (ed.), *World Survey of Climatology*, **16**, 477-514.

———, and T. R. Oke, 1986: Suburban-rural energy balance comparisons in summer for Vancouver, B.C. *Bound.-Layer Meteor.*, **36**, 351-369.

Cooper, H. J., M. Garstang, and J. Simpson, 1982: The diurnal interaction between convection and peninsular-scale forcing over south Florida. *Mon. Weather Rev.*, **110**, 486-503.

Coppin, P. A., 1979: Turbulent fluxes over a uniform urban surface. Ph.D thesis, Flinders University, Adelaide, Australia, 196pp.

Daniel, C. E. J., and K. Krishnamurthy, 1973: Urban temperature fields at Poona and Bombay, India. *J. Met. Geoph.*, **24**, 4.

Davies, J. A., and S. B. Idso, 1979: Estimating the surface radiation balance and its components. In *Modification of the Aerial Environment of Crops*. Barfield, B. J., and J. F. Gerber (eds.), American Society of Agricultural Engineers, Michigan, pp. 183-210.

De Bruin, H. A. R., 1989: Physical aspects of the planetary boundary layer. In *Estimation of Areal Evapotranspiration* (Proceedings of a workshop held at Vancouver, B.C., Canada, August 1987). T. A. Black, D. L. Spittlehouse, M. D. Novak and D. T. Price (eds.), IAHS Publ. no. 177, 117-132.

———, and A. A. M. Holtslag, 1982: A simple parameterization of the surface fluxes of sensible and latent heat during daytime compared with the Penman-Monteith concept. *J. Appl. Meteor.*, **21**, 1610-1621.

Dyer, A. J., 1974: A review of flux-profile relationships. *Bound.-Layer Meteor.*, **7**, 363-372.

Estournel, C., and R. Vehil, D. Guedalia, J. Fontan, and A. Druilhet, 1983: Observations and modeling of downward radiative fluxes (solar and infrared) in urban/rural areas. *J. Appl. Meteor.*, **22**, 134-142.

Grimmond, C. S. B., 1988: An evapotranspiration-interception model for urban areas. Ph.D. Thesis, The University of British Columbia, Vancouver, B.C., 206pp.

———, 1992: The suburban energy balance: Methodological considerations and results for a mid-latitude west coast city under winter and spring conditions. *Int. J. Climatol.*, **12**, 481-497.

———, H. A. Cleugh, and T. R. Oke, 1991: An objective hysteresis model for urban storage heat flux and its comparison with other schemes. *Atmos. Environ.*, **25B**, 311-326.

———, and T. R. Oke, 1990: Preliminary comparisons of measured summer suburban and rural energy balances for a hot dry city, Tucson, Arizona. Proceedings of the International

Symposium on Urban Climatology, Air Pollution and Planning in Tropical Cities. Guadalajara, Mexico 25-30, November 1990.

———, and ———, 1995: Comparison of heat fluxes from summertime observations in the suburbs of four North American cities. *J. Appl. Meteor.*, **34**, 873-889.

———, and ———, 1999a: Heat storage in urban areas: local-scale observations and evaluation of a simple model. *J. Appl. Meteor.*, **38**, 922-940.

———, and ———, 1999b: Aerodynamic properties of urban areas derived from analysis of surface form. *J. Appl. Meteor.*, **38**, 1262-1292.

———, ———, and H. A. Cleugh, 1993: The role of "rural" in comparisons of observed suburban-rural flux differences. Exchange processes at the land surface for a range of space and time scales, *IAHS Publ.*, **212**, 165-174.

———, C. Souch, R. H. Grant, and G. Heisler, 1994: Local scale energy and water exchanges in a Chicago neighbourhood. *Chicago's Urban Forest Ecosystem: Results of the Chicago Urban Forest Climate Project*, USDA Forest Service Northeastern Forest Experiment Station, Gen. Tech. Rep. NE-186, 41-61.

Hammond, A. L. (ed.), 1992: World Resources (1992-1993). *A Guide to the Global Environment*, Oxford: Oxford University Press.

Hanna, S. R., and J. C. Chang, 1990: Modification of the hybrid plume dispersion model (HPDM) for urban conditions and its evaluation using the Indianapolis data set. Vol. III. Analysis of urban boundary layer data. EPRI Rep. No. A089-1200.III, 113pp.

———, and ———, 1992: Boundary-layer parameterizations for applied dispersion modeling over urban areas. *Bound.-Layer Meteor.*, **58**, 229-259.

Hartmann, D. L., 1994: *Global Physical Climatology*. San Diego: Academic Press.

Holtslag, A. A. M., and A. P. Van Ulden, 1983: A simple scheme for daytime estimates of the surface fluxes from routine weather data. *J. Appl. Meteor.*, **22**, 517-529.

Humphreys, E., 1999: Seasonal patterns and controls of evaporation from a Canadian West Coast Douglas Fir forest. Vancouver, B.C., Faculty of Agricultural Sciences, University of British Columbia, M.Sc. thesis, 154 pp.

Jáuregui, E., 1986: Tropical urban climates: review and assessment. In *Urban Climatol. and its Applic. with Special Regard to Trop. Areas*, Oke, T. R. (ed.), WMO No. 652, World Meteorol. Organiz., Geneva, 63-86.

———, 1996: *Bibliography of Urban Climatology for the Period 1992-1995. WCASP-36, WMO/TD-No. 759*, World Meteorol. Organiz., Geneva, 61 pp.

Kalanda, B. D., T. R. Oke, and D. L. Spittlehouse, 1980: Suburban energy balance estimates for Vancouver, B.C., using Bowen ratio-energy balance approach. *J. Appl. Meteor.*, **19**, 791-802.

Kalkstein, L. S., and K. E. Smoyer, 1993: The impact of climatic change on human health: some international implications. *Experientia*, **49**, 969-979.

Kanda, M., R. Moriwaki, M. Roth, and T. R. Oke, 1999: A novel dual-scintillation method to estimate area-averaged turbulent fluxes over a dense urban surface. Proc. ICB-ICUC Conference, Sydney, in press.

———, Y. Takayanagi, H. Yokoyama, and R. Moriwaki, 1997: Field observation of the heat balance of an urban area. *J. Japan Soc. Hydrol. & Water Resour.*, **10**, 329-336.

Karl, T. R., H. F. Diaz, and G. Kukla, 1988: Urbanization: its detection and effect in the United States climate record. *J. Climate*, **1**, 1099-1123.

Kerschgens, M. J., and R. L. Drauschke, 1986: On the energy budget of a wintry mid-latitude city atmosphere. *Contrib. Atmos. Phys.*, **59**, 115-125.

———, and J. M. Hacker, 1985: On the energy budget of the convective boundary layer over an urban and rural environment. *Contrib. Atmos. Phys.*, **58**, 171-185.

Kondratyev, K. Ya., V. P. Lominadze, O. B. Vasil'ev, V. S. Grishechkin, L. S. Ivlev, Sh. G. Gavasheli, V. F. Zhvalev, and V. Ya. Sikharulidze, 1976: A coordinated study of the radiation and meteorological regimes of Rustavi (CAENEX-72). *Soviet Meteorologiya i Gidrologiya*, **3**, 1-9.

McCaughey, J. H., 1985: A radiation and energy balance study of mature forest and clear-cut sites. *Bound.-Layer Meteor.*, **32**, 1-24.

McNaughton, K. G., and Jarvis, P. G., 1983: Predicting effects of vegetation changes on transpiration and evaporation. In *Water Deficits and Plant Growth*, Vol. 7. T. T. Kozlowski (ed.), Academic Press, New York, 1-47.

———, and T. W. Spriggs, 1989: An evaluation of the Priestley and Taylor equation and the complementary relationship using results from a mixed-layer model of the convective boundary layer. In *Estimation of Areal Evapotranspiration* (Proceedings of a workshop held at Vancouver, B.C., Canada, August 1987). T. A. Black, D. L. Spittlehouse, M. D. Novak and D. T. Price (eds.), IAHS Publ. no. 177, 89-104.

Monteith, J. L., and M. H. Unsworth, 1990: *Principles of Environmental Physics*. London: E. Arnold.

Newton, T., 1995: A parameterization of urban surface energy fluxes. Unpublished essay for Geography 505, UBC, Vancouver.

Okabe, I., 1995: The North American monsoon. Ph.D. Thesis, The University of British Columbia, Vancouver, B.C., 146pp.

Oke, T. R., 1978: Surface heat fluxes and the urban boundary layer. *WMO Symp. Boundary Layer Physics Applied to Specific Problems of Air Pollution*, Norköping, Sweden, World Meteor. Org. 63-69.

———, 1982: The energetic basis of the urban heat island. *Q. J. R. Meteorol. Soc.*, **108**, 1-24.

———, 1987: *Boundary Layer Climates*, second edition. London: Routledge.

———, 1988: The urban energy balance. *Prog. Phys. Geog.*, **12**, 471-508.

———, 1991: Bibliography of urban climate 1981-88. WCAP-15 WMO/TD No. 397.

———, 1995: The heat island of the urban boundary layer: characteristics, causes and effects. In *Wind Climate in Cities*. Cermak, J. E., A. G. Davenport, E. J. Plate and D. X. Viegas (eds.), Kluwer Academic Publishers, Netherlands, 81-107.

———, 1997: Urban environments. In *The Surface Climates of Canada*. Bailey, W. G., T. R. Oke, and W. R. Rouse (eds.), McGill–Queen's University Press, Montréal, 303-327.

———, H. A. Cleugh, S. Grimmond, H-P. Schmid, and M. Roth, 1989: Evaluation of spatially-averaged fluxes of heat, mass, and momentum in the urban boundary layer. *Weather and Climate*, **9**, 14-21.

———, and R. F. Fuggle, 1972: Comparison of urban/rural counter and net radiation at night. *Bound.-Layer Meteor.*, **2**, 290-308.

———, B. D. Kalanda, and D. G. Steyn, 1981: Parameterization of heat storage in urban areas. *Urban Ecology*, **5**, 45-54.

———, and J. H. McCaughey, 1983: Suburban-rural energy balance comparisons for Vancouver, B.C.: an extreme case? *Bound.-Layer Meteor.*, **26**, 337-354.

———, R. Spronken-Smith, E. Jáuregui, and C. S. B. Grimmond, 1999a: The energy balance of central Mexico City during the dry season. *Atmos. Environ.*, **33**, 3919-3930.

———, C. S. B. Grimmond, and R. Spronken-Smith, 1999b: Urban impacts on climate using station pairs: results from three cities and the meteorological implications. *Climatic Change*, submitted.

———, R. Taesler, and L. E. Olsson, 1990/91: The Tropical Urban Climate Experiment (TRUCE). *Energy and Buildings*, **15-16**, 67-73.

———, D. H. Yap, and R. F. Fuggle, 1972: Determination of urban sensible heat fluxes. In *International Geography 1972*. Adams, W. P., and F. M. Helleiner (eds.), University of Toronto Press, 176-178.

———, G. Zeuner, and E. Jáuregui, 1992: The surface energy balance in Mexico City. *Atmos. Environ.*, **26B**, 433-444.

Padmanabhamurthy, B., 1979: Isotherms and isohumes in Pune on clear winter nights: a meso-meteorological study. *Mausam.*, **30**, 134-138.

———, 1990: Urban climate research in India. Proceedings of the International Symposium on Urban Climatology, Air Pollution and Planning in Tropical Cities. Guadalajara, Mexico, 25-30 November 1990, 75-79.

———, and H. D. Bahl, 1981: Ecoclimatic modification of Delhi due to urbanization. *Mausam.*, **32**, 295-300.

PAHO, *Patterns of Urban Mortality, Sci. Publ. No. 151*, Pan American Health Organization, Washington, DC, 1967.

Paltridge, G. W., 1970: Day-time long-wave radiation from the sky. *Q. J. R. Meteorol. Soc.*, **96**, 645-653.

Pielke, R. A., 1984: *Mesoscale Meteorological Modeling*. Orlando: Harcourt Brace Jovanovich.

Pradhan, S. K., Dayakishan, and N. S. Manral, 1976: The effects of urbanization and industrial development on air temperatures at Bombay Airport. *Indian J. Met. Hydrol. Geoph.*, **27**, 187-190.

Prata, A. J., 1996: A new long-wave formula for estimating downward clear-sky radiation at the surface. *Q. J. R. Meteorol. Soc.*, **122**, 1127-1151.

Priestley, C. H. B., and Taylor, R. J., 1972: On the assessment of surface heat flux and evaporation using large-scale parameters. Mon. Weather Rev., **100**, 81-92.

Purdom, J. F. W., and K. Marcus, 1982: Thunderstorm trigger mechanisms over the southeast United States. *Prepr. Vol. 12th AMS Conf. on Severe Local Storms, San Antonio, Texas*, pp. 487-488, Jan. 11-15, 1982.

Raupach, M. R., R. A. Antonia, and S. Rajagopalan, 1991: Rough-wall turbulent boundary layers. *Appl. Mech. Rev.*, **44**, 1-25.

Roth, M., 1991: Turbulent transfer characteristics over a suburban surface. Vancouver, B.C., Department of Geography, University of British Columbia, Ph.D. dissertation, 292 pp.

———, and T. R. Oke, 1994: Comparison of modelled and "measured" heat storage in suburban terrain. *Contrib. Atmos. Phys.*, **67**, 149-156.

———, and ———, 1995: Relative efficiencies of turbulent transfer of heat, mass, and momentum over a patchy urban surface. *J. Atmos. Sci.*, **52**, 1863-1874.

Sass, B. H., 1992: A numerical model for prediction of road temperatures and ice. *J. Appl. Meteor.*, **31**, 1499-1506.

Saunders, I. R., and W. G. Bailey, 1997: Longwave radiation modeling in mountainous environments. *Phys. Geog.*, **18**, 37-52.

Schmid, H-P., 1994: Source areas for scalars and scalar fluxes. *Bound.-Layer Meteor.*, **67**, 293-318.

———, H. A. Cleugh, C. S. B. Grimmond, and T. R. Oke, 1991: Spatial variability of energy fluxes in suburban terrain. *Bound.-Layer Meteor.*, **54**, 249-276.

Sham Sani, 1977: An index of comfort for Kuala Lumpur – Petaling Jaya and its environs. *Sains Malaysiana.*, **6**.

———, 1980: *The Climate of Kuala Lumpur – Petaling Jaya Area Malaysia – A study of Urbanization on Local Climate within the Humid Tropics.* Monograph 1, Dept. of Geography, University of Kebangsaan, Malaysia.

Steyn, D. G., and T. R. Oke, 1980: Effects of a small scrub fire on the surface radiation budget. *Weather.*, **35**, 212-215.

———, H-P. Schmid, J. L. Walmsley, and J. D. Wilson, 1997: Spatial variability in surface climates. In *The Surface Climates of Canada.* Bailey, W. G., T. R. Oke, and W. R. Rouse (eds.), McGill–Queen's University Press, Montréal, 44-67.

Stull, R. B., 1995: *Meteorology Today for Scientists and Engineers.* New York: West Publishing Company.

Swinbank, W. C., 1963: Long-wave radiation from clear skies. *Q. J. R. Meteorol. Soc.*, **89**, 339-348.

Taesler, R., 1980: Studies of the development and thermal structure of the urban boundary layer in Uppsala. Meteor. Instit., Uppsala University, Uppsala, Sweden, Rep. No. 61, 177pp.

Tanner, B. D., and J. P. Greene, 1989: Measurements of sensible heat and water vapor fluxes using eddy correlation methods. Final report to U.S. Army Dugway Proving Grounds, DAAD 09-87-D-0088, 94 pp.

Thompson, M. A., D. I. Campbell, and R. Spronken-Smith, 1999: Evaporation from natural and modified raised peat bogs in New Zealand. Ag. and Forest Met., **95**, 85-98.

Verhoef, A., H. A. R. De Bruin, and B. J. J. M. Van Den Hurk, 1997: Some practical notes on the parameter kB^{-1} for sparse vegetation. *J. Appl. Meteor.*, **36**, 560-572.

Voogt, J. A., and C. S. B. Grimmond, 1998: Proceedings of the 2nd Urban Environment Symposium/13th Conference on Biometeorology and Aerobiology. Albuquerque, New Mexico, 2-6 November 1998, 98-99.

———, and T. R. Oke, 1997: Complete urban surface temperatures. *J. Appl. Meteor.*, **36**, 1117-1132.

Webb, E. K., G. I. Pearman, and R. Leuning, 1980: Correction of flux measurements for density effects due to heat and water vapour transfer. *Q. J. R. Meteorol. Soc.*, **106**, 85-100.

Weihe, W. H., 1986: Life expectancy in tropical climates and urbanization. In *Urban Climatol. and its Applic. with Special Regard to Trop. Areas*, Oke, T. R. (ed.), WMO No. 652, World Meteorol. Organiz., Geneva, 313-353.

White, J. M., F. D. Eaton, and A. H. Auer, Jr., 1978: The net radiation budget of the St. Louis metropolitan area. *J. Appl. Meteor.*, **17**, 593-599.

Willmott, C. J., 1982: Some comments on the evaluation of model performance. *Bull. Amer. Meteor. Soc.*, **63**, 1309-1313.

Yap, D. H., 1973: Sensible heat fluxes measured in and near Vancouver, B.C. Department of Geography, University of British Columbia, Ph.D. dissertation, 177 pp.

———, 1975: Seasonal excess urban energy and the nocturnal heat island – Toronto. *Archives for Meteorology, Geophysics and Bioclimatology*, **B 23**, 69-80.

———, and T. R. Oke, 1974: Sensible heat fluxes over an urban area – Vancouver, B.C. *J. Appl. Meteor.*, **13**, 880-890.

Zeuner, G., 1983: The urban climate in tropical cities: climatological characteristics, applications and suggestions for future research. Unpublished essay for Geography 411, UBC, Vancouver.

APPENDIX 1 NET RADIOMETER INTERCOMPARISON

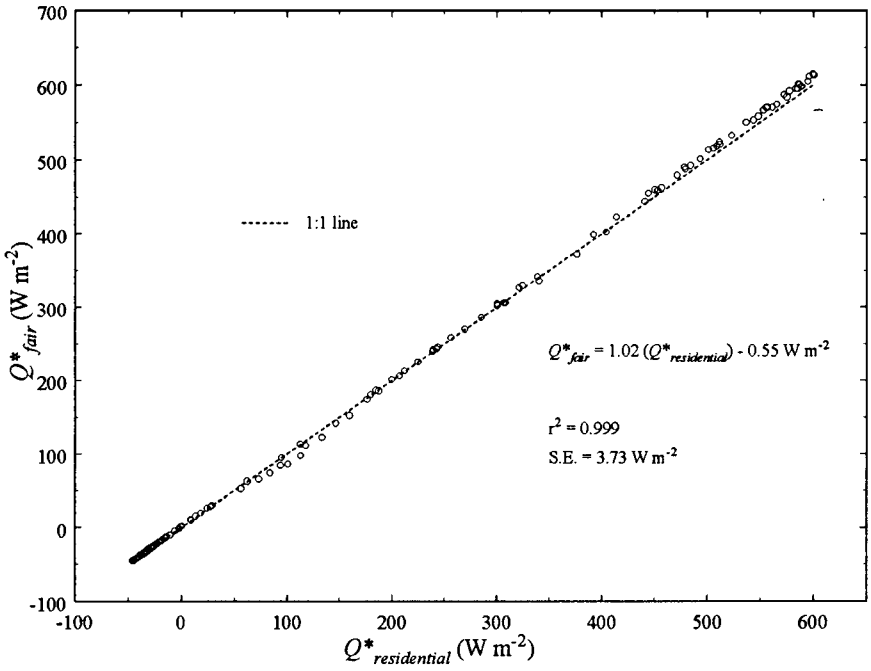

Fig. A.1 Intercomparison between the two REBS net radiometers, conducted at a height of 2 m over a grassy field in Bloomington, Indiana, from July 10-12, 1995. No regression line is plotted because it would obscure the 1:1 line.

The slope of the linear regression is 1.016, and the y-intercept is close to zero, so from –100 to 600 W m^{-2}, the two instruments provide the same reading to within less than about 2%. No correction has been applied to either instrument because neither is an absolute standard. It can only be said that that the Q^*_{fair} radiometer tends to read about 1.6% higher than $Q^*_{residential}$. At small input values (± 100 W m^{-2}), the two are essentially indistinguishable, differing by 1 to 2 W m^{-2}. At +600 W m^{-2} on the $Q^*_{residential}$ instrument, the Q^*_{fair} sensor might be expected to read approximately 609 W m^{-2}.

APPENDIX 2 α_{PM} vs. α_{PT}

Essentially $\alpha_{PM} \sim \alpha_{PT}$, but because they are calculated in slightly different ways, they are not exactly interchangeable. α_{PM} is calculated by plotting a number of points, fitting a straight line through them by linear regression, and extracting α_{PM} from the slope (m) of the line using:

$$\alpha_{PM} = -[m(1 + \gamma/s) - \gamma/s - 1] \tag{A2.1}$$

for a plot of Q_H vs. A (= $Q^* - \Delta Q_S$), and

$$\alpha_{PM} = m(1 + \gamma/s), \tag{A2.2}$$

for a plot of Q_E vs. A, where in both cases γ and s are calculated from the average near-surface air temperature during the flux observation period. Equations (A2.1) and (A2.2) are taken from (4.16) and (4.17), respectively, thus the fact that the line fitted through the points may not pass through the origin is accounted for by β_{PM}.

If (4.17) is rearranged to calculate α_{PM} for a single set of flux measurements (e.g. a single hourly average of each of Q^*, Q_H, and Q_E), it has almost the same form as (4.1) when the latter is used with Q_E observations to calculate α_{PT}:

$$\alpha_{PT} = Q_E / [(s/(s + \gamma))(Q^* - \Delta Q_S)], \tag{A2.3}$$

which is used in chapter 4 to calculate the α_{PT} values shown. However, this rearranged version is incorrect because (4.17) is designed to find α_{PM} by plotting a group of flux measurements, not single measurement points. Therefore putting it to a use for which it was not intended gives an equation which though similar to (A2.3), is dimensionally inconsistent:

$$\alpha_{PM} = Q_E / [(s/(s + \gamma))(Q^* - \Delta Q_S)] - \beta_{PM} \tag{A2.4}$$

Here α_{PM} is dimensionless, as is the first term on the right side of (A2.4), but β_{PM} has units of W m^{-2}.

Therefore in summary, α_{PT} is designed to enable calculation of the parameter for a single set of flux measurements, if necessary, but α_{PM} requires a series of observations. Also, α_{PT} incorporates the offset, i.e. the fact that a linear regression of Q_E vs. A may not pass through the origin, while α_{PM} does not. Thus if α_{PM} and α_{PT} are calculated for the same set of data, the values obtained are similar but not identical. In Miami, the daytime, all-sky dataset gives an α_{PM} of 0.501, while the average α_{PT} for these data is 0.514. Another difference between the two is that α_{PM} can be found from observations of A with either Q_H or Q_E, while α_{PT} only relates Q_E to A.